Master Thesis

“Direct-Ink-Writing 3D Printing of Microfluidic Guidance Devices for Nigrostriatal Connectoids”

Carried out for the purpose of obtaining the degree of Dipl.-Ing, submitted at TU Wien, Faculty of Electrical Engineering and Information Technology

Stefan Sützl

Matr.Nr.: 01327098

under the supervision of

Univ.Prof. Dipl.-Ing. Dr. Heinz Wanzenböck

Institut of Solid State Electronics

reviewed by

Name of Reviewer 1	Name of Reviewer 2
Institute	Institute
Institute Address	Institute Address

This work was supported by the European Union withing the framework of the OpenMIND project.

I confirm, that going to press of this thesis needs the confirmation of the examination committee.

The experimental work that this thesis is based upon was conducted by the author at the facilities of the Technical University of Denmark (DTU) under the supervision of Prof. Jenny Emnéus from the Department of Biotechnology and Biomedicine during an external stay with grants provided by the Erasmus project.

Affidavit

I declare in lieu and oath, that I wrote this thesis and performed the associated research myself, using only literature cited in this volume. If text passages from sources are used literally, they are marked as such.

I conform that this work is original and has not been submitted elsewhere for any examination, nor is it currently under consideration for a thesis elsewhere.

Vienna, September, 2023

Signature

Table of Contents

Abstract

Neurodegenerative diseases such as Parkinson's disease is a major burden to society which is expected to increase over the coming decades. The openMIND project intends to contribute to the relieve of this burden through the creation of multi-regional brain organoid models called connectoids. As a first step in this direction the fabrication of PDMS guidance devices for nigrostriatal pathfinding was investigated. To this aim a new workflow for rapid prototyping of these guidance devices using volumetric direct-ink-writing (DIW) 3D printing was established. This approach was based on RepRap derived printing technology and may therefore present a viable alternative for research groups that cannot afford state-of-the-art 3D printing systems. Besides the printing of the guidance devices supportive experiments were conducted to evaluate the reproducibility of the printing method and to lay the foundation for its improvement. The guidance devices were tested on hVM1 spheroids and handed over to Lund university where they were tested with brain organoids. In addition, different condition for the formation of hVM1 spheroids were tested to investigate their suitability for nigrostriatal models.

Abbreviations

Table 1 List of abbreviations.

abbreviation	meaning
CAD	computer-aided design
CNC	computer numerical control
cAMP	cyclic adenosine monophosphate
DIW	Direct-Ink-Writing
ECM	extracellular matrix
GDNF	glial cell line-derive neurotrophic factor
GPi	globus pallidus pars interna
GPe	globus pallidus pars externa
hVM1	human ventral midbrain 1
hrEGF	human recombinant epidermal growth factor
hrFGF	human recombinant fibroblast growth factor
IsO	Isthmic organizer
magn.	magnification
LOW	Leaky optical waveguide
O/N	overnight
PBS	phosphate-buffered saline
PD	Parkinson's disease
PDMS	polydimethylsiloxane
PLL	poly-L-lysine
pos.	position
qPCR	quantitative polymerase chain reaction
rpm	rounds per minute
SNc	substantia nigra pars compacta
SNr	substantia nigra pars reticulata
STN	subthalamic nucleus
TH	tyrosine hydroxylase
β-III tub.	β-III tubulin
τ	transfer day

1. Introduction

1.1 Parkinson's Disease & the Nigrostriatal Pathway

Parkinson's disease (PD) is the second-most common neurodegenerative disease and thus constitutes a major strain on society. This disease leads to an impairment of motor functions with symptoms such tremor, rigidity, and bradykinesia. PD related bradykinesia manifests mostly through the delayed onset of movement as well as a reduction in movement amplitude and velocity. The appearance of these symptoms is known to be related to an advanced depletion of dopamine in the striatum (~80%)[1] which is a nucleus the forebrain. This depletion is caused by the loss of dopaminergic neurons in the substantia nigra pars compacta (SNc) that innervates the dorsal striatum (caudate nucleus & putamen) via the nigrostriatal pathway (Figure 1/A). The dopaminergic denervation of the striatum then leads via the basal ganglia-thalamocortical circuit to reduced activation of the motor cortex (Figure 1/B) which is assumed to play a key role in the onset of parkinsonian motor symptoms[2]. Administration of the dopaminergic drug L-dopa or deep brain simulation can both alleviate the motoric symptoms, but they ultimately cause side effects such as L-dopa-induced dyskinesia[3] or depression and fatigue[4]. The etiology of PD is not yet determined but several environmental and genetic risk factors have been discovered[5]. It is assumed that the development of PD may start up to decades before the onset of motor symptoms and is known to be associated with the formation of neural inclusions called Lewy bodies. These Lewy bodies are abnormal aggregations of the protein α-synuclein. Although their accumulation increases with the progression of PD their role is not yet understood[6]. Neurodegenerative diseases are associated with a distinctly high failure rate in drug development which can be as high as 99%[7]. A major contributor to the failure of drug candidates is the poor translation from animal models to humans caused by the particularities of the human brain. The recent development of human brain organoids offers the possibility to study disease relevant mechanisms on a human *ex-vivo*-type platform. Besides, it permits to study the effects of disease related genes that show different effects in human-derived organoid cultures than in animal models.

1.2 Brain Organoids and Neural Spheroids

What generally distinguishes the concept of organoids from classical spheroid cultures are the additional criteria organoids must meet. While it is sufficient to constitute a self-assembled 3-dimensional system of adhering cells to pass certain definitions of spheroids[8], it requires additional layers of organization and functionality to constitute an organoid. In contrast to this, some definitions of spheroids include the absence of foreign extracellular matrix[9, 10], which would exclude most organoid systems due to the usage of Matrigel in their formation. In regards to neural cells there is the term neurosphere[11-13] which refers to a specific systems of free-floating clusters of neural stem cells and should not be used for neural spheroids [10, 14] in the generic case to avoid confusion. While spatial organization and organizational hierarchy are mostly neglected in spheroid cultures, they are a crucial part in the formation of organoids, which resembles the embryonic development *in vivo*[15-20]. This spatial organization of cells is facilitated by different mechanisms of self-sorting (self-assembly) and spatially restricted lineage commitment (self-patterning), which are a requisite for the development of organ-specific functionalities (self-driven morphogenesis)[15, 16]. The self-sorting aspect refers to selective aggregation or rearrangements in respect to the relative position of cells[16] and is largely governed by the minimalization of potential energy[21]. A comparable process to this in terms of involved mechanisms would be the spontaneous

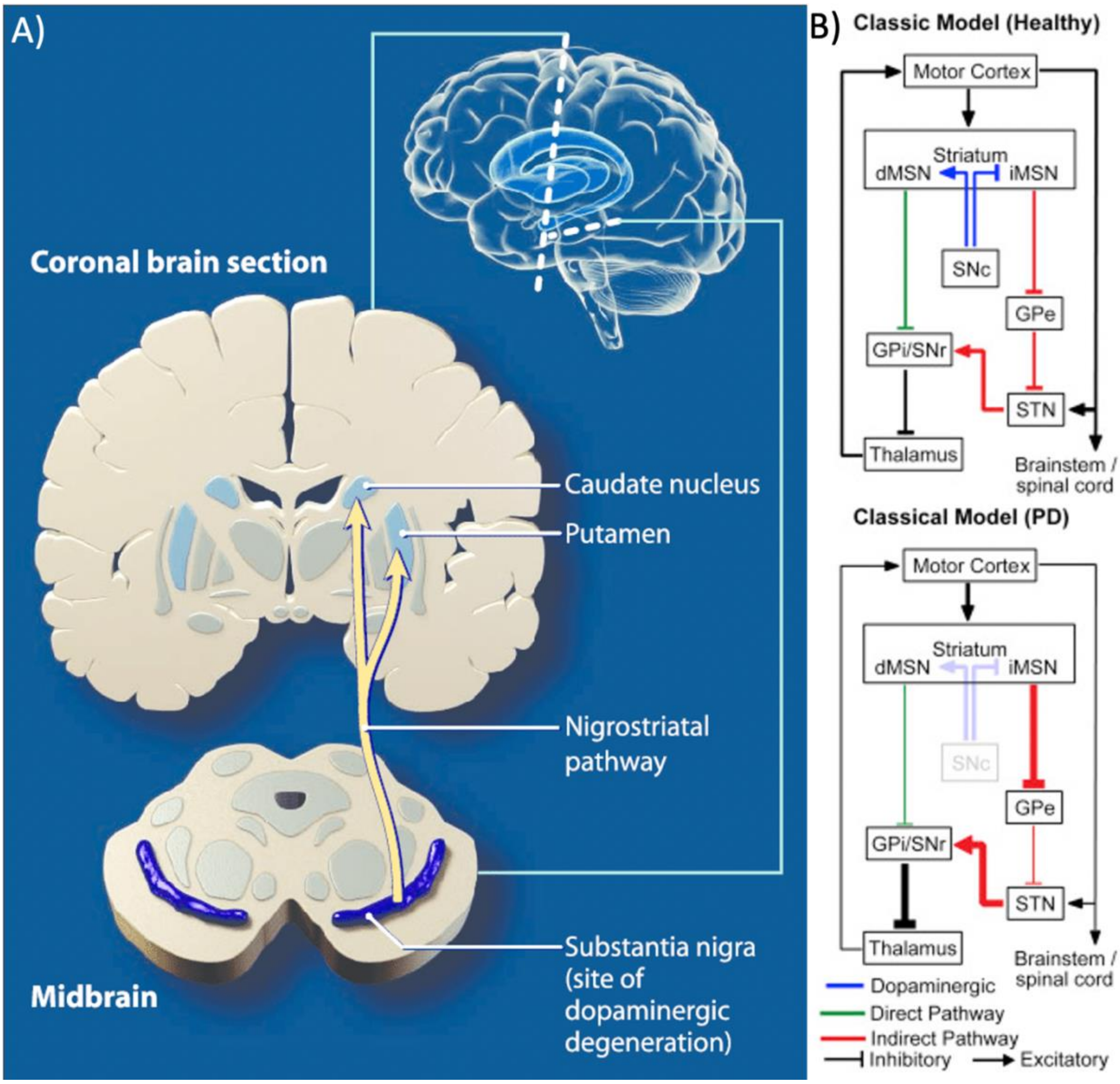

Figure 1 The nigrostriatal pathway (A) and the basal ganglia (B). A) Coronal brain section showing the putamen and the caudate nucleus which form the dorsal striatum of the forebrain and their dopaminergic innervation from the substantia nigra that is referred to as the nigrostriatal pathway[22]. B) The classical model of the basal ganglia-thalamocortical circuit that illustrates the effects of parkinsonian dopaminergic denervation of the substantia nigra pars compacta (SNc)[2]. Nigrostriatal dopamine (blue) effects the striatal GABAergic (inhibitory) output neurons, referred to as the medium spiny neurons (MSN), that project modulate the basal ganglia output nuclei globus pallidus pars interna (GPi) and the substantia nigra pars reticulata (SNr) via a direct (green) or an indirect (red) pathway. The indirect pathway involves GABAergic neurons in the globus pallidus pars externa (Gpe) and downstream glutamatergic (excitatory) neural projections from the subthalamic nucleus (STN) to Gpi & SNr. In the healthy state nigrostriatal dopamine activates the direct pathway which inhibits inhibitory basal ganglia output on the thalamus and inhibits the indirect pathway that excites inhibitory basal ganglia output on the thalamus. In the parkinsonian condition dopaminergic depletion of the striatum causes an imbalance that favors the inhibitory pathway thus leading to a decreased excitation of the motor cortex by the thalamus. The image on the left was taken from [22] and the image on the right is a modification of a figure from [2].

Formation of snowflakes, which does not require any mechanistic aspects specific to biological systems. The self-patterning aspect involves spontaneous symmetry breaking from homogenous cell populations and can be governed by different mechanisms. One such mechanism are Turing-type reaction-diffusion systems[23] where patterns are formed spontaneously in initially homogenous systems by the interplay of auto-activated short-range activation and long-range inhibition of chemical processes. Other known mechanisms of symmetry breaking in tissues are based on mutual exclusivity between different cellular

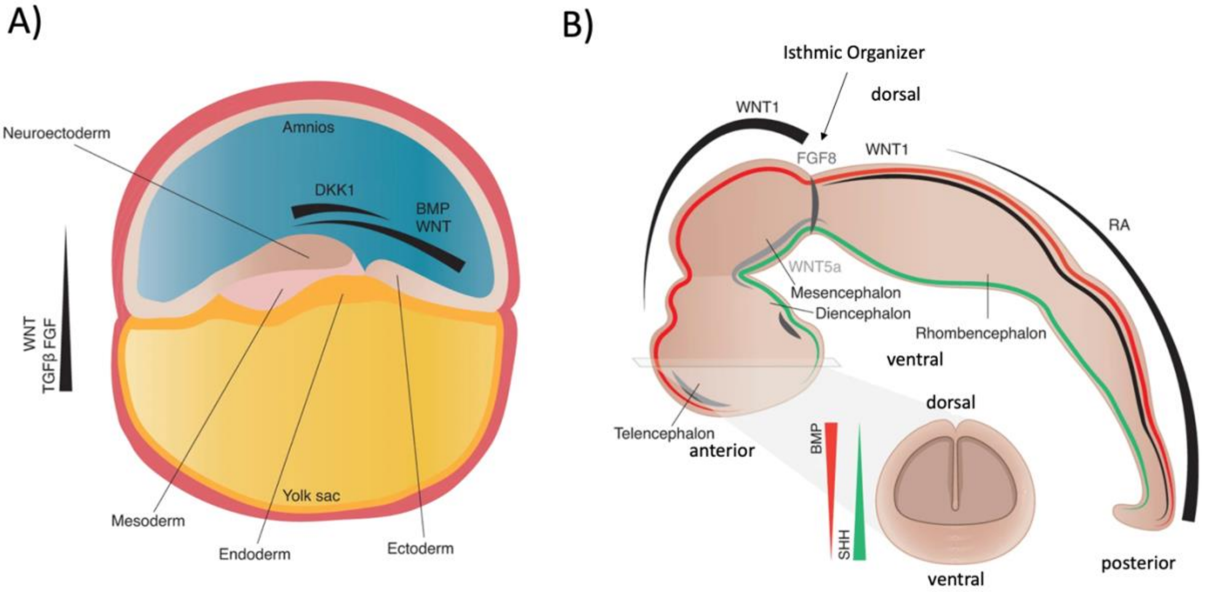

Figure 2 Human embryonic germ layers at the stage of the gastrula (A) and the human neural tube at embryonic day 49 (B). While the mesoderm gives rise to the muscular tissue, connective tissue, and the red blood cells among others the endoderm gives rise to the interior lining (epithelium) of the digestive and respiratory tube. The ectoderm gives rise to both neural tissue and several epithelial linings as well as the epidermis. Cells get directed towards a mesodermal or endodermal fate (mesendodermal) through the gradient of signaling proteins from Wnt & the TGF-β superfamily. The gradient of Wnt & BMP further directs ectoderm towards a non-neural fate (non-neural ectoderm), such that an opposing gradient of the Wnt inhibitor Dickkopf-1 (DKK1) develops to secure the neuroectoderm. The anterior-posterior axis of the neural tube (B) goes from the forebrain (Telencephalon & Diencephalon) over the midbrain (Mesencephalon) to the hindbrain (rhombencephalon). The isthmic organizer emerges during late gastrulation & early somitogenesis and directs differentiation into forebrain, midbrain, and hindbrain through the expression of FGF8 at its posterior side and a decreasing gradient of Wnt1 in anterior direction. Hindbrain development is further organized be an increasing gradient of retinoic acid (RA) in posterior direction. Cellular differentiation along the dorsoventral axis is organized by to gradients in opposite directions of BMP and SHH. Both sides of the figure are slightly modified versions of figures found in [24].

processes within a regulatory network[16]. In some instances, symmetry breaking within homogenous cell populations leads to the emergence of cellular structures that begin to asymmetrically direct lineage commitment of their surrounding cells through the generation of morphogen gradients along the now emerging developmental axes. One such structure that emerges between late gastrulation and early somitogenesis in the neural tube is the isthmic organizer, which forms the border between midbrain (mesencephalon) and the anterior part of the embryonal hindbrain (metencephalon).The isthmic organizer is a ring of Wnt1 expressing cells on the mesencephalic side and Fgf8 expressing cells on the metencephalic side[25]. The interplay of Wnt1 and Fgf8 induces midbrain-hindbrain identity and the Wnt1 gradient in anterior direction controls cell lineage commitment towards midbrain or forebrain identity[24, 25] (Figure 2). An example of self-driven formation of organ-specific functionalities (organogenesis) is the cellular formation of axons and their projection towards their cellular targets. These axons regionally form nerve tracts by bundling around a pioneer axon to form so-called axonal fascicles. Related to the spontaneous organization of cells is the concept of stigmergy, that describes the self-organization or emergence of complex systems by non-linear interactions between unsupervised local actors[26, 27]. This concept was initially formulated to explain how insects can maintain levels of organization that by far exceed their intellectual capabilities, which works without an apparent coordinator or even communication between the actors. Similar to how subtle differences in environmental cues can determine whether an ant colony sets in motion or not, stem cell cultures can change their entire developmental trajectory based on small differences in

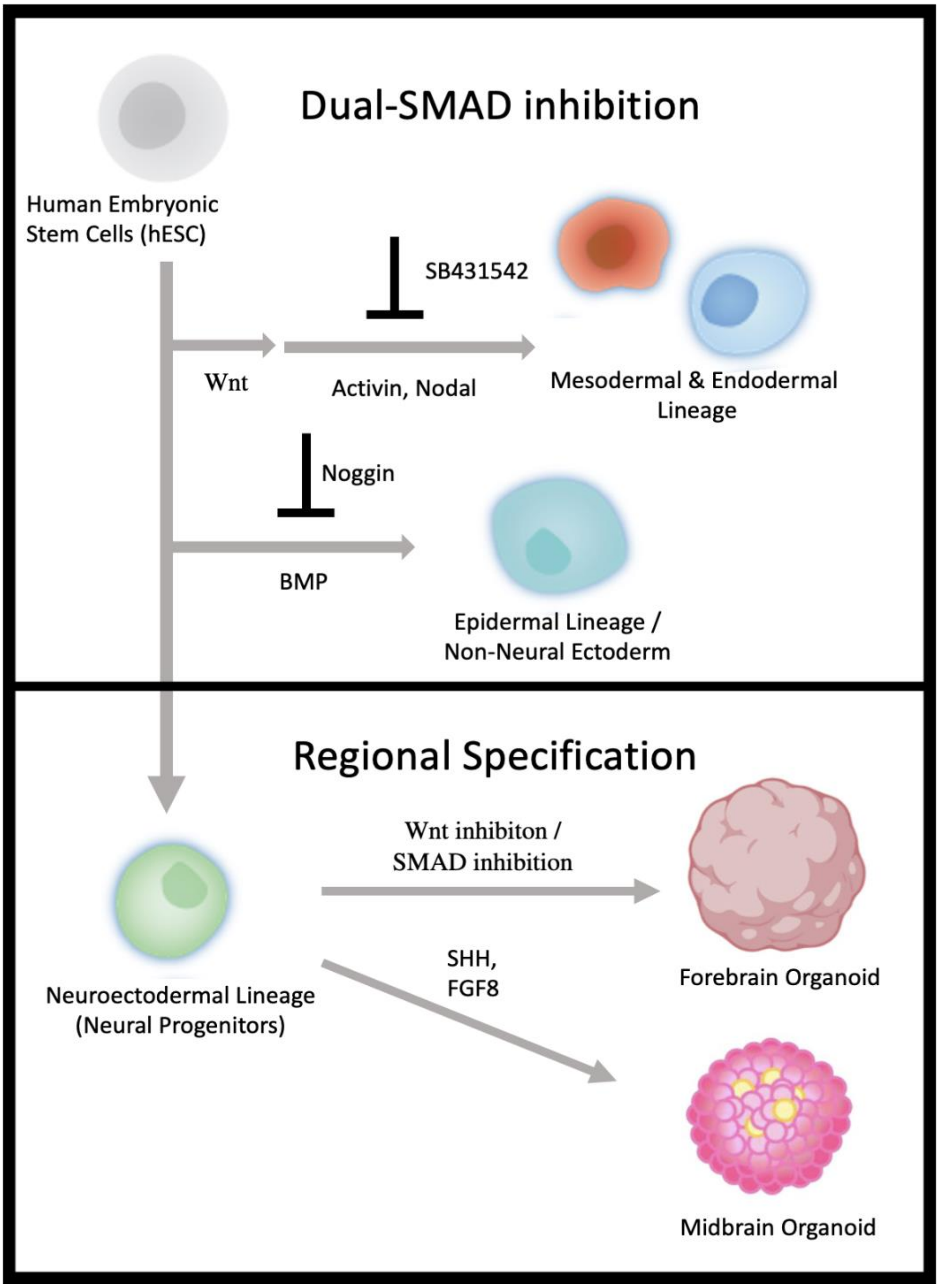

Figure 3 Dual-SMAD inhibition and acquirement of region specificity in brain organoid formation. The first step in brain organoid formation is usually dual-SMAD inhibition to prevent early germ layer formation and commitment to mesodermal, endodermal or non-neural ectodermal fate[24]. SMAD proteins convey signals from the transforming growth factor beta (TGF-β) superfamily at the cytoplasmic level[28-30]. The most common form of dual-SMAD inhibition is treatment with SB431542 to disrupts the Nodal/Activin pathways via phosphorylation of activin-like kinase (ALK) 4,5 & 7 receptors in combination with Noggin treatment to inhibit bone marrow protein (BMP). Since Wnt is a crucial activator of the Nodal gene[31] a similar effect can be achieved by Wnt inhibition with IWR1endo[24, 32]. Dual-SMAD inhibition of ESCs leads to the generation of neural progenitors and from there forebrain organoids can be formed without additional patterning steps, but further Wnt/SMAD inhibition improves homogeneity[33] in forebrain organoids in analogy to the Wnt regulated anterior-posterior specification of the neural tube in vivo[34]. Protocols for midbrain-like organoids typically use sonic hedgehog (SHH) & fibroblast growth factor 8 (FGF8) for regional specification. In vivo FGF8 is involved in the activity of the isthmus organizer that stabilizes the border between midbrain & hindbrain [35] while SHH expression is associated with the induction of ventral identity in the neural plate[24, 36]. For the figure individual elements were taken from [37] and [38].

chemical or mechanical cues. An interesting example of this are the germ-cell tumors called teratomas, which can form tissues with ectodermal, mesodermal and endodermal origin in a chaotic fashion in dependency on their initial conditions[15, 18]. In order to recapitulate embryonal development *in-vitro* human stem cells or induced pluripotent cells can be used to form so-called embryonic bodies which comprise the three primordial human germ layers ectoderm, mesoderm and endoderm[39]. The emergence of the three primordial human germ layers can be understood as an initial step of the commitment of pluripotent stem cells along different paths or cell lineages, that ends with their differentiation into functional tissue or other specialized cells. *In-vitro* this can be facilitated via the application of external patterning factors that guide the cells towards certain lineages in so-called directed differentiation[15, 17]. The first brain organoids were generated without the use of external patterning growth factors relying only on growth conditions that support cell intrinsic signaling[40]. This approach was based on the fact that embryonic stem cells can commit themselves towards a neuroectodermal fate through autocrine FGF signaling, which in the past had given rise to the hypothesis of a default pathway before this mechanism was better understood[41]. Other approaches generate brain organoids through a process called dual-SMAD inhibition[29] (Figure 3), that reduces organoid heterogeneity[42, 43]. The SMAD proteins convey the signaling of the TGF-β superfamily at the cytoplasmic level and their inhibition is usually done upstream via phosphorylation of their transmembrane receptors[30]. The TGF-β superfamily comprises besides the TGF-β subfamily the bone morphogenetic proteins, the activins and nodal which direct cells towards mesoendodermal or non-neural ectodermal fate[24]. A single round of dual-SMAD inhibition is sufficient for the generation of forebrain-like organoids[32], but a second round of SMAD inhibition or Wnt inhibition reduces non-forebrain identities[43]. During *in-vivo* embryonal development the anterior-posterior axis is formed by reciprocal gradients of Wnt, which upregulate *nodal* and secreted frizzled-related protein 1 (sFRP1) and thus inhibit Wnt signaling[34]. Further specification of forebrain organoids towards striatal identity had been achieved with agonist of retinoic acid receptors[44]. To generate human midbrain-like organoids dual-SMAD inhibition is used in combination with SHH and FGF8 activators[45]. *In vivo* FGF8 is involved in the activity of the isthmus organizer that stabilizes the border between midbrain & hindbrain[35] while SHH expression is associated with the induction of ventral identity in the neural plate[24, 36]. This coincides with the fact that most dopaminergic neurons are located in the ventral part of the midbrain[46]. For a multi-organoid system to mimic the interplay between midbrain and forebrain a functional synaptic connection of dopaminergic neurons projecting from the midbrain-like organoid into the forebrain-like organoid must be established. Synaptic connection between different brain organoids had been reported in so-called assembloid systems where striatum-like organoids and cortex-like organoids had been cultured in close contact in ultra-low attachment plates[44]. Since closed contact does not resemble the *in-vivo* reality of the nigrostriatal pathway where Parkinson-related neural degeneration is most prominent, the connectoid system has been proposed[47].

1.3 The Connectoid as a Model of the Nigrostriatal Pathway

These connectoids are proposed to be multi-regional brain organoids synaptically connected via axonal fascicles that span through microchannels (Figure 4). The openMIND projects aims to fabricate connectoid models of the nigrostriatal pathway with integrated leaky optical waveguides (LOW), 3D microelectrode arrays and GABA sensors. The microelectrode arrays are envisioned to be fabricated by pyrolization of 3D printed SU8 structures as it was established in the research group of Prof. Stephan Sylvest Keller and the envisioned fabrication methods for the LOWs are at the moment confidential. The LOWs allow for controlled

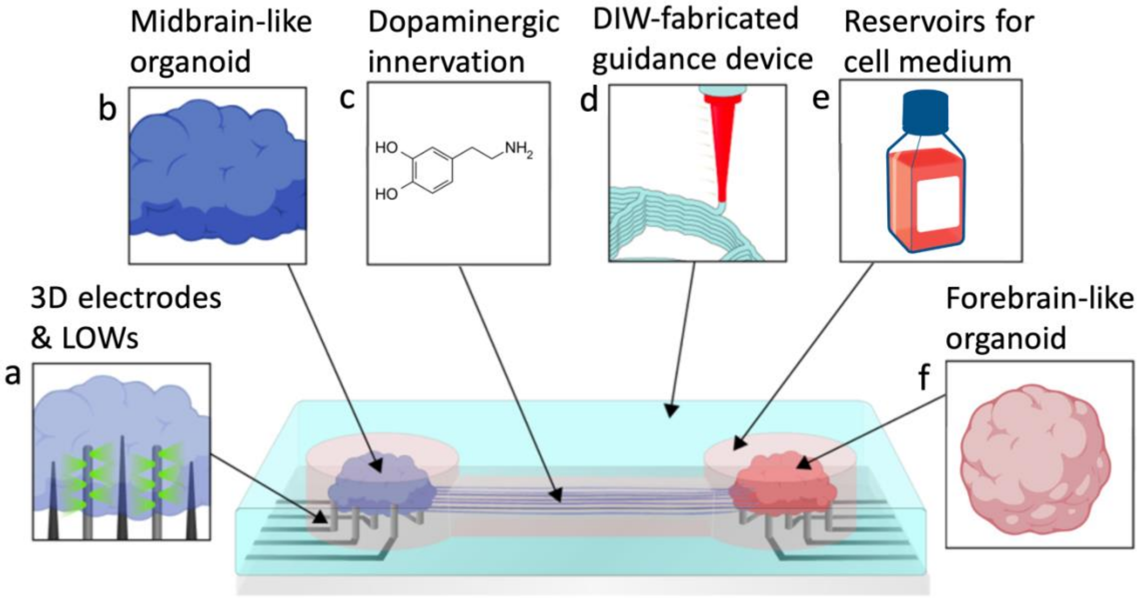

Figure 4 Concept of a simplified nigrostriatal connectoid device. The direct-ink-writing-fabricated (d) guidance device guides dopaminergic axonal fascicle formation (c) from the midbrain-like organoid (b) towards the forebrain-like organoid (f). The guidance device includes large 3D reservoirs (e) to satisfy the organoids need for ample medium consumption. Integration of leaky optical waveguides (LOWs, a) allows for the controlled excitation of optogenetically modified midbrain-like organoids[48] and thus controlled dopamine release into the forebrain-like organoid. Integration of dopamine-selective 3D electrodes (a) further allows for spatially resolved detection of dopamine release into the forebrain-like organoids and GABA sensors for the measurement of resulting GABAergic response from the forebrain-like organoid. The figure is a modified version of a figure from the proposal of the openMIND project.

excitation and thus neurotransmitter release from optogenetically modified organoids[48]. The development and integration of dopamine-selective electrodes would then allow for real-time spatially resolved monitoring of dopamine release into the forebrain and the integration for GABA sensors for monitoring of the resulting changes in GABA concentration. The first step for the development of the connectoid platform would be the fabrication of devices for axonal guidance that supports the formation of axonal fascicles through a channel that connects two organoid chambers. An interesting candidate for the fabrication of such devices is Direct-Ink-Writing (DIW) 3D printing.

1.4 Direct-Ink-Writing 3D printing

Direct-Ink-Writing is a 3D printing technique where a shear thinning ink is deposited layer-by-layer through a nozzle (Figure 5/A) in order to fabricate 3-dimensional structures[49]. In 3D printing a printhead is moved in x, y and z direction and deposits its material in a temporally and spatially controlled process. The difference between DIW 3D printing and the more famous FDM or FFF 3D printing lies in the deposited material. While FDM 3D printing deposits thermoplastic filament by controlled heating inside the nozzle of the printhead DIW deposits ink that gets it final material characteristics through a curing process. To make 3-dimensionally fabrication possible this puts certain demands on a used ink. Since the ink has to be extruded through the nozzle of the printhead the ink must be fluid under shear, but the ink has to behave like a solid after extrusion such that the print can retain its 3-dimensional form until curing. In terms of rheology the ink must behave like a viscoelastic fluid under shear and like a viscoelastic solid at rest. This means that the ink’s loss modulus must dominate in respect to the storage modulus while their relation must be inverse under stress. Loss modulus represents the energy that is dissipated as heat while the storage modulus represents the energy stored in the elastic deformation during deformation[50]. Their ratio is given by the viscoelastic stress-strain phase-shift δ (Figure 5/B). A common simplification of this is that inks for 3D printing have to be shear-thinning, but these rheological phenomena are not the same since shear-thinning describes a reduction of viscosity with increasing shear. There are two major types of extrusion control used for DIW which are volumetric or pneumatic. During volumetric DIW a plunger is pushed by a screwing mechanism to control ink extrusion in contrast to the pneumatic mechanism used in other methods. Volumetric control is mostly used for soft materials like hydrogels especially when it contains sensitive and valuable materials like cells. In pneumatic DIW a pressure is applied on the ink and this technique is mostly used for viscous materials since larger extrusion forces can be applied. In most instances, DIW is realized through commercial 3D printers or costume made XYZ machines with an integrated extrusion mechanism. These machines are usually programmed in the computer numerical control (CNC) programming language RS-274, better known as g-code. These g-codes can be generated by so-called slicer software from a computer-assisted design (CAD) file that represents a 3D structure. This workflow is suitable for rapid prototyping since both the slicing and the CAD file can be changed readily, which is important during an ongoing design process.

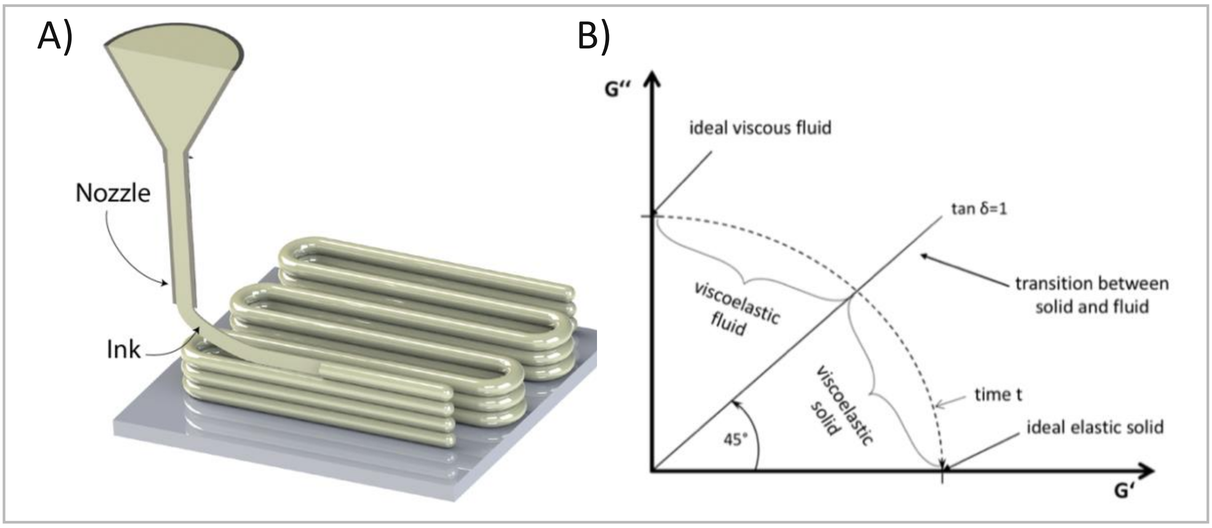

Figure 5 Basic principle of Direct-Ink-Writing (DIW) (A) and illustration of the complex modulus that describes the viscoelastic spectrum (B). In DIW a viscoelastic ink will be extruded through a nozzle in order to print 3-dimensional structures. The mechanic response of materials can be described on a spectrum between ideal elastic solid that regain their form after deformation and ideal viscous fluid where all the energy used for deformation gets dissipated as heat. Image A was taken from [51] and Image B from [52].

The material used in this project for fabrication is polydimethylsiloxane (PDMS), a silicone widely used for biomedical engineering since it holds a plethora of advantageous characteristics such as chemical inertness, biocompatibility, gas permeability, optical transparency and relative ease of fabrication[53]. Although pneumatic DIW of PDMS is an established process[54] a volumetric printer was chosen because commercial pneumatic 3D printers are very cost expensive which makes them unavailable for many research groups and the ones in use are usually used by many different researchers such that cheaper alternatives may present themselves as a valuable addition to the more expensive machines. The most common fabrication method with PDMS is soft lithography where the material gets casted into a master mold and thus adopts its inverted shape during hardening[55]. Biomedical research often requires a liquid-tight sealing between devices and their substrate, which demands exceedingly flat surfaces. Meeting this demand with stereolithography usually demands specialized fabrication methods and expensive cleanroom facilities which only a minority of universities can afford. Another advantage of DIW is that rapid prototyping is more feasible since the fabrication of the molds is the most time-consuming step. In addition, the additive nature of 3D printing represents a possible vector for the integration of microelectronic units into the fabricated device. Besides commercially available printers there is a plethora of open-source technology that is already used for the fabrication of self-made 3D printers and their associated investment costs would be affordable for most research groups. Much of this technology is derived from the RepRap project[56], which had the aim of creating self-replicating open-source 3D printers. Although there are open-source pneumatic 3D printers[57, 58], that better resemble established methods for PDMS printing volumetric open-source printers can be assumed to be more user-friendly since the high pressures necessary for PDMS extrusion may present a security risk for the researchers, especially since most of them will not have expertise in the maintenance of such systems. An illustration of the investment costs associated with the different fabrication methods for biomedical PDMS devices is shown in Figure 6. Other methods of 3D printing like vat photopolymerization offer a more precise and easier method for manufacturing than DIW, but it is currently still debated whether so-called biocompatible photo resins have a negative influence on cell cultures.

Figure 6 Investment costs associated with different devices for 3D fabrication of PDMS devices. The respective prices for the printers and pictures are taken from [59], [60], [61] and [62].

Since many DIW printers like the FelixBIO or some RegenHU models are called bioprinters it is adequate to discuss the term bioprinting here. In the narrower sense bioprinting refers to the printing of biological materials and their scaffolds while in the wider sense it can refer to the printing of biomedical devices using specifically engineered biocompatible materials called biomaterials. 3D printing of biological material is generally done by volumetric DIW since the higher pressures of pneumatic printing and the resins as well as the applied wavelengths of vat polymerization will typically result in cell death. Uncured PDMS is typically cytotoxic due to their functional groups for crosslinking, but applications would be limited anyway due to its hydrophobic nature. 3D printing of devices for cell culture requires either sterile fabrication or sterilization afterwards. Ethanol is a commonly used agent for sterilization but in the case of PDMS devices it must be considered that due to swelling the PDMS might absorb ethanol from where it might diffuse into the cell medium during culture.

2. Materials & Methods

2.1 Overview of Experimental Work

The idea behind this project was to use the FelixBIO, a comparatively cheap 3D printing system, for the fabrication of nigrostriatal guidance devices which might later be used as a basis for the connectoid system of the OpenMIND project[47] (see section 1.3). To this aim a workflow for volumetric 3D printing of PDMS had to be developed by the author first. After the main obstacles to PDMS extrusion had been solved different design concepts were thought out and used for prototyping of guidance devices. The workflow, design and printing parameters were gradually refined to optimize quality and reproducibility of the prototypes and make the workflow more efficient. An envisioned peculiarity of the 3D printed was that they would be detachable after cell cultivation such that they could be removed from the substrate without inflicting damage on the axonal fascicles of the organoid cultures. To achieve this a wafer passivated with 1H,1H,2H,2H-perflourodecyltrichlorosilane (FDTS). Due to the flat surface of the (passivated) wafers the bottom surface of the printed devices will be extremely smooth which provides for strong adhesion and possible even tight sealing. An early prototype of the guidance devices was used for the cultivation of hVM1 spheroids to investigate their suitability as a fast-growing substitute for brain organoids during the prototyping of electrochemical bioplatforms like the envisioned connectoid system[47]. Since no formation of hVM1 spheroids has been reported at the time of the project different conditions for their formation were tested and evaluated. The final prototypes were handed to our project partners at Lund University where they were tested for the cultivation of brain organoids. An illustrated overview of the project and the allocation of tasks is given in Figure 7. In order to increase the ease of reading this thesis the design and fabrication of the guidance devices and the cell cultures will be discussed separately with the following subtopics:

- **Volumetric 3D Printing of detachable PDMS devices:** conceptualization and testing of a workflow for 3D printing of PDMS using the volumetric 3D printer "FelixBIO" with a focus on PDMS extrusion & height alignment (z-alignment) and an estimation of the developed printing methods in respect to quality of the devices and reproducibility of their structural features. Design of the nigrostriatal guidance devices and applied considerations to tackle problems with the cultivation process or the printing process respectively.

- **Spheroid & Organoid cell cultures:** Since the organoid culture was done by project partners at Lund University the focus will be laid on the description of the spheroid culture which was done by the author. Here experiments were made to investigate beneficial conditions for the generation of hVM1 spheroids and the cultivation of hVM1 spheroids was tested in 3D printed guidance devices with a naïve approach to get a first evaluation of the suitability of these devices for cell culture.

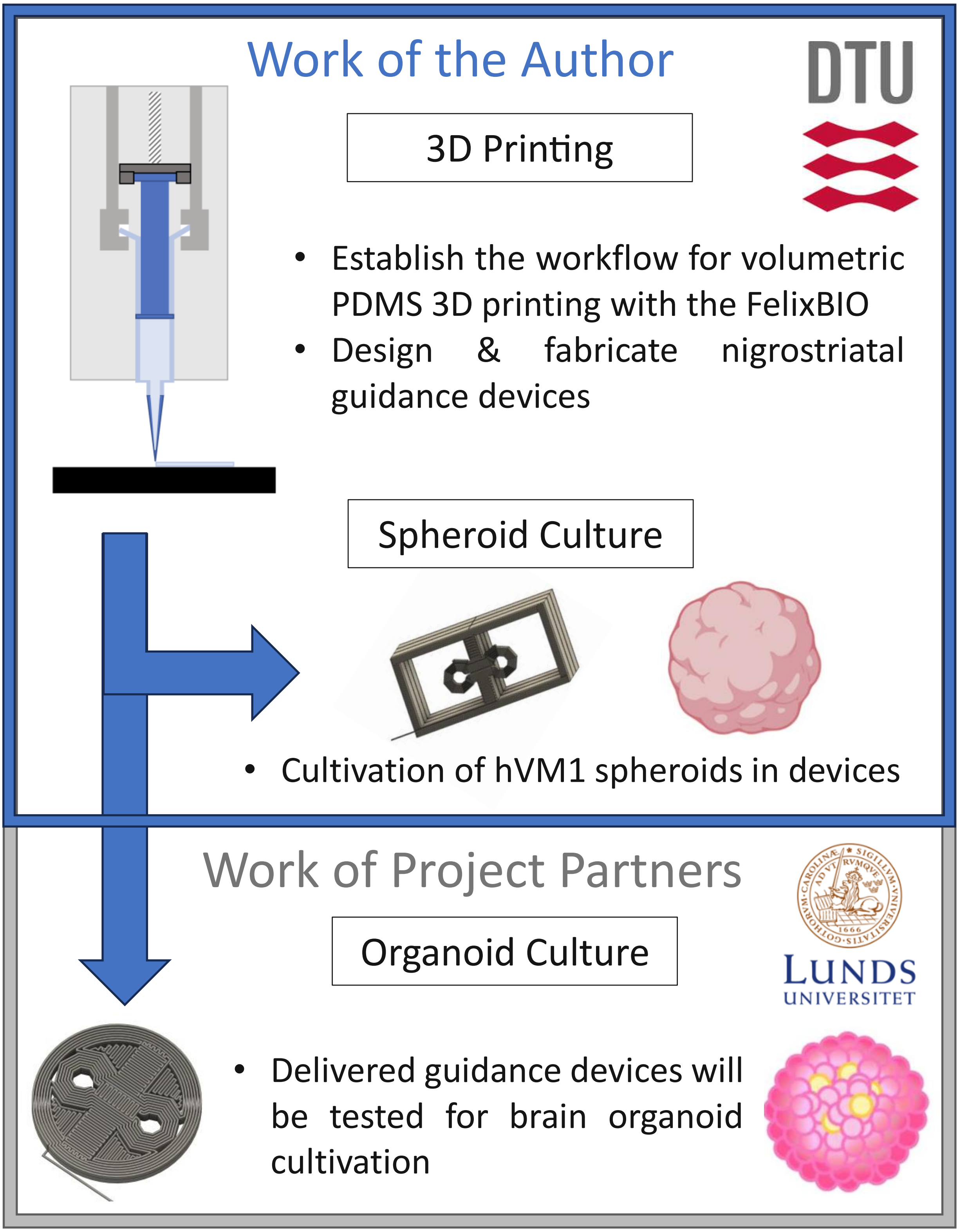

Figure 7 Project overview and allocation of work tasks. For the fabrication of nigrostriatal guidance devices, the author will first develop a workflow for volumetric PDMS 3D printing with the FelixBIO. Having found a way to fabricate PDMS with the given printing system the author will then design and fabricate different guidance devices. During this prototyping of devices, the gathered understanding will be used to optimize the 3D printing workflow in an iterative process. The author will then use his guidance devices for cultivation of hVM1 spheroids. Since no protocols for hVM1 spheroids were reported at the time of this project, different conditions for spheroids formation will be investigated. To test the guidance devices for the cultivation of brain organoids, which is their primary envisioned purpose, they will be transferred to Lund University where they have expertise with brain organoids and can compare the author's 3D printed guidance devices to already established systems. The images used for spheroid & organoid were taken from [37] and [38].

In order to illustrate the work done an experimental outlook is given in Figure 8. In this figure spheroid is meant to include organoids. This block diagram serves both as an abstract illustration of the work done for this thesis and as a workflow to fabricate 3D printed objects with the tested printing systems. This workflow could be used for a plethora of experimental devices to fulfill diverse criteria. The procedure for 3D printing was developed by the author and the methods for prototype design were created to fulfill the needs of the printing process. They will hence be discussed in the results part. Another Major block was in the optimization of the conditions for spheroid formation. This block was put in dashed lines because it was only done during in this project for spheroids and not for organoids and because it is not necessary part of the pipeline.

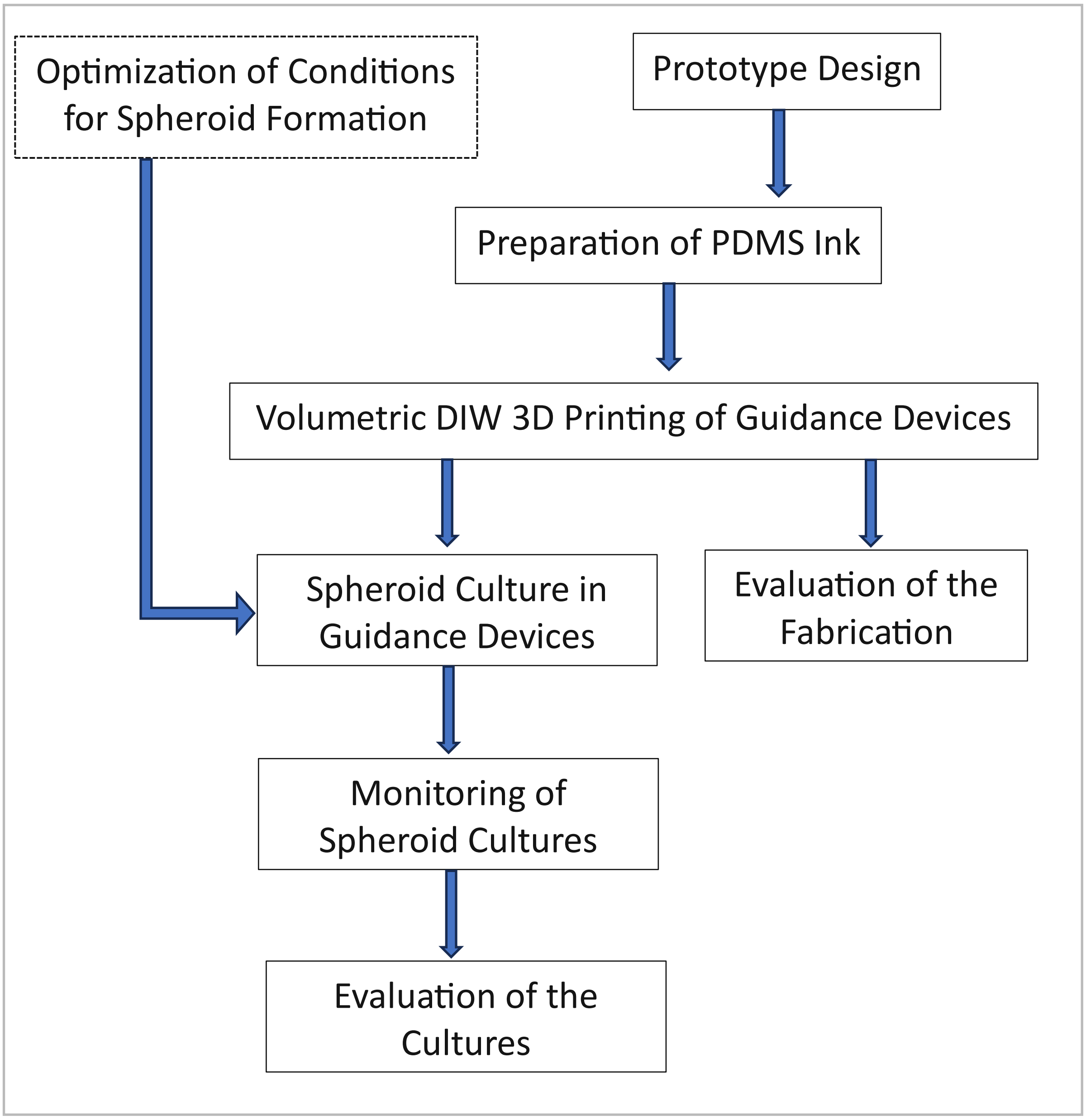

Figure 8 Block diagram of the thesis and of the suggested workflow. The block “optimization of Conditions for Spheroid Formation” was put in dashed lines because this part was only done for spheroids by the author and is not necessary part of the workflow in general. For the other blocks spheroid can also be understood in the sense of organoid.

The only blocks that were mostly based on established methods are "Preparation of PDMS INK and the Monitoring of Spheroid Cultures". These blocks will therefore be thoroughly discussed in the "Methods" sections (2.4). The rest will be discussed in the "Results" (3) or "Conclusions" (4) section. A description of the used materials will be given in the following section, while the used tools will be the next section.

2.1 Materials

This section will give a short description of the used materials for 3D printing and cell culture. In respect to printing this section will cover the PDMS and the printing substrate since there will be a tools sections that refers to the machinery. In respect to the spheroid culture this section will discuss the used cell lines, the coating agents and the culture medium.

2.2.1. PDMS

For a device to be suitable for cell culture certain criteria must be met. Most importantly the material that is in contact with the cells must be biocompatible meaning that their proximity does not cause harm to them. This criterium is known to be met by several materials like the metals silicon and palladium, a number of ceramic alloys or some plastics like polystyrene as it is used for most well-plates. Most of these materials have severe limitations like their opaqueness in the case of metals and ceramics or the lack of proper fabrication methods for rapid prototyping in the case of polystyrene. An additional criterium in our specific case is permittivity for oxygen since otherwise the low diffusion in the device channels might lead to cell death. All of these criteria are met by silicone material polydimethylsiloxane, better known as PDMS[53]. The best known PDMS in biomedical research is Sylgard 184 from DOW which is used heavily in stereolithography. Since this material does not meet the rheological criteria for Direct-Ink-Writing as discussed in section 1.4 it was not possible to use to here. A PDMS material which has already been used for 3D printing is DOWSIL SE1700[63] from DOW. This material is non-flowing at rest, has a good adhesion and is heat curing. Devices fabricated with DOWSIL SE1700 are less transparent than the ones fabricated with Sylgard 184. DOWSIL SE1700 is reported to be biocompatible but since it is not an established standard like Sylgard 184 the suitability of SE1700 for long-term culture might not be given. A possible vector for the introduction of cell toxicity might be the heat-curing crosslinker of SE1700 that has different functional chemical groups than Sylgard 184. One of the many benefits of PDMS is that it can be bonded to glass using processes like plasma bonding. A prerequisite for leakage-tight long-term bonding is a near-perfectly flat bottom surface of the devices which can be very hard to achieve. One method that can be used to fabricate devices with a near-perfectly flat surface is printing on passivated wafers.

2.2.2. Printing Substrate and Passivation

As discussed in the previous paragraph near-perfectly flat bottom surface are a prerequisite for the bonding of a devices on a glass surface. In this work the plan was to print detachable devices that can be removed after organoid culture such that the axon fascicles of the connectoids can be set free for analysis without inflicting any damage on them. This exacerbates the need for flatness even more and necessitates strong physical interaction between the fabrication material and their new substrates. There are two approaches that can be used to remove a printed device from a substrate without inflicting any damage to it: the first approach is to print on a substrate and then dissolve the substrate and the other approach is to print on a passive substrate where the ink has only very low adhesion. Since it is not trivial to produce such dissolvable substrates, especially with the requirement on flatness the second approach has been used. Near-perfectly flat substrates are available as silicon wafers as they are used in lithography and their silicon surface reacts readily with some chemical agents like silanes which can be used for passivation. In this sense a wafer passivated with 1H,1H,2H,2H-perflourodecyltrichlorosilane (FDTS) was used as a printing substrate. The molecular structure of FTDS is shown in Figure 9. Passivation with FDTS based on long hydrofluorocarbon chains than form monolayers on the substrate when the silane reacts with the surface atoms.

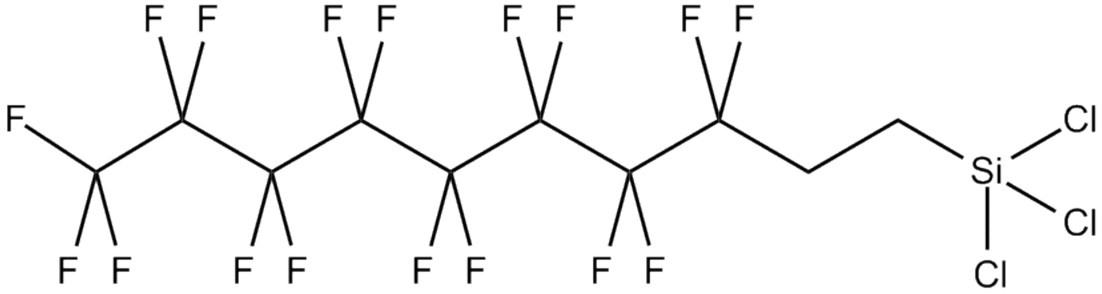

Figure 9 Molecular structure of 1H,1H,2H,2H-perfluorodecyltrichlorosilane (FDTS). The graphic was taken from [64]

Unfortunately, the exact protocol which was used for the passivation of the wafer is unknown since the researcher that performed the procedure had left DTU and the no precise notes could be found. It is assumed that the passivation was done with chemical vapor deposition (CVD) since passivation of wafers with FTDS is a commonly applied method in the research group where this step was done. FTDS can also be used in wet approach for passivation (wet-silanization), but there can be grave differences in the quality of the passivation due to different kinetics and the physicochemical differences between gas-solid interfaces and liquid-solid interfaces. A possibility might be that some fraction of the passivation-agent adheres after detachment on the printed material and then leaks into the cell medium during culture. This might have deleterious effects on the cells which might only manifest in long-term culture and might thus be less likely to have been reported.

2.2.3. Cells

While organoids are usually made from embryonic stem cells or human-induced pluripotent stem cells spheroids are often made from progenitor cells. This is largely because organoids are wanted to resemble functional organs and these protocols are used that partially recapitulate the embryonic development during their maturation (see section 1.2) and spheroids are usually wanted to have uniform cells. The origin of the cells for the organoids used at Lund University and their applied protocols are at this point confidential since they are part of ongoing research, but they are partially based on previous experiments conducted in their research group[65]. For the spheroid the progenitor cell line human ventral midbrain 1 (hVM1) was used due to its high yield in dopaminergic neurons which might lead to the readily formation of axonal fascicles in microchannel. hVM1 is a polyclonal, immortalized, and multipotent cell line isolated from the ventral mesencephalon of a 10-week-old human fetus[66, 67]. Since no protocols for the formation of hvM1 spheroids were available different conditions were tested (see section 3.2.2.) in order to find the best protocols that might help to use hVM1 spheroids as a fast-growing replacement of brain organoids during the prototyping of microelectronic devices like the connectoid system (see section 1.3). The cell medium used for these experiments were based on 2D protocols established by partners of the OpenMind project. The spread of axons on a substrate is largely a function of the applied coatings which will be discussed after the cell medium.

2.2.4. Cell Media

One medium was used to grow hVM1 cells as 2D cultures in flask which will be referred to as proliferation medium and a different medium was used to induce dopaminergic differentiation after spheroid formation which will be referred to as differentiation medium. This was done because cells need to be in culture for at least two weeks before their differentiation to conform to scientific standards and since differentiated cells have low proliferation. The differentiation is necessary to resemble mature cells like they mostly make up the substantia nigra. For the preparation of proliferation medium and differentiation medium a basal medium was prepared and sterile filtrated according to Table 2. This basal medium was stored at 4°C for up to a month and was used as a basis for proliferation medium and differentiation medium. For their preparation N_2 supplements and non-essential amino acids were added to the basal medium and further factors were added to each medium specific according to Table 3. Proliferation medium and differentiation medium were stored at 4°C and used within a week. For preparation of the non-essential amino acid solution the respective amount of water was heated to 55°C and the amino acids were added in the order indicated by Table 4 followed by 15 min of stirring and sterile filtration.

Basal Medium

Table 2 Formulation of basal medium: The compounds used for medium preparation are listed as well as their provider, catalogue number (cat. number) and their concentration in the final solution.

Compound	Provider	Cat. Number	Conc.
AlbuMAX-I	Gibco	11020	1.25 g/L
DMEM/F12(1:1) with Glutamax	Gibco	31331-028	solvent
HEPES	Gibco	15630-056	5 mM
Glucose	Sigma	G7021	6 g/L
Penicilin/Streptomycin 1000x	home made		0.1 v/v

Proliferation Medium & Differentiation Medium

Table 3 Formulation of proliferation medium and differentiation medium. Basal medium according to Table 2 was used as a basis for both media. N_2 and AANE were added for both whereas hrEGG & hrFGF-2 were specific to proliferation medium and GDNF and cAMP were specific to differentiation medium. AANE-solution was prepared according to Table 4.

Compound	Provider	Cat. Number	Conc.
N_2 supplements	Gibco	17502-048	0.1 v/v
Non-essential amino acid solution	home made		0.1 v/v
specific to proliferation medium			
hrEGF	R&D Systems	236-EG-200	20 mg/L
hrFGF-2	R&D Systems	233-FB-025	20 mg/L
specific to differentiation medium			
GDNF	Peprotech	450-10	2 mg/L
Dibutyryl cAMP	Sigma	D0627	2.5 g/L

Non-Essential Amino Acid Solution

Table 4 Formulation of non-essential amino acid (AANE) solution: H_2O was heated to 55°C and the respective amount of AA was dissolved under stirring for 15 min followed by sterile filtration. The amino acids were obtained from Merck and the CAS Registry Number (CAS RN) was given for each AA.

compound	CAS RN	per liter
L-alanine	1.01007	3.92 g
L-asparagine monohydrat	1.01565	6.00 g
L-aspartic acid	1.00126	5.32 g
L-glutamic acid	1.00291	5.88 g
L-proline	1.07434	4.60

2.2.5. Coatings

Since most substrates used for cell culture do not provide for adhesion of cells coating of the substrates is a standard procedure. The coating has a major influence on cellular behavior due to their different potential for interaction with biological matter. Two different coatings were used which are poly-L-lysine and Geltrex. PLL is mostly used for proliferation of stem cells due to its lack of trophic factors and ECM proteins, but its successful application in hVM1 dopaminergic differentiation has been reported[68]. In addition, patterns of different PLL densities have been shown to guide neuritogenesis and redirect axonal growth along their lines through interaction with the filopodium[69, 70]. Geltrex is a basal membrane extract that resembles physiological conditions *in vivo*[71] and contains proteins that are known to be associated with growth cones[72] and support of dopaminergic differentiation[73, 74].

In addition to the materials used in these section different reagents had been used for cell staining after the culture experiments. Since the monitoring of the cell culture will be a block thoroughly described in the "methods" section the used staining agents will be discussed there. Before the discussion of the methods the tools in the sense of machines and software used for the experiments are discussed.

2.3. Tools

This section will first discuss the mixer used for PDMS preparation and then the FelixBIO 3D printer. This will be followed by a discussion of the software used for 3D design and slicing. The last discussed tools will by the microscopes used for imaging. A more thorough discussion of the preparation of the PDMS ink is given in section 2.4.1 and the procedures used for 3D printing and for prototype design are given in section 3.1.4.

2.3.1 DAC 150.1 FVZ SpeedMixer & FelixBIO Printer

PDMS is used together with a crosslinker that forms stable bonds between the PDMS polymers after curing. PDMS and crosslinker are stored separately and are only mixed together before PDMS is used for fabrication. Because the used PDMS DOWSIL SE1700 is very viscous the material was mixed with its crosslinker in a DAC 150.1 FVZ SpeedMixer during ink preparation. Although PDMS and crosslinker can be mixed by manual stirring the DAC provides a more reproducible mixing process and might thus prevent problems caused by inhomogeneities. The data sheet of the DAC 150.1 FVZ SpeedMixer is given in Table 5.

Table 5 Datasheet of the DAC 150.1 FVZ SpeedMixer[75]

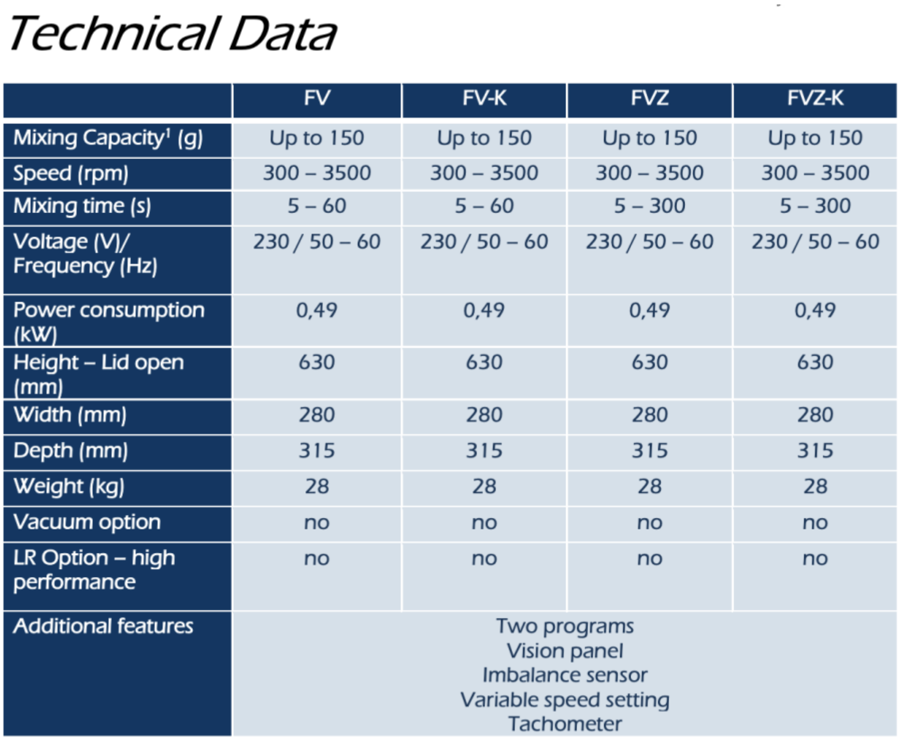

Technical Data

	FV	FV-K	FVZ	FVZ-K
Mixing Capacity^1 (g)	Up to 150	Up to 150	Up to 150	Up to 150
Speed (rpm)	300 – 3500	300 – 3500	300 – 3500	300 – 3500
Mixing time (s)	5 – 60	5 – 60	5 – 300	5 – 300
Voltage (V)/ Frequency (Hz)	230 / 50 – 60	230 / 50 – 60	230 / 50 – 60	230 / 50 – 60
Power consumption (kW)	0,49	0,49	0,49	0,49
Height – Lid open (mm)	630	630	630	630
Width (mm)	280	280	280	280
Depth (mm)	315	315	315	315
Weight (kg)	28	28	28	28
Vacuum option	no	no	no	no
LR Option – high performance	no	no	no	no
Additional features	Two programs Vision panel Imbalance sensor Variable speed setting Tachometer			

The DAC is a planetary mill and a quartz ball with a diameter of one centimeter was used for grinding. The mixing is based on dual asymmetric centrifugation where the mixing arm spins in one direction while the basket the sample is mounted in spins in the opposite direction. Centrifugation was then done at 4500 rpm for 4 to 8 minutes depending on the PDMS volume in the syringe.

The FELIX BIOprinter (FelixBIO) from the company FELIXprinter, formerly Felixrobotics, is a comparativelz inexpensive 3D printer as illustrated in Figure 6. The FelixBIO is a volumetric syringe-extrusion based 3D printer that works with a mechanic and electronic framework that is largely derived from the company's FDM printers. The extrusion of the FelixBIO is implemented through a Portescap 35DBM-L linear actuator stepper motor with a holding torque of 40 N that exerts mechanical force on the plunger of a syringe through a screw mechanism (Figure 14/A). The specifications of the machine are given in Table 6.

Table 6 Specifications of the FelixBIO 3D printer taken as from [76].

Specifications

Layer Resolution	to 50 microns
Build Plate	Aluminium sandwich plate with steel flexplate or optionally glass plate
Print head	Dual motorized syringe operation
Syringe Specs	5 ml Luer lock or luer slip syringe
Build Speed/s	Recommended build speed is 20 mm/s. Speed depends on material viscosity
Typical print x,y,z accuracy	± 0.05 mm for sizes below 20 mm
Syringe Min/Max print temperatures	4-75 ˚C
XYZ resolution	XY: 1.6 microns, Z: 0.15 micron
Dimensions & Weight	430 x 390 x 550 mm, 11.5kg
Build Volume	XYZ = 130 x 210 x 130 mm
Extrusion width	Greater than 0.1mm, depending on nozzle size
Extrusion force of syringe	350N max

The printhead can be readily equipped with 5 ml and 3 ml syringes and smaller syringes can be used with an adapter. The printer is therefore based on technology and software that is derived from the RepRap project[56], which had the aim of creating self-replicating open-source 3D printers. In this sense the FelixBIO uses the same 5-dimensional g-codes as ordinary home-owned FDM printers which are x, y and z coordinates, printing speed f and extrusion e. While in FDM printers e describes the movement of the screws that push the filament through the nozzle this coordinate describes the movement of the plunger that extrudes the ink. The similarities of the FelixBIO to RepRap printers and the cheap price (see section 1.4) of such system make this machine a good candidate to evaluate the potential of open-source volumetric 3D printers for PDMS printing. G-codes for the FelixBIO can be generated by slicer software that take 3D models as input and create a printing path with the respective e coordinates that are calculated as a function of the printer settings. G-codes from different slicers can be used on the FelixBIO but only Simplify3D and Repetier-host are supported by the manufacturer. More informations on the FelixBIO can be found in the doctoral thesis of Hakan Gürbüz[77] who worked on the machine. The software used to make 3D models and their subsequent printing script generate with a slicer are described in the next section.

2.3.2. Software for 3D Modeling & Slicing

The used software for 3D modeling was Fusion360 which is an application for computer-aided design (CAD). The software is developed by Autodesk and although it is a commercial software a free version is available for students[78]. Fusion360 has a plethora of features that can be applied in computer-aided manufacturing and computer-aided engineering, but most of them have not been of relevance since the software was only used to make STL files. STL is the standard file format for models used in 3D printing and is based upon triangulation to create scalable objects. The Interface of Fusion360 during the design process is shown in Figure 10 Interface of Fusion 360 during the preparation of STL files for 3D printing.

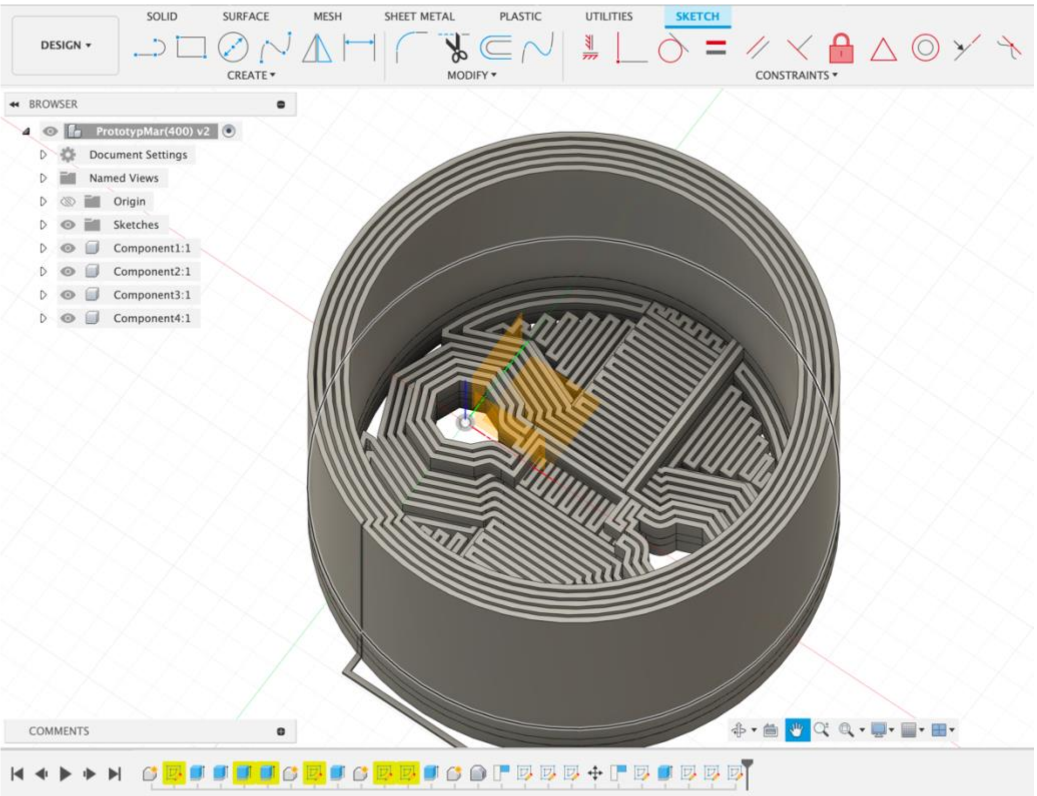

Figure 10 Interface of Fusion 360 during the preparation of STL files for 3D printing.

The used software for slicing was Simplify3D (S3D). Slicing is the process where a computer numerical control (CNC) code for 3D printing is created from a 3D model like an STL file. This CNC code is usually written in the programming language RS-284, better known as g-code. S3D was conceptualized for FDM printing but the same code can be used for volumetric DIW. The interface of S3D during slicing for FDM printing is shown in Figure 11.

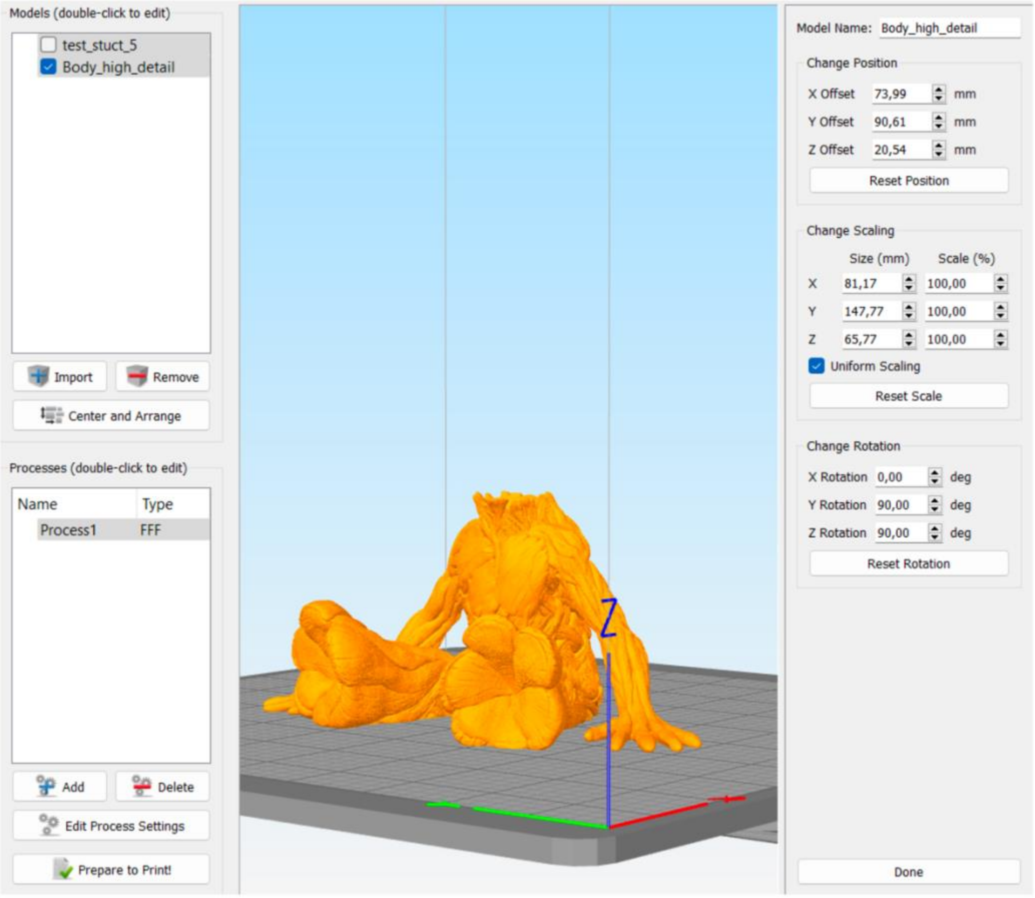

Models (double-click to edit)
☐ test_stuct_5
☑ Body_high_detail

Processes (double-click to edit)

Name	Type
Process1	FFF

Model Name: Body_high_detail

Change Position
X Offset 73,99 mm
Y Offset 90,61 mm
Z Offset 20,54 mm

Change Scaling

	Size (mm)	Scale (%)
X	81,17	100,00
Y	147,77	100,00
Z	65,77	100,00

☑ Uniform Scaling

Change Rotation
X Rotation 0,00 deg
Y Rotation 90,00 deg
Z Rotation 90,00 deg

Figure 11 Interface of Simplify3D during slicing for FDM printing.

The g-codes generated by S3D are 5-dimensional scripts where the three dimensions of x,y and z control the translation of the printhead and the dimension E (for extrusion) controls the movement of the plunger that exerts the extrusion force on the loaded ink which is then again influenced by the fifth dimension of printing speed (f). The advantage of S3D in comparison to other slicers was that S3D can also be used to control the FelixBIO via a machine panel. The exact procedure how the prototypes were designed are given in section 3.1.4. The following chapter gives information about the used microscopes.

2.3.3. Microscopes

For imaging of the 3D printed devices a Zeiss Axioskop 40 Polarized Light Microscope and a Dino-lite digital microscope were used. For image analysis the open-source software ImageJ-MicroManager-1.4 was used. For imaging of the cell culture, a Zeiss AxioObserver Z1 inverted epifluorescence microscope equipped with 5x (EC Plan-Neofluar 0.16 M27), 10x (EC Plan-Neofluar 10x/0.30 Ph1, Zeiss^{TM}, Germany) and 20x magnification (LD Plan-Neonfluar 20x/0.4 Korr M27, Zeiss^{TM}, Germany) objectives was used. The images from the cell culture were then processed with the software Zen (Zeiss^{TM}) and Fiji NIH. The epifluorescence microscope was especially used for fluorescence microscopy after staining. The procedures for cell staining are described at the end of the “methods” section.

2.4. Methods

This section focuses on the formulation and handling of the PDMS ink and the monitoring of the spheroid cultures since they were the only experimental parts that were mostly based upon existing procedures. The printing procedures will be discussed in the results part since the development of the procedure was an ongoing process and can only be understood considering the initial results. The exact condition for spheroid culture are also given results section, but mostly to give this information in proximity to the results to help with the interpretation.

2.4.1. PDMS Ink Preparation & Curing

Since the project partners from DTU Health Tech already had experience with DIW 3D printing of PDMS their methods for formulation and handling of PDMS ink could be used readily for the project. It should be noted here that their experience with PDMS printing was limited to high pressure pneumatic extrusion and that their ink formulation may hence be suboptimal for volumetric printing due to the difference in applied extrusion force. Following their formulation DOWSIL SE1700 clear base silicone and DOWSIL SE 1700 catalyst were mingled in a weight ratio of 1:10 and mixed for 3 min at 3000 rpm with a DAC 150.1 FVZ SpeedMixer from Hauschild. The PDMS/crosslinker solution was then transferred into 5 ml Braun omnifix solo syringes which were then placed in 50 ml falcon tubes for centrifugation. The syringe was placed in the tubes with the plunger facing downwards to avoid the formation of an air layer between plunger and PDMS as shown in Figure 12.

Figure 12 Preparation for PDMS centrifugation. The PDMS was centrifuged in a 50 ml falcon tube with the plunger facing downwards to avoid the formation of an air layer between plunger and PDMS ink.

Centrifugation was then done at 4500 rpm for 4 to 8 minutes depending on the PDMS volume in the syringe. The prepared ink was used directly after preparation if possible and the ink would become unusable for printing after 3-4 hours the latest. After printing the substrates with the prints were put into a Termaks 1056U oven at 50°C o/n as a first curing step to stabilize the form of the printed PDMS. The PDMS ink is capable of curing at room temperature but since this process takes longer than overnight and the availability of the wafer was a limited factor for the printing this approach was not feasible. In a second step the temperature of the oven was set to 150°C for at least 90 min to prevent problems with the biocompatibility of the material. The temperature at the curing steps may have significant influence on the printed devices due to the macromolecular processes during curing and shrinkage but this factor was not further investigated due to the limited time.

2.4.2. Monitoring of Spheroid Cultures

During cell culture images were taken with polarized light microscopy and for the final analysis the cell cultures were reversibly stained with live/dead staining and then permanently stained using methods from immunocytochemistry. Live/dead staining was only done at the end of the culture since the author was unsure about the handling and did not want to risk early cell death. During immunocytochemistry antibodies are used to target specific immunomarkers and these markers are then visualized with secondary antibodies. A prerequisite for immunocytochemistry is the fixation process which aims to prevent the degradation of the samples due to cell death at the end of a cell culture. Since no protocols for hVM1 spheroid fixation were available established protocols for 2D cultures were adapted for the longer times necessary for mass transport into the interior of spheroids. Unfortunately, this approach led to damage to the protruding axons for the spheroids transferred on day 4 & 7 the duration of each step was reduced again to the original times of the 2D protocols for the spheroids with later transfer days. For fixation the first group was kept for 30 min in 4% (v/v) paraformaldehyde in PBS and washed twice with PBS for 5 min. The second group was kept for 2 minutes in 2% (v/v) PFA in PBS and for 4 min in 4% PBS for fixation and washed twice with PBS for 5 min. For permeabilization/blocking and immunocytochemistry the times for the later transferred spheroids will be given in brackets. For permeabilization & blocking the spheroids were kept for 6 h (or 1 h for the second group) in STPBS solution. For the formation of the STPBS solution Triton X-100 was dissolved in PBS under stirring for a final concentration of 0.3 % (v/v) before goat serum and horse serum were added to a concentration of 1 % (v/v) each. Afterwards the spheroids were incubated with rabbit polyclonal anti-tyrosine hydroxylase and mouse monoclonal anti-β-tubulin III primary antibodies diluted together 1:1000 in STPBS for 48 hours (O/N) at 4°C. Afterwards the antibody-solution was removed and the samples were washed with STPBS for 30 min (10 min), then with 0.3 % Triton X-100 in PBS for 30 min (10 min) and then with PBS for 30 min (10 min). After this the samples were incubated with Alexa 546 goat anti-mouse (1:500) and Alexa 647 goat anti-rabbbit (1:500) together with Hoechst 33342 solution (1:5000) in PBS for 24 h at 4°C (30 min). The secondary antibody solution was then removed, and the sample washed twice with PBS for 30 min (10 min). For live/dead staining the samples were washed 3x with PBS in preparation and then incubated for 20 min in 0.5 ‰ (v/v) Invitrogen™ calcein AM & 2 ‰ (v/v) Invitrogen™ ethidium homodimer-1 in PBS for 20 min in the incubator at 37°C. Imaging for both live/dead staining and immunostaining was performed with the Zeiss AxioObserver Z1 inverted epifluorescence microscope and Zen software while Fiji NIH was used afterwards for analysis. The images acquired with this microscopy are given in the “results” section.

3. Results

An overview of the experimental work is done in section 0. The volumetric printing of PDMS will be discussed first and then the cell cultures. At the beginning of each of these two blocks a summary will be given for the 3D printing or the cell cultures respectively. An overview of the entire experiments is given in Figure 8.

3.1. Volumetric DIW 3D Printing of PDMS

The reason to use a volumetric 3D printer was the lower cost of such system which can be orders of magnitude lower than state-of-the-art pneumatic printers as discussed in section 1.4. The goal of this work was to use volumetric DIW 3D printing of PDMS for the fabrication of nigrostriatal guidance devices. These devices could then form the basis of the connectoid device envisioned by the OpenMIND project (see section 1.3). Since volumetric 3D printing of PDMS is not an established process several problems had to be tackled to print PDMS at all and then to print PDMS devices in a reliable and reproducible process. An overview of the discussed blocks is given in Figure 13. These blocks will be discussed as if they were in chronological order although they were mostly done in parallel.

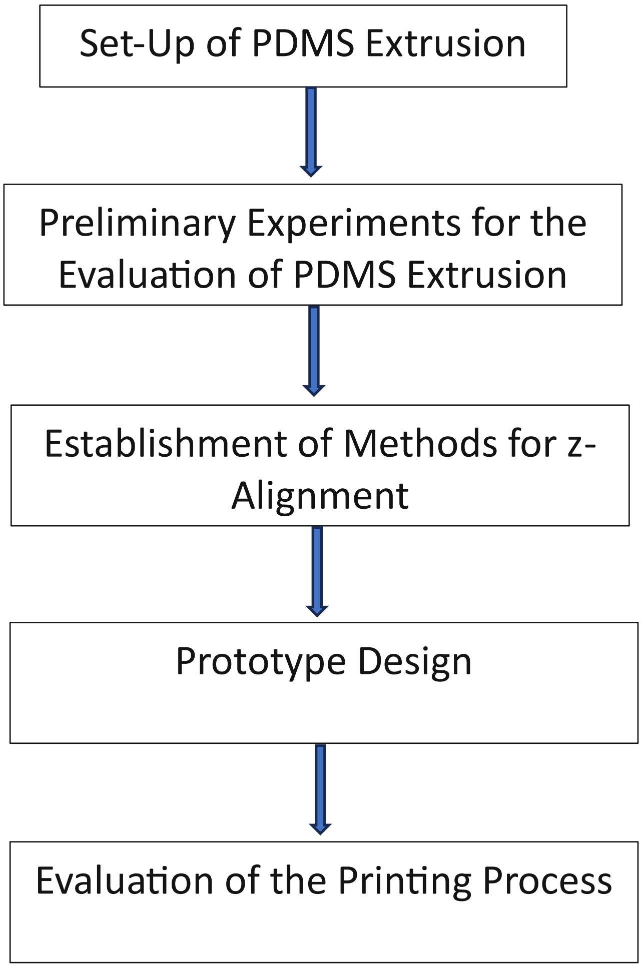

Figure 13 Overview of the establishment of the procedure for volumetric DIW 3D printing of PDMS.

Since the fabrication of the guidance devices necessitated the print of microfluidic channels on the bottom side this put a very large demand on the printing process in respect to the z-alignment since this would have a massive influence on the channel width due to squeezing of the PDMS ink during extrusion in the bottom layers. The problem with the z-alignment used to regularly cause variations of the channel width of several hundred microns especially in the early days of the experiments such an emphasis was laid on the reproducibility of the printing process in respect to channel width. The channel width can be assumed to be a critical feature of the guidance devices since its features are an important mechanical cue for the axons. The problem with the reproducibility remained until the end and possible procedures that might alleviate this problem further in the future are given in the “outlook” section. The first discussed section is the set-up of PDMS extrusion since the materials viscosity caused severe problems in the beginning which had to be solved before the problem of z-alignment could be tackled in a meaningful way.

3.1.1. Extrusion & Printer Setting

The facilitation of PDMS extrusion through a small nozzle is not a trivial question due to the high mechanical resistance. Since no reports of experiments were found where volumetric extrusion of PDMS was used for 3D printing this was the first major obstacle to be tackled in during this project. The extrusion of the FelixBIO is implemented through a Portescap 35DBM-L linear actuator stepper motor with a holding torque of 40 N that exerts mechanical force on the plunger of a syringe through a screw mechanism (Figure 14/A). 5 ml Braun Omnifix syringes with Cellink 27G precision tapered nozzle tips with an inner diameter of 200 μm were used in analogy to experiments conducted on a RegenHU 3DDiscovery printer[54]. Due to the shear-thinning characteristics (Figure 14/B) of the PDMS in combination with the low extrusion force of the system it is not possible to achieve monotonous extrusion with a monotonous extrusion force, but complex extrusion profiles are neither supported by the slicer software nor the printer. Shear thinning characteristics of the ink are a prerequisite for 3D printing but usually either high pressure is applied which remedies the influence of the complex rheological characteristics or low viscosity materials like hydrogels are printed with volumetric control were the applied extrusion force is much higher than the mechanical resistance. The 27G nozzles, which were specifically wished-for by one of the supervisors, introduced the additional problem of high resistance against extrusion which made the ink effectively behave like a Bingham pseudoplastic (Figure 14/B) such that either no extrusion or excessive extrusion would be the consequence of monotonous extrusion settings. Since the extrusion force cannot be directly determined by the g-code volumetric extrusion factors had to be used as a proxy to manipulate the extrusion force. In particular the extrusion is controlled by the 5-dimensional g-code where the three dimensions of x,y and z control the translation of the printhead and the dimension E (for extrusion) controls the movement of the plunger that exerts the extrusion force on the loaded ink which is then again influenced by the fifth dimension of printing speed (f). The exact control of the extrusion force that the FelixBIO would apply as a result of the passed g-code commands is obscure, but it was observed that the jog control commands for larger extrusion (e.g. 1 mm) would apply a stronger extrusion force than the jog control commands for incremental extrusion of the same volume (e.g. 10 x 0.1 mm) such that only the commands for larger extrusion volumes would overcome the resistance in high gauge nozzles. The first successful PDMS prints with the FelixBIO with 27G nozzles were achieved by writing a start script that would include the extrusion of 0.3 mm and the printing would then proceed with a continuous extrusion profile. This approach would

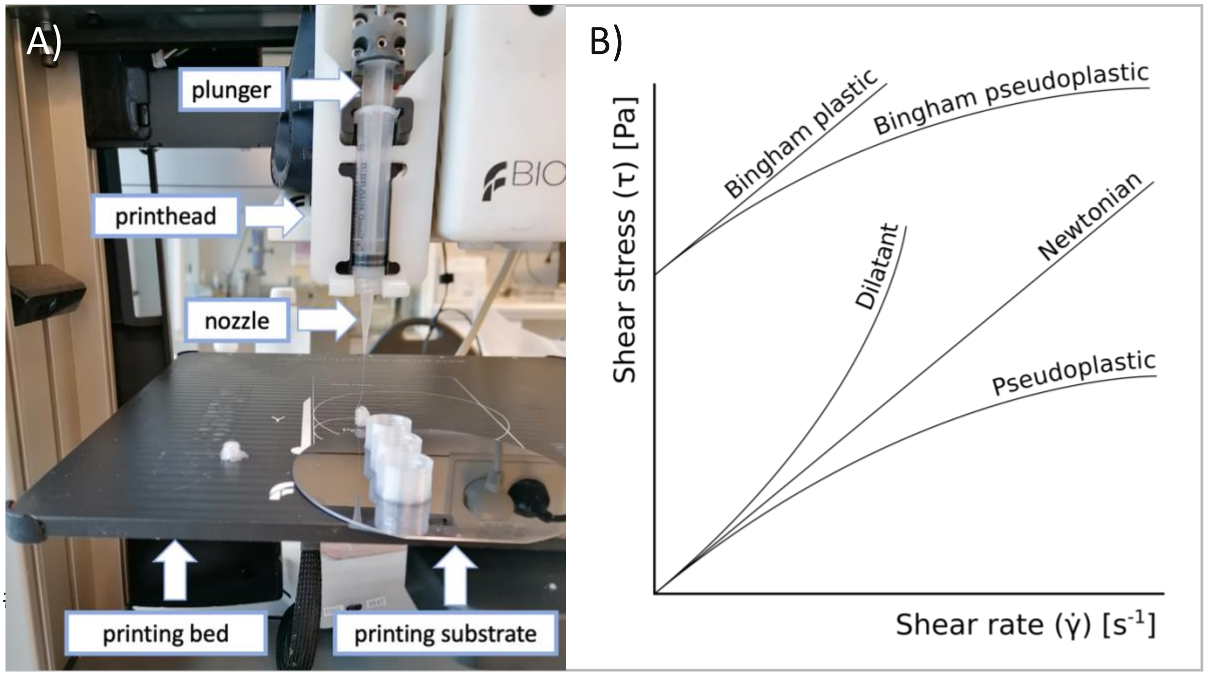

Figure 14: Basic components of a volumetric DIW-3D printing system (A) and characterization of different rheological profiles (B) (graphic taken from [79]). The printhead has a screw mechanism that works on a plunger to control extrusion through the nozzle. Printing bed and printhead are moveable in XYZ direction. Printing bed and (printing) substrate refer to the printer's stage and to the material onto which the ink is printed. The used substrate was a passivated wafer to enable detachment and re-attachment of the devices as explain in 2.2.2. A pile of PDMS can be seen under the nozzle which is the result of retarded mechanical equilibration after the printing process. Inks for 3D printing are generally shear-thinning (or pseudoplastic as in (B)) since they must be solid at rest but fluid during extrusion. Shear thinning means that the viscosity of an ink will decrease with the velocity of extrusion which can lead to different extrusion profiles at the start of a printing process. A Bingham pseudoplastic ink is a shear-thinning material that requires a certain threshold force or shear stress to initiate a flow. It should be noted that the decrease of viscosity with printing time might also be a result of thixotropy of the PDMS ink, but thixotropy of SE1700 is not reported by the manufacturers[80] and thixotropy and shear-thinning can be hard to distinguish without rheological measurements.

enable continuous PDMS extrusion, but the extrusion would be increased at the beginning of the printing since the plunger would apply an overpressure on the PDMS ink due to its inability to execute the extrusion demand which would only relax after some minutes. Although the PDMS extrusion seems to stabilize with printing time PDMS extrusion will not stop after the printing process leading to a pile of PDMS on the printing bed (Figure 14/A). This post-print extrusion can be prevented by implementing a retraction (or negative extrusion in S3D) in the ending script. To account for the increased flux after the start of the extrusion, voluminous pre-prints were designed to be printed on a timescale of 5-10 minutes to allow for a stabilization of the ink extrusion before the desired structures were printed. The starting script was later removed, and the extrusion was instead started with the jog control which would allow to let the extrusion somewhat stabilize before the printing would be started with execution of the g-code. The preprints were kept for stabilization of the extrusion which might now be upregulated or downregulated depending on the extrusion at the moment of passing of the g-code for execution. In summary it can be said that the small nozzle size posed a significant barrier for mechanical equilibration, but this might have been a significant feature of this printing method.

Early experiments to determine the extrusion width were conducted but as it will be explained in section 3.1.2. In order to investigate the influence of the extrusion multipliers in combination with the printing speed early prototypes were printed and evaluated in respect to the likelihood of failed prints due to problems of over, - and underextrusion or structural disintegration as well as in respect to a perceived smoothness of the print. The extrusion multiplier increases the amplitude of plunger displacement in respect to x and movement. With low viscosity materials the relationship between extrusion multiplier and extrusive flux could be considered linearly, but due to the observations explained in the last paragraph it cannot be assumed that this was the case with this printing set-up. The extrusion multiplier was varied in order to find the best compromise for reproducible printing in respect to extrusion width and subsequent channel width and the prevention of underextrusion which might cause problems with structural instability of the devices as well as leakage. The printing speed was varied in order to find the fastest speed possible for printing without risking failed prints due to delamination of adjacent lines. The first layer height was varied since slower printed basal layers decreased to change of printing problems similar to the case with FDM printing. During these experiments g-code scripts were used that had a distance of 300 µm between adjacent lines of the printing path or in other words a necessitated extrusion width of at least 300 µm to print closed structures. During these experiments the parameters in Table 7 were fixed.

Table 7 Principal printing parameters set in S3D. The first group of parameters was fixed during all experiments and the second group was varied during preliminary experiments. The chosen values for the determination of extrusion width are given in the third column.

Fixed Parameters	Setting	
Filament Diameter	12.00 mm	
Nozzle Diameter	0.20 mm	
Extrusion Width	0.20 mm	
Primary Layer Height	0.15 mm	
First Layer Height	100%	
First Layer Width	100%	
Varied Parameters	**Range**	**Chosen Value**
Default Printing Speed	480 – 600 mm/min	480 mm/min
Extrusion Multiplier	1.00 – 1.20	1.00
First Layer Speed	50 – 100 %	50 %

Printing speed from 480 to 720 mm/min were successfully used for printing, but 480 mm/min were chosen for further experiments because it was assumed to lead to the lowest variability although this might not be the case. Another reason was that with 600 – 720 mm/min printing problems started becoming more common after they had been used successfully and the reduction to 480 mm/min appeared to have prevented these problems. Since the problems with higher printing speeds appeared with an increase in temperature due to summertime it was hypothesized that this might have been the cause. Similarly, first layer speed was reduced to 50 % because with this speed the least problems would be observed. The extrusion multiplier had the least problem with a value of 1.20 but was reduced to 1.00 because it was assumed to increase the reproducibility at it seemed to provide for a stable extrusion.

3.1.2. Preliminary Experiments for the Evaluation of PDMS Extrusion as a function of the printing procedure

Having established a reliable method to start PDMS extrusion different experiments were envisioned to characterize the PDMS extrusion as a function of printing height, printing speed and extrusion multipliers. As a first experiment the influence of the bed unevenness on the extrusion with should be tested with a systematic approach. To this aim two analogue patterns of two-layered lines were printed alternatingly, either from left-to-right or reverse (Figure 15), on Hounisen 76 x 26 mm object glasses. All samples were printed on the same location on the printing bed. The results of these experiments are shown in Figure 16.

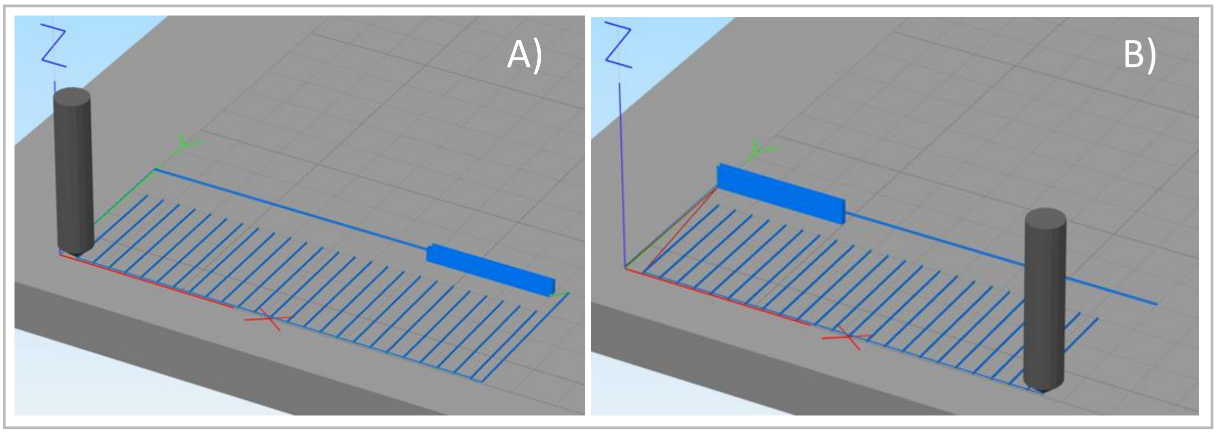

Figure 15 Illustration of the preliminary experiments into the extrusion width where arrays of two-layered lines were printed alternatingly from right to left (A) and from left to right (B) to minimize the influence of bed unevenness. The fact that the extrusion width decreased to both directions with every printed line (Figure 16) indicated that stable extrusion would have required much bigger preprints since the bed unevenness should have otherwise caused a decreasing or increasing extrusion width in opposite directions. These experiments were discontinued mostly due to problems with the unevenness of the used substrate and since the introduction of larger preprints would introduce additional problems.

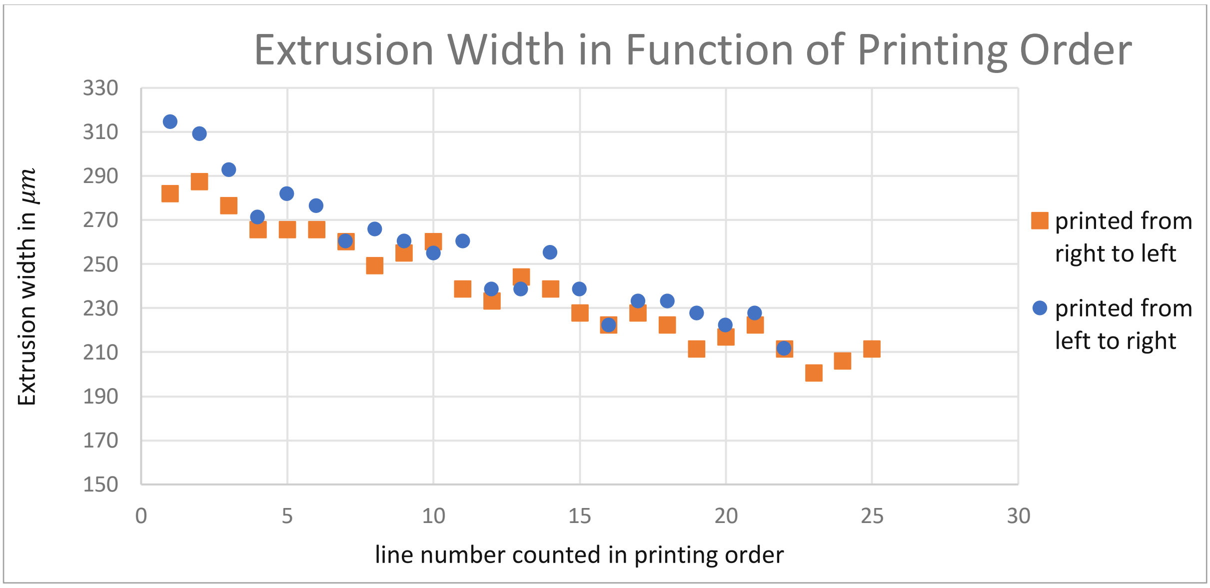

Figure 16 Plot of extrusion width as function of printing order. The numbers on the x-axis indicate the printing sequence. These findings indicated the need for excessive pre-prints to stabilize the extrusion to reproducibly print structures.

Unexpectedly both experiments led to a decrease in extrusion width along the order of the printed lines instead of the location on the printing bed which indicated that excessive pre-prints would have been necessary to stabilize the extrusion. This would have made the experiments unfeasible since the aging of the PDMS ink and the fullness of the syringe would have introduced more variables that would have to be controlled. Another reason why these experiments were stopped was because the surface unevenness often led to grave damages to the nozzle. The applied ISO 8037/1 allows for differences in thickness of 300 µm between maximum and minimum which proofed them unsuitable for the purpose, but no viable alternative was available. The inclusion of even larger preprints would have further introduced problems with the aging of the ink. Another reason for the discontinuation of these investigations was the question of the translation from printing on glass substrates to printing on fluor-functionalized wafers (for passivation see section 2.2.2) due to different surface interactions. During preliminary experiments with the same nozzles an assumed extrusion width of 300 µm was successfully used to fabricate closed 3D structures and was thus kept for the fabrication of the guidance devices. Although 3D printing usually assumes an extrusion width close to the nozzle diameter it was refrained from doing this since it did lead to clogging of the nozzle in some experiments. Since these experiments could neither be used to optimize the printing parameters nor for the characterization of the printing process it was decided to evaluate them with the print of the final device prototypes.

3.1.3. z-Alignment

The alignment of the print head in respect to printing bed or substrate is one of the most important steps in 3D printing since it is obligatory for the printing of a solid base layer without which the printed layers will become displaced in respect to each other. For the fabrication of nigrostriatal guidance devices this step is especially crucial since the dimensions of the bottom layers form the channel for axonal penetration. Although the FelixBIO has an intrinsic mechanism for automatic height measurement (z-probing), this mechanism is neither very precise nor reproducible and results in nozzle damage. Different mechanisms were explored for z-probing that would increase the reproducibility and would prevent damage to the nozzle. The aim was to find reproducible methods to determine the distance between nozzle and substrate, either directly through contact with the substrate or indirectly through contact with a spacer device. When printing on a silanized wafer the most effective method for z-alignment was to fixate the wafer on the edge of the printing bed using double adhesive tape and to optically determine the z-position where the nozzle would get in contact with the wafer. Here a dino-lite digital microscope (dinocam) was used for magnification (Figure 17/A). The wafer was placed at the edge of the printing bed since only there contact between nozzle and substrate was properly determinable. Here the small mechanical backlash when lifting the nozzle from the wafer was used to determine whether the two had been in contact. With this method it was possible to do the z-probing with a reproducibility of around 10 µm and in a relatively fast and direct way. The wafer had been cut on two edges which allowed for a more precise z-alignment. Another method was the fabrication of spacer devices (Figure 17/B-F) that would either be tipped when or start vibrating through nozzle movement when the distance between nozzle and printing bed is low enough (Figure 17/F). This method had the advantage that it was easier to use in the middle of the printing bed, but this method was much slower, needed external calibration and introduced several other complications. The main advantage of this method was that it would not be influence by the mechanical moveability of the syringe in the holder in z-direction (Figure 20). Since it was observed that the nozzle was moved in z-direction as a function of movement of the plunger this moveability had to be determined for

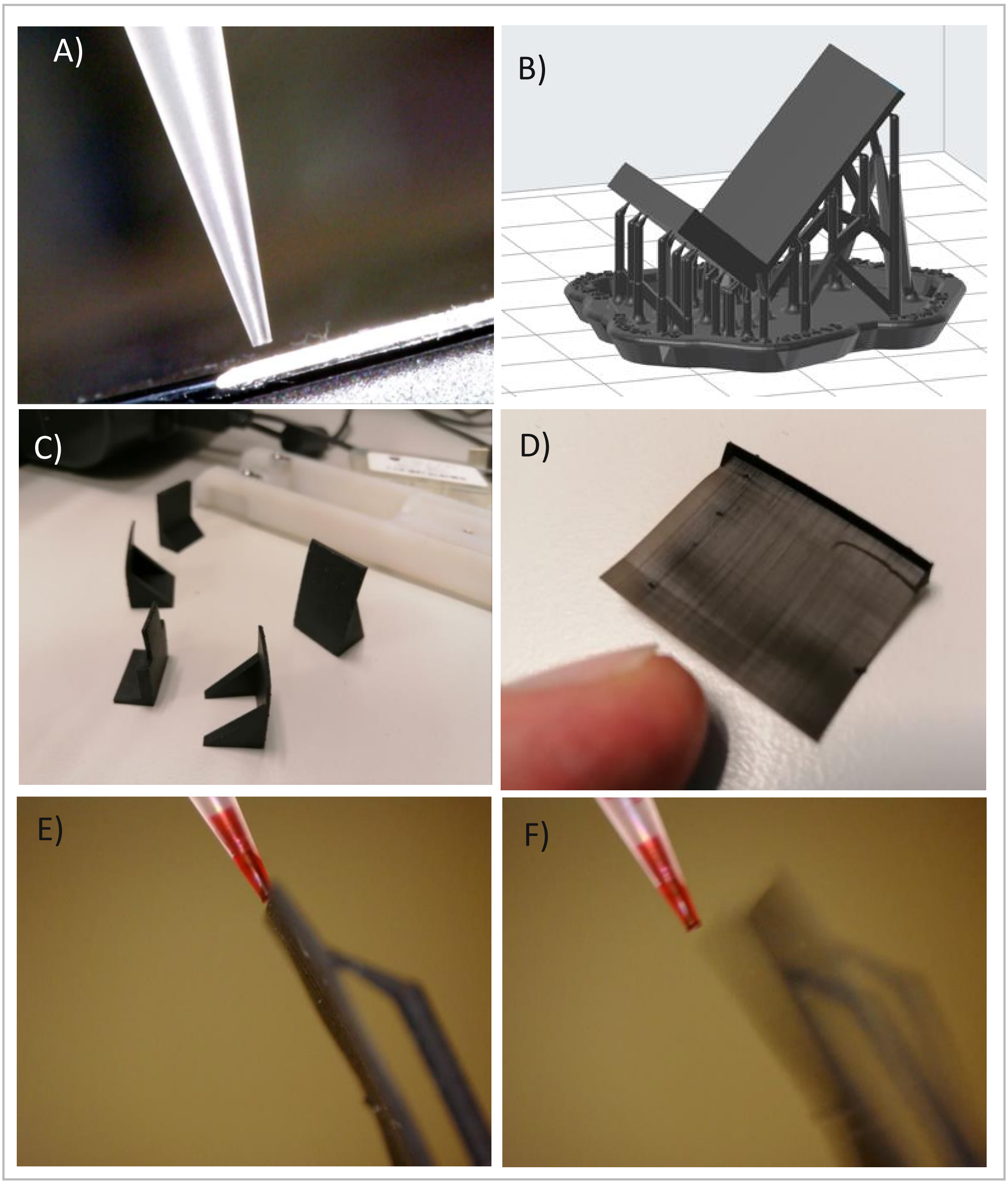

Figure 17 Methods used for z-Alignment. Optical height alignment using a dinocam (A). The edges of the wafer were cut which enabled better z-alignment since contact between nozzle and substrate can be determined best on the edges of substrate and printing bed. For an alternative approach to z-alignment spacer devices (C-D) were created with SLT printing (B) and used for z-probing. In this approach the nozzle was repeatedly moved over the spacer device and its distance to the printing bed was reduced in every round until physical contact between nozzle and spacer was recognized through vibrations or toppling (E-F). Although this method was not used for z-alignment due to the need of external calibration this method proofed effective to determine the influence of piston movement on nozzle height or the unevenness of the printing bed.

z-correction to assess the effective initial layer height. To this aim the spacer method was applied to an unloaded syringe first with retracting the plunger until no change of the nozzle position could be determined via dinocam and afterwards the plunger was moved downwards until no movement of the nozzle could be determined and the spacer method was applied again.

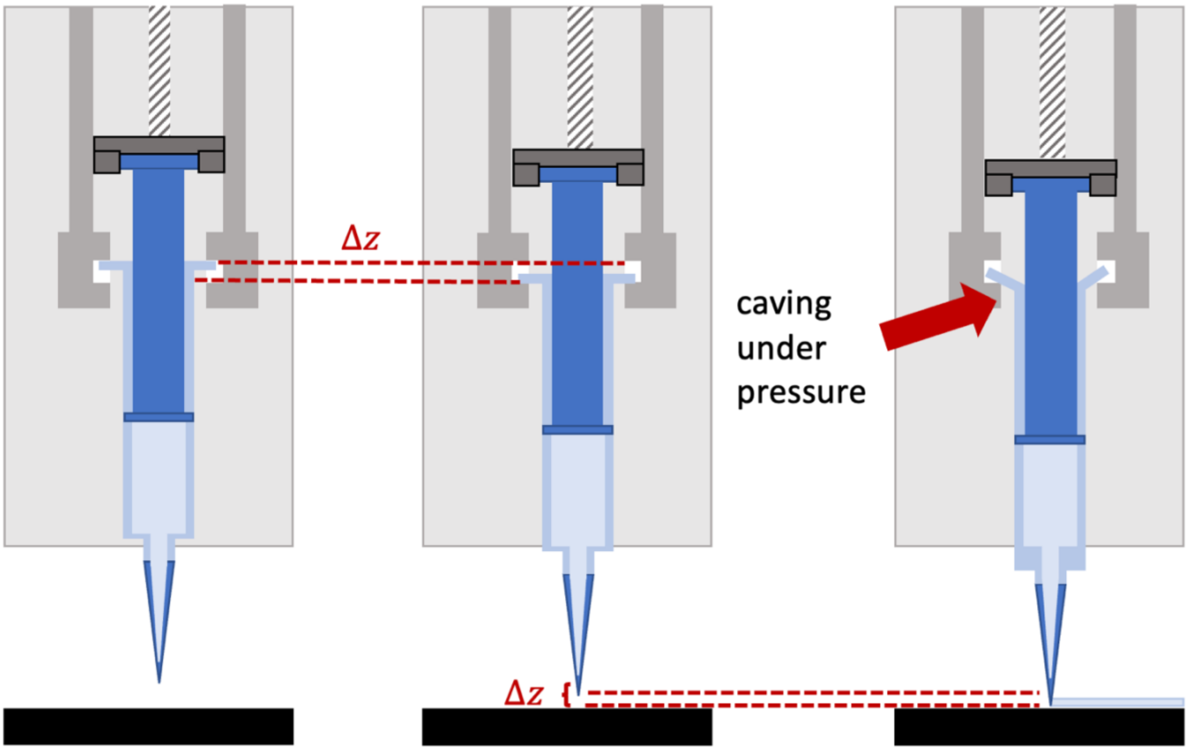

Figure 18 Contributions to the z-correction factor. The moveability of the syringe within the holder changes the nozzle-to-substrate distance as a function of piston movement. The difference between the highest and lowest position was estimated to be about 200 µm using a stereolithographically fabricated spacer device. Another factor is the caving of the syringe under mechanical pressure during syringe extrusion. Since extrusion would have interfered with the used methods for z-probing the influence of this effect could not be measured directly.

With this procedure a z-difference of about 200 µm was measured between the two states. Another complication that was observed was caving of the syringes under pressure, but since PDMS extrusion would have interfered with the measurement it was not possible to measure the effects thereof with the given methods. In order to determine evaluate the z-alignment z-correction factors of 50, 200 and 350 µm were tested by the printing of reduced versions of the two-chamber design (see section 3.1.4). A third reproducible method for z-alignment was the formation of aqueous bubbles around the nozzle that would burst when brought in contact with a glass substrate. This was not tested on wafers, but it presented a possibility for external calibration of the spacer devices. Since the described methods for z-alignment were only established after the guidance devices which were used for cell culture had been printed mechanical z-alignment had been used there. Herein the nozzle was lowered until a piece of paper could only hardly be moved between nozzle and printing bed and the nozzle was than elevated for 600 µm as a starting position and the substrate was placed in between. Since the mechanical alignment is very subjective and since it was not directly done on the substrate to prevent damage to the wafer the outcomes of the print were hardly reproducible. The specimen for cell cultures were handpicked by optical evaluation. The variations in channel width due to z-alignment were an important consideration during early prototype design.

3.1.4 Prototype Design & Slicing

Since the stereolithographically fabricated guidance devices from Osaki et al.[55] were used at the project partners at Lund university their design (Figure 19) formed the basis for the new designs. Since the well diameters were deemed rather short for organoid culture it was aimed to increased them to about 2.5 mm. In addition, walls for cell medium retention were added around the channels while in Osaka's device 8 channels are integrated into one device with outer walls. Different prototypes for guidance devices were developed either with two chambers to retained medium with different concentrations in morphogens or one chamber for cultivation with uniform medium composition. The two-chambers design was the earlier prototype and was tested for the cultivation of neural spheroids. Different one-chamber prototypes were fabricated of which design was transferred to Lund university where it was tested for the cultivation of midbrain-like organoids. One of the main considerations in the design of the one-chamber prototypes was the fact that problems with medium leakage occurred with the two-chamber design such that these prototypes had an increased bottom surface area to improve adhesion.

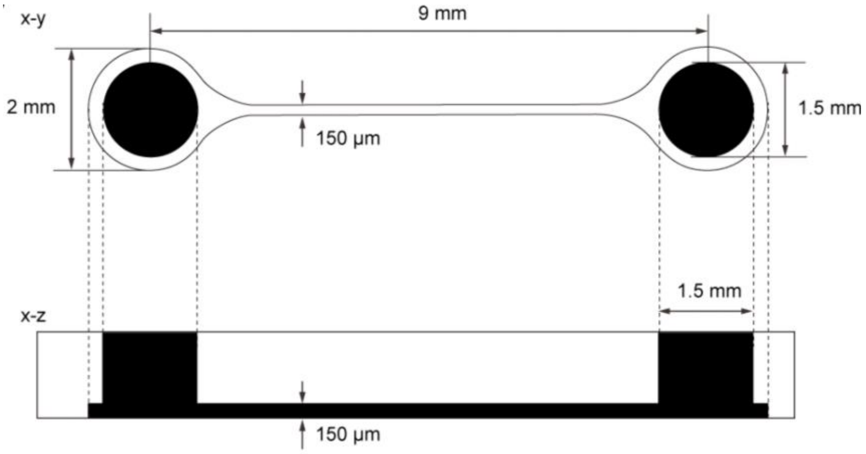

Figure 19: Channel system of the stereolithographically fabricated guidance device from Osaki et al.[55]. These devices were used at the project partners at Lund university and were used as a conceptual starting point for the design process. The graphic was taken from their paper.

The options that S3D has for the filling of 3D bodies from a CAD design proofed unsuitable for the realization of PDMS printing since ink retraction was not possible. This caused problems during printhead movement since the slicer would assume that no extrusion occurs thus leading to PDMS extrusion into the wells. To solve this the problem a method was developed which will be referred to as "semi-direct drawing of the printing path". Here the CAD software Fusion360 was used to model a hollow serpentine body with the outer dimensions of the desired structures (Figure 20, 21, 22 and 23). Given the right slicer settings the generated g-code files will include a printing path that corresponds to a line that follows the serpentine body from one end to the other in the exact middle of its width. To achieve multi-layered design a sketch was drawn for each desired printing layer that consisted of a single circuitous line with a width of 200 µm (Figure 20) such that the slicer would create a printing path that follows this line from start to end. Adjacent sections of this line mostly had a distance of 100 µm in accordance with the assumed extrusion width of 300 µm. This distance was reduced in vulnerable parts of the design where adjacent regions of the printing path would only share short parallel or anti-parallel segments (e.g. the lid design as depicted in Figure 20). This vulnerability is caused by anisotropic shrinkage of PDMS and by traction of the extruded PDMS string through printhead movement which can prevent tight sealing of the printed PDMS.

Another consideration in the CAD design was that the piston movement was not fully synchronized with the XYZ movement of the printhead which could result in extrusion problems for long lines. This would only be a significant problem in the case of free-hanging structures such as the channel lid which would demand kinks and shorter lines in the printing path.

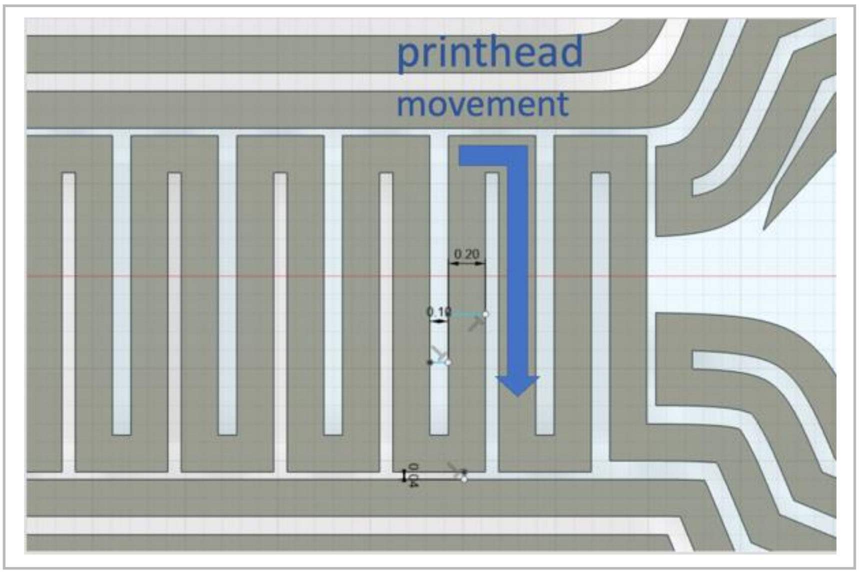

Figure 20: "Semi-direct drawing of the printing path" in Fusion360. STL files were created that contained 3D circuitous structure with an inner width that corresponds to the extrusion width as determined in the slicer software (200 µm). That way the printing path for each layer corresponds to the center line of each section of the body. The distance between the center lines of two section must correspond to the effective extrusion width in order to print closed structures. A distance of 300 µm between the center lines of adjacent sections was used since this distance proofed to be reliable in preliminary experiments thus resulting in a distance of 100 µm between adjacent sections in the CAD file. This distance was reduced in parts that were known from experience to be problematic, such as areas were adjacent sections only share a short border such as the sections forming the lid. A general reduction of the distance was avoided because of problems with clogging of the nozzle in preliminary experiments.

The two-chamber device was the first majored prototype and was designed to have two separate chambers that could host mediums with different gradients in growth factors via prevention of convection by filling the connecting channel with hydrogel. The channel width and the center-to-center distance were chosen to resemble the design of Osaki et al.[55] who fabricated organoid culture chips by PDMS casting into lithographically fabricated molds. The two-chamber design is shown in Figure 21 and had a theoretical channel width of 200 µm with an assumed extrusion width of 300 µm. The center-to-center distance between the wells was 9 mm and the CAD inner diameter of the wells was 2.650 mm. The design consisted of 4 different types of layers that repeated itself in multitudes of the printing layer height. The first design layer had a thickness of 750 µm and the second layer of 450 µm therefore corresponding to 5 and 3 printing layers respectively. The third and fourth layer were stacked as a pattern where 2850 µm layer 3 were topped by 300 µm of layer 4 therefore corresponding to 19 and 2 printing layers respectively. This pattern was repeated 3 times and was designed to prevent PDMS delamination along the printing lines. This design was conceptualized to have two chambers separated by a channel for axonal pathfinding which would be filled with hydrogel in order to slow down mixing between the two chambers. The aim was to be able to have different concentrations of morphogens inside each chamber such that different conditions could be applied simultaneously, but the use of hydrogel was not tested.

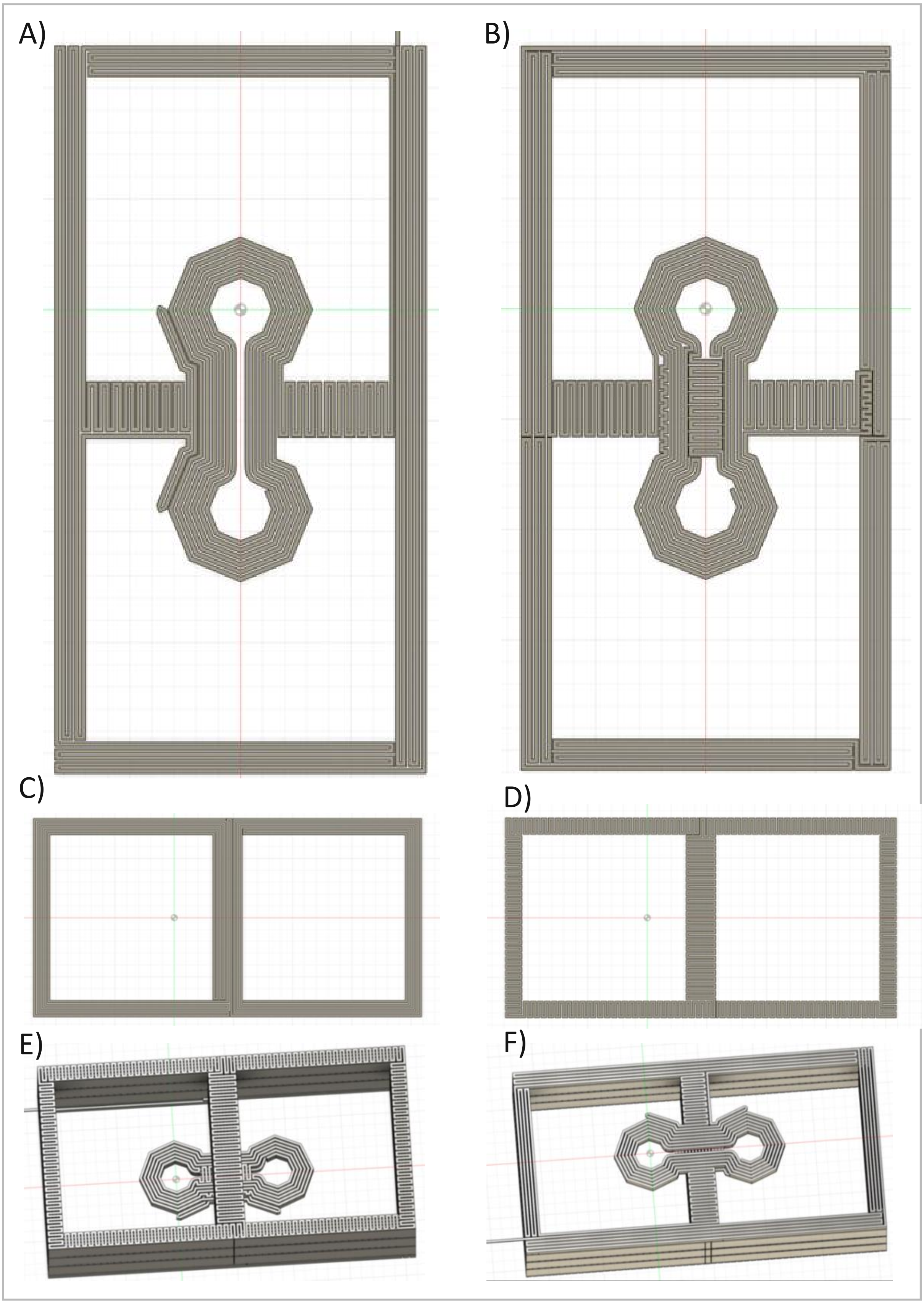

Figure 21 Two-chamber design of the guidance device. The two-chamber design consists of 4 different layers were the first layer (A) has a thickness of 750 µm and the second layer (B) of 450 µm corresponding to 5 and 3 printing layers respectively. The third and fourth layer were stacked as a pattern where 2850 µm layer 3 were topped by 300 µm of layer 4 corresponding to 19 and 2 printing layers respectively. The whole design is shown from the top in E and from the bottom in F.

The one-chamber prototype as shown in Figure 22 was the final prototype and included some changes which partially came from observations made from spheroid culture in the two-chamber devices. These designs were specifically designed to be used at Lund University to cultivate brain organoids on round glass slides with a diameter of 18 mm. Here the idea of two chambers was discarded to simplify the handling of the device. An important consideration in their design was the fact that problems with medium leakage appeared with the two-chamber prototype hence the bottom surface area was increased. The channel width was increased to a CAD width of 1000 μm since this was assumed to support the formation of axonal fascicles and the CAD wells diameter was 3.000 mm. The center-to-center distance of the wells was kept at 9 mm. The one-chamber design consisted of 3 layers where the heights of the bottom layer, middle layer (lid layer) and top layer were 900 μm , 300 μm and 10050 μm corresponding to 6, 2 and 67 printing layers respectively.

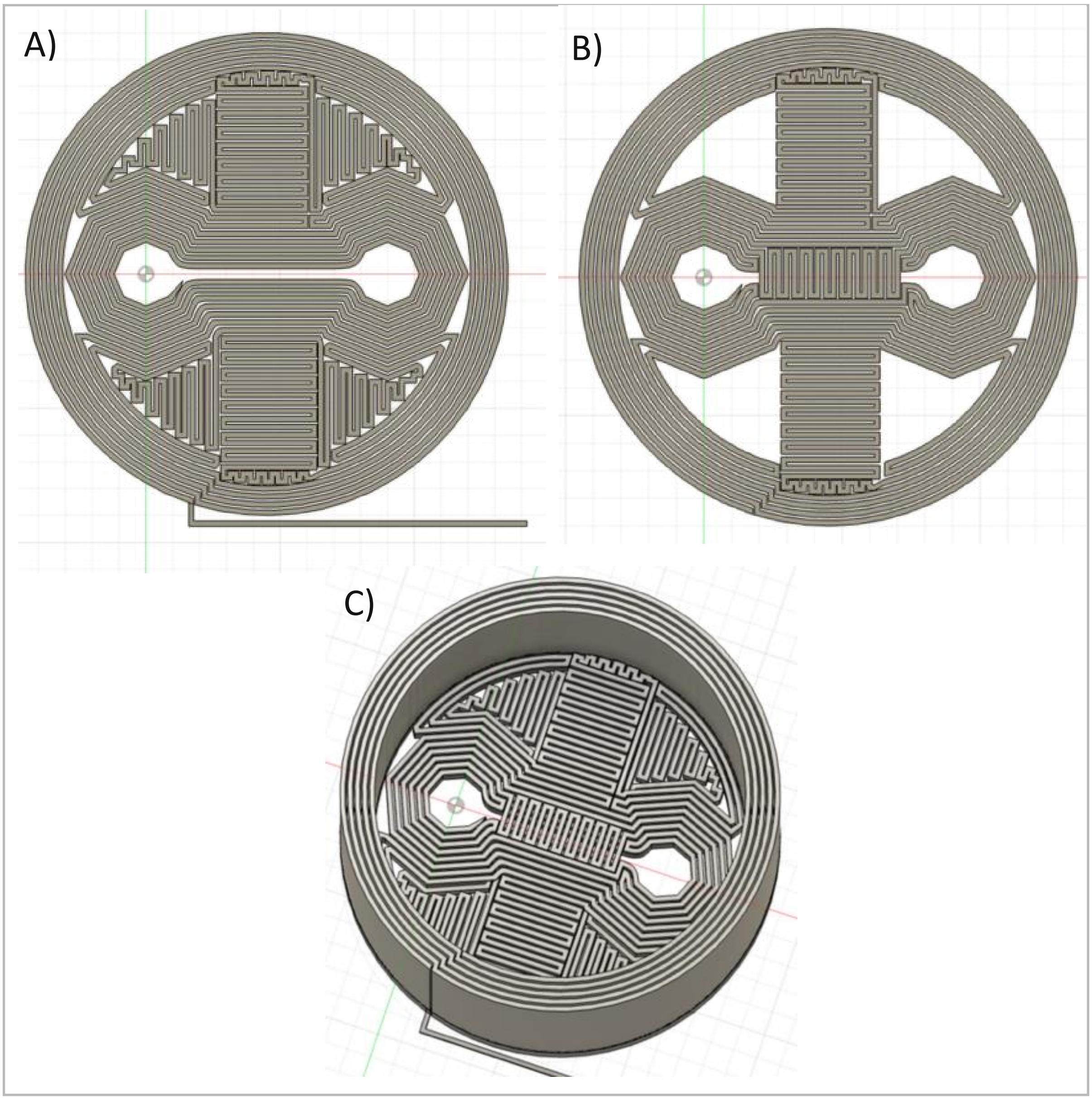

Figure 22 The one-chamber design of the guidance device. The one-chamber design consists of 3 layers were the first (A) has a thickness of 900 μm, the second (B) of 300 μm and the third (C) of 10050 μm corresponding to 6, 2 and 67 printing layers respectively.

The chamberless design as shown in Figure 23 was conceptualized as an alternative to the one-chamber design and had the same outer diameter and sizes in the well-and-channel system. This design was meant to reduce printing time through a reduction of height. Since this design lacked a medium reservoir, they would have to be used in an external well for medium retention. The chamberless design consisted of a 900 xc thick bottom layer and a 300 µm thick top layer corresponding to 6 and 2 printing layers respectively.

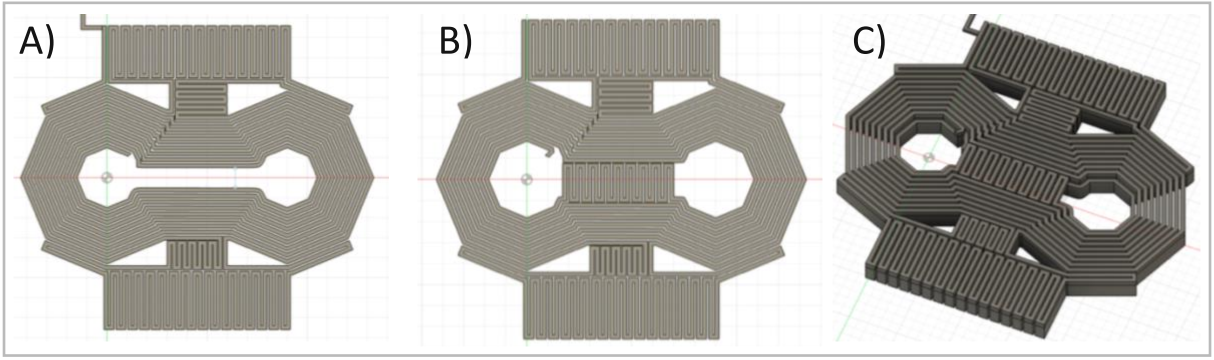

Figure 23 Chamberless design of the guidance device. The design consists of a 900 µm thick bottom layer (A) and a 300 µm thick lid layer (B). The assembled design is shown in C.

A reduced form of the one-chamber device (Figure 9) was used for the determination of printing reproducibility in respect to channel width and depth which will be discussed as the next chapter.

3.1.5 Determination of Printing Reproducibility in Regard to Channel Width and Depth

Since the real dimensions of the 3D printed structure are not only dependent on the extrusion width which could not be successfully determined in the preliminary experiments (see section 3.1.2) but are also subject to different deformational phenomena like creep or shrinkage during PDMS curing, the actual dimensions and the reproducibility of the printing process must be determined to evaluate the fabrication process. These investigations were only done after the printing of the prototype for spheroid and organoid culture since only then the methods for z-alignment were advanced enough to provide a significant level of reproducibility. Although the problems with the z-alignment and subsequent variability of the printing process were considered when it was decided to go for a broad channel in the one-chamber device the decision was rather made on the hypothesis that broader channels would be more suitable for brain organoids. To determine the reproducibility of the printing process a reduced form of the one-chamber prototype was printed in series of 2 columns with 3 prints per column (Figure 24/E). The reduced form consisted only of the bottom layer and lid layer of the original design. This reduction was done to increase the number of prints that could be printed per series since otherwise the process would be limited by the syringe volume. As a correction along the x-direction the z-probing on the wafer was done right before printing at the starting position of the first structure of each column and integrated into the g-code. Following PDMS curing the structures were detached from the wafer and put onto microscope slips. The channels were then filled with deionized water dyed with baker's color to prepare for imaging with a Zeiss Axioskop 40 Polarized Light Microscope in combination with the open-source software ImageJ-MicroManager-1.4. Because neurites tend to grow on the coated substrate rather than on PDMS walls the bottom width of the channels can be assumed to be the relevant dimensional aspect in contrast to the maximal bottom width which might be visible on the microscope images. Since the semi-transparent lid makes it hard to determine the bottom channel length (Figure 24/A) imaging was conducted upside down (Figure 24/B & D).

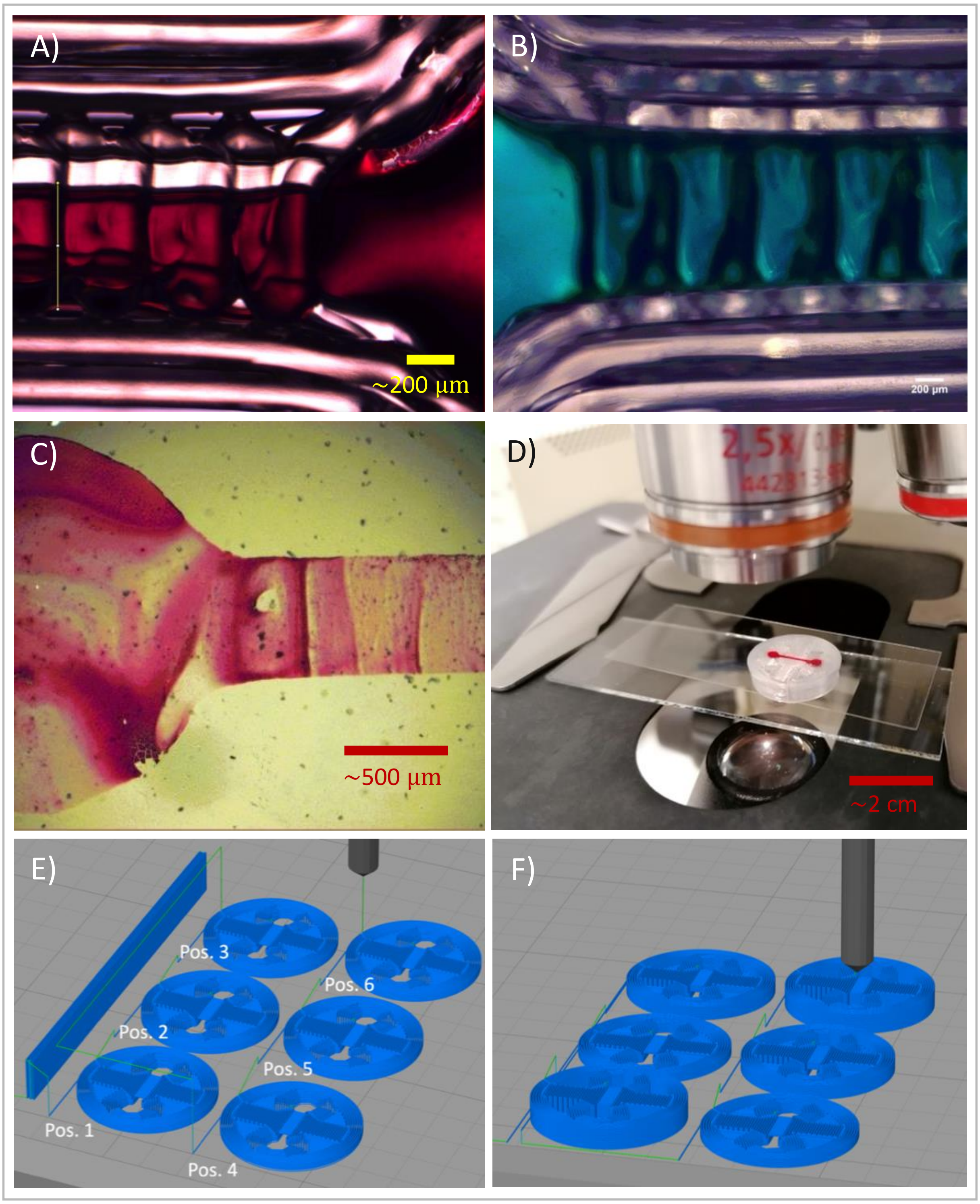

Figure 24 Microscope imaging and experiments for the determination of channel width and depth. Microscope channel images taken from the top (A) and from below (B). Microscope images from the bottom were taken as depicted in D. The image in C was taken during channel width determination with the dye-and-dry method were pigmental baker's color was dried inside the channel and imaged after removal of the PDMS device. This dye-and-dry method may be better suited to measure the bottom channel width, but not enough dye with fitting characteristics was available. For determination of the channel width a reduced form of the one-chamber design was printed in two columns of 3 pieces each (E). For each round of printing z-alignment was done at position 1 & 4 and their height difference was corrected using g-code. An analogue g-code was created to determine channel height as a function of lid thickness (100%, 300% and 600%) as depicted in F.

This method of upside-down microscopy yielded acceptable quality for the reduced form of the prototype but yielded poor images with full height. Alternative approaches for the measurement of the bottom channel width were the mechanical slicing and imaging or dying of the glass substrate through letting pigmental baker's color dry out in the channels. After the baker's color was dried out the residual pigments could be set free for imaging by removal of the PDMS structures. The drying method may be a superior method for quantitative determination of the bottom width, but this method is inherently slow and early removal of the prints often led to uninterpretable images and problems with reattachment of the structures. In order to determine channel depth and test the influence of sagging 3 variations of the one-chamber design were used where the third design layer was removed and the thickness of the lid layer was varied between 100%, 300% and 600% resulting in a thickness of 300 $\mu\mathrm{m}$, 900 $\mu\mathrm{m}$ and 1800 $\mu\mathrm{m}$ respectively (Figure 24/F). These prints were filled after curing with carbon black dyed DOWSIL SE1700 PDMS (crosslinker ratio 1:10) and the curing procedure was repeated. The prints were then sliced with a scalpel and imaged with the microscope. Each lid variation of the design was printed 4 times and the channel depth of each slice was measured at 3 positions. As discussed in the previous paragraph the channel width was measured for a reduced form of the one-chamber design with either a correction factor of 50, 200 or 350 $\mu\mathrm{m}$ for z-alignment. The correction factor of 50 $\mu\mathrm{m}$ did not yield successful prints due to clogging of the nozzle. The channel width achieved with the correction factors 200 and 350 $\mu\mathrm{m}$ were measured at 5 points and are shown in Table 9 while their mean is shown in Table 8. The 5 points were taken from one side of the channel to the other side such that the 1st and the 5th point were close the channel entries and the 3rd point was approximately in the middle. As it can be seen in Table 9 and Figure 25/B the channel width was usually slightly broader at the entrance of the channel. The channel widths far above 1000 $\mu\mathrm{m}$ in Table 8 and Table 9 were caused by internal leakage as seen in Figure 25/A.

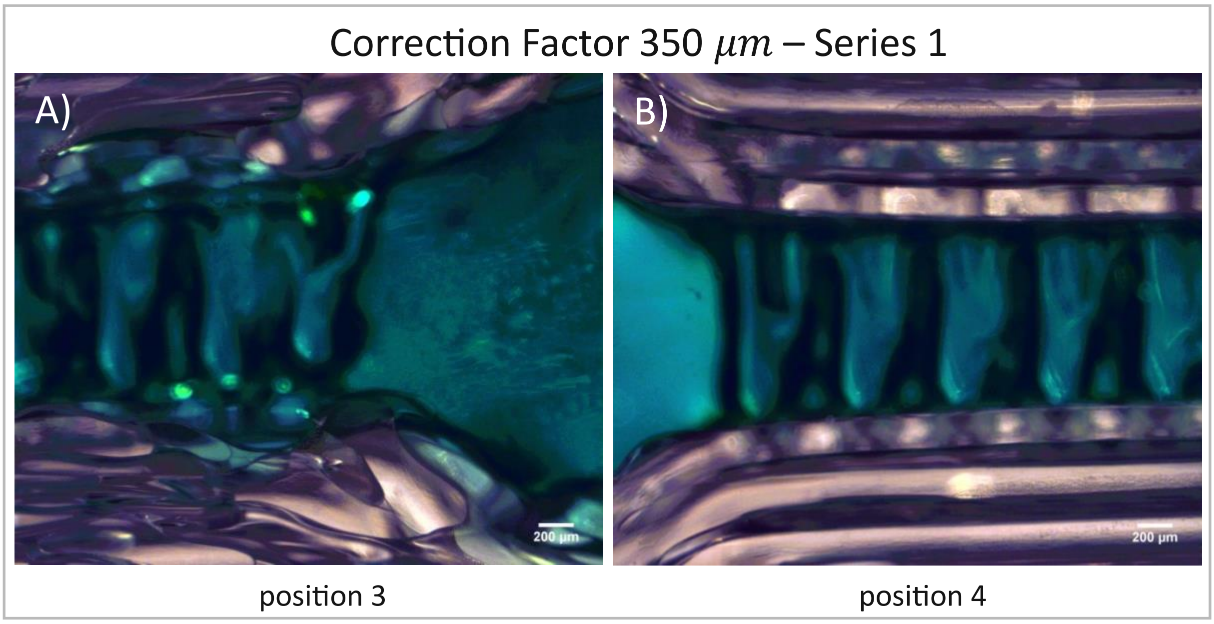
Correction Factor 350 μm – Series 1

position 3 position 4

Figure 25 Measurement of the channel width for series 1 with correction factor 350 μm. Image A shows the print in position 3 were internal leakage led to a very broad channel width. Image B shows the print in position 4 where the channel width appears rather uniform.

Table 8 Median measured channel width for the reduced one-chamber devices. Three correction factors of 50, 200 and 350 µm were tested and each correction factor was used in triplicates. The prints with the correction factor of 50 µm failed early due to clogging of the nozzle. The positions 1-6 correspond to the positions illustrated in Figure 24/E. The measured channel widths far exceeding 1000 µm were caused by internal leakage of the devices.

		Position					
		1	2	3	4	5	6
50 µm	All Series						
200 µm	Series 1	970	1041	954	980	923	1004
	Series 2	921	1089	965	889	1089	965
	Series 3	1012	1024	1187	846	1037	1134
350 µm	Series 1	1073	1111	1415	1030	1127	1290
	Series 2	1046	1111	1306	1046	1176	1211
	Series 3	1304	1585				

Table 9 Measured channel widths for the reduced one-chamber design using the correction factors 200 and 350 µm for z-alignment. The positions 1-6 correspond to the printing positions indicated in Figure 24/E such that 1-3 and 4-6 form a column respectively. The channel widths far above 1000 µm were caused by internal leakage as indicated in Figure 25/A. For correction factor 350 µm the prints in position 3-6 failed such that no channel width could be measured.

	1	2	3	4	5	6
	Correction Factor 200 µm					
Series 1	981	976	959	963	967	980
	965	976	943	972	919	1000
	965	1051	949	980	894	1004
	970	1041	954	984	928	1004
	970	1051	970	988	935	1004
Series 2	921	1138	1008	900	1030	894
	921	1176	965	894	1014	911
	921	1089	959	889	986	927
	927	1068	954	883	992	916
	932	1062	986	878	981	938
Series 3	1016	1024	1220	890	1065	1163
	1012	1000	1130	833	1033	1126
	992	1020	1187	829	1033	1150
	996	1081	1260	846	1037	1130
	1028	1094	1179	915	1130	1134
	Correction Factor 350 µm					
Series 1	1019	1106	1285	1084	1279	1322
	1051	1095	1236	1046	1073	1274
	1073	1182	1604	1030	1111	1290
	1073	1111	1507	1030	1127	1339
	1133	1122	1415	1052	1192	1279
Series 2	1079	1111	1285	1117	1182	1163
	1046	1062	1285	1046	1176	1179
	1014	1111	1306	1035	1149	1211
	1024	1133	1312	1041	1127	1264
	1068	1247	1529	1052	1187	1272
Series 3	1260	1447				
	1257	1593				
	1305	1585				
	1427	1593				
	1565	1484				

The values from Table 8 which contained the channel widths obtained with the z-correction factors of 200 and 350 μm were plotted in Figure 26 and Figure 27 for visualization.

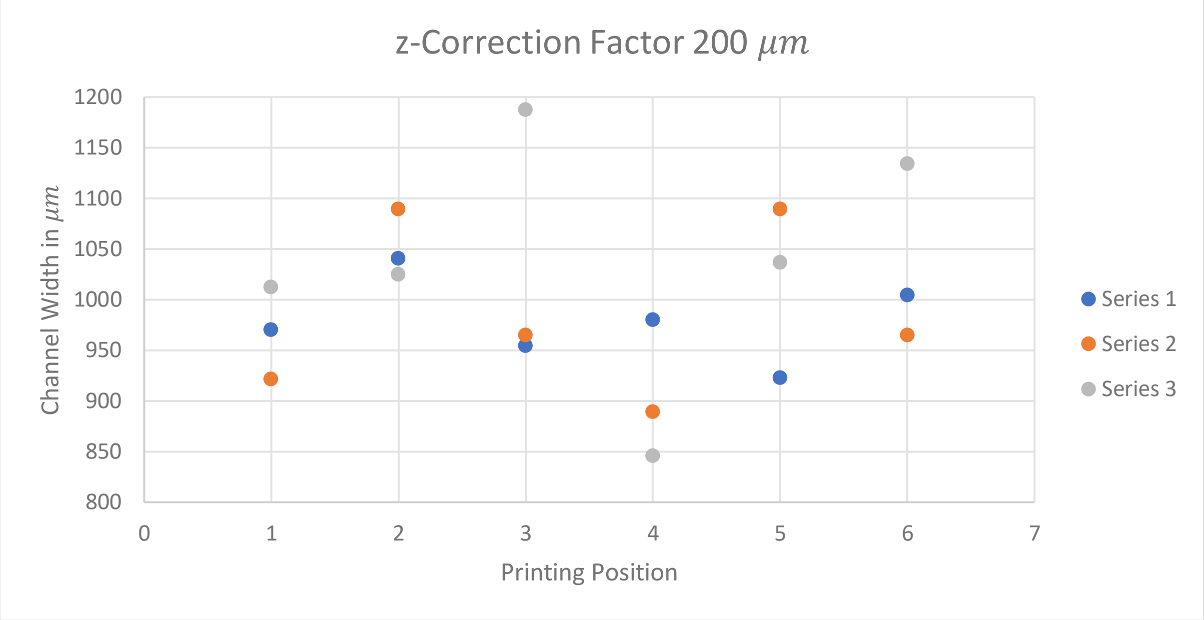

Figure 26 Plot of the results from Table 8 for the z-correction factor of 200 μm. The printing positions refer to the positions indicated in Figure 24/E such that the position 1-3 and 4-6 form a column. The trend indicates a trend of increased channel width caused by a decreased extrusion width caused by a decline in height along the y-direction with the notable exception of position 3.

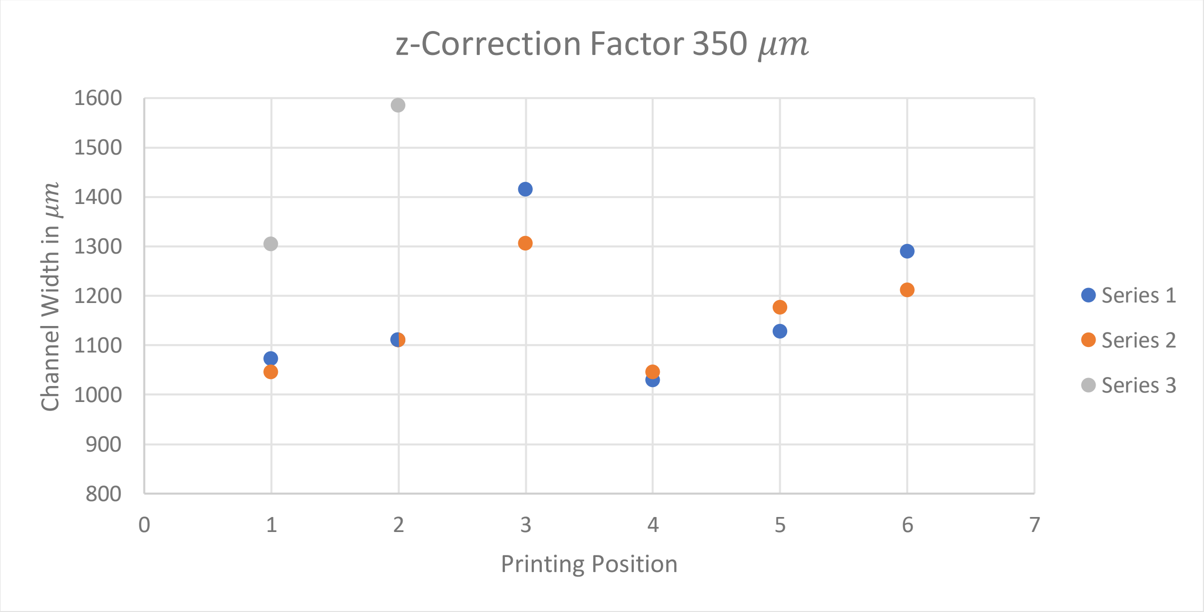

Figure 27 Plot of the results from Table 8 for the z-correction factor of 350 μm. The printing positions refer to the positions indicated in Figure 24/E such that the position 1-3 and 4-6 form a column. The trend indicates a trend of increased channel width caused by a decreased extrusion width caused by a decline in height along the y-direction. The prints of position series 3 failed after the second print and the channel widths far above 1000 μm were caused by internal leakage as shown in Figure 25/A.

Figure 28 shows extrusion width in function of first layer height obtained from printing with a RegenHU which was added to provide a reference.

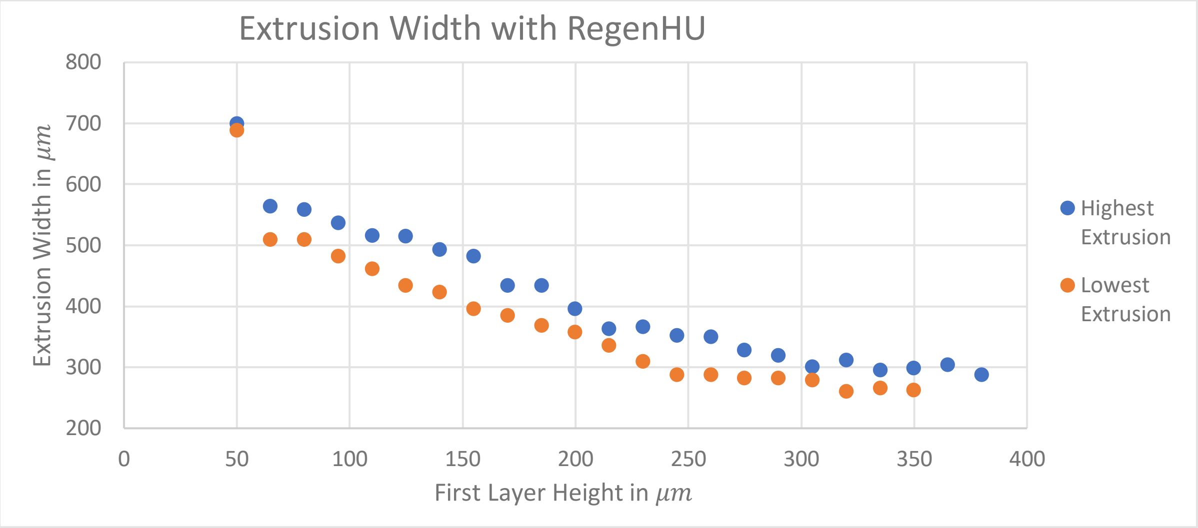

Figure 28 Plot of extrusion width for straight lines as a function of first layer height printed with a RegenHU 3D printer. The RegenHU is a state-of-the-art pressure-based 3D printer and was used as a reference to compare the results obtained with the FelixBIO to. 2 cm long PDMS lines were printed in 2 layers on microscope slides with a printing speed of 600 mm/s and a pressure of 120 kPa. The first layer height was steadily increased from 50 μm to 400 μm and the width of the lines was determined using Zeiss Axioskop 40 Polarized Light and ImageJ-MicroManager-1.4. With very high first layer heights the extruded PDMS strings became a snake-like form and were excluded from the results. The printing was repeated 5 times.

The extrusion width decreased in the reference steadily with an increase in first layer height until the extrusion became unstable around 350 μm. Accordingly, the increase in channel width along the y-direction (compare Figure 24/E) seen in Figure 27 and Figure 28 can be interpreted as an increase in first layer height in y-directed due to improper bed leveling. While there was a steady increase in channel width inside the printing columns (pos. 1-3 & 4-6) for each series when the z-correction factor of 350 μm was used, the individual series showed more apparent randomness when the z-correction factor of 200 μm was used. This might indicate that the decrease in first layer height causes increased variability of extrusion through scratching of the extruded PDMS or it might be that the reduced printing height induces mechanical vibrations in the substrate. When comparing the results gained with the z-correction factor of 350 μm with the reference from the RegenHU it might be inferred that the z-correction factor led to an effective first layer height between 300 and 400 μm due to borderline stability and higher uniformity. Using this heuristic would then mean that the z-correction factor of 200 μm enables z-alignment with a deviation of ± 50 μm, but these assumptions are rather speculative. As explained in the results section the channel widths far above 1000 μm were caused by internal leakage as can be seen in Figure 25/A. Without shrinkage the channel width would be the result of the distance between the innermost lines of the printing path minus the extrusion width. In our case this model would yield to a paradox result since the distance in the printing path was 1200 μm such that a channel width of 1000 μm or above would mean an extrusion width of less than 200 μm while the general distance between neighboring lines in the printing path was 300 μm. Although there was partial delamination as it can be seen in Figure 31 the extruded PDMS strings were at least partially in contact since there would have been complete delamination otherwise and no junctions or lumens would have been formed. Since the carbon black dyed slices that were preselected against narrowing at the channel bottom showed a mean channel width of 901 $\pm$ 23 μm this may indicate that the direct determination of the channel width as shown in Figure 27 and Figure 28 was prone to overestimation of the channel width. It should be considered that the channels might be widened due to hydrostatic pressure.

3.1.6. Cross-sectional slices for the Measurement of Channel Width, Depth and of Channel Slices

The channel depth can not only be assumed to be an important factor for axonal guidance due it's influence on medium diffusion, but it can also be used to evaluate the reproducibility of the printing process especially in regard to z-alignment. Since the channel depth is not directly measurable from the outside the devices were sliced in order to make the cross-section available for imaging. The cross-section of the STL file for the prints before they were sliced is shown in Figure 30. Because only thin slices can be properly illuminated by the microscope, but thin PDMS slices were not form stables the channels had to filled with a form stable colored material before slicing. To this aim the channels of already cured 3D printed devices were filled with carbon black dyed SE1700 PDSM using a syringe which was then cured again before slicing. Due to the relatively high viscosity of the material and the high resistance against flow in the thin channels the filling of the channels often resulted in a bursting of the channel/lid interface (Figure 29 and Figure 31). The measurement of the channel depth is shown in Table 10. A visible influence of the lid thickness on the channel depth is not recognizable and the high in-group variation may indicate that insufficient bed leveling, and improper alignment may have overshadowed its influence. The slices were further used for qualitative analysis of the printing process. As it can be seen in Figure 29/A most of the slices showed significant narrowing at the bottom of the channels presumably due to low first layer height. Figure 29/B may also indicate a widening of the channel due to the pressure with which carbon black PDMS was injected into the channels. In order to get a heuristic for the reproducibility that might be achievable with better z-alignment and bed levelling PDMS slices were selected that did only show minor channel narrowing at their bottom side as seen in Figure 31. What is recognizable on the slices is partly delamination of the PDMS along the lines of extrusion. The delamination did not affect the bottom side of the devices and seemingly not their functionality. The reason why the bottom side was not affected might be related to squeezing due to lower effective layer height, higher static pressure, or the closer distance to the rigid substrate. Although this delamination was not recognizable on the images directly taken from the devices they could be seen by eye on their top side. The delamination was partially prevented by the formation of junction which led to the formation of major lumens in some locations (Figure 29 and Figure 31). The ununiform distribution and shape of the lumens and junction may indicate that they are the results of directional contractive forces during the curing process. The channel width of these slices was measured at 5 locations in each slice and are given in Table 11. The medians of these values are given in Table 12. The mean of the median values was 901 μm with a standard deviation of 23 μm.

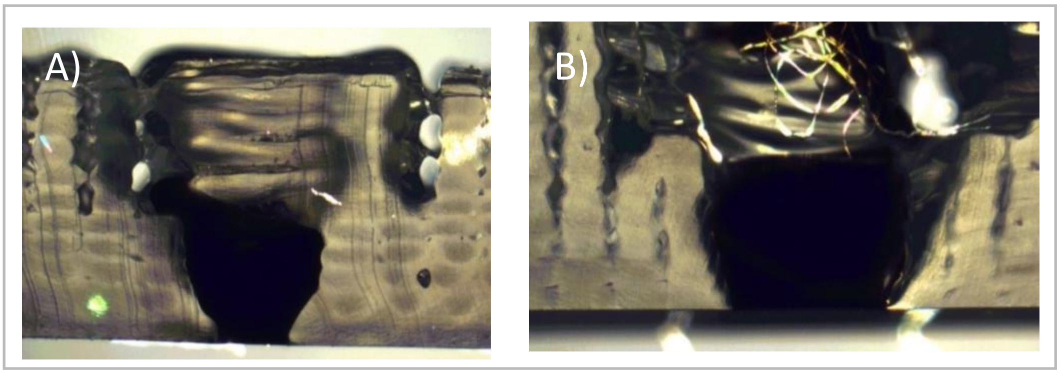

Figure 29 Examples of the channel slices used for measurement of channel depth. The measured channel depths are given in Table 10.

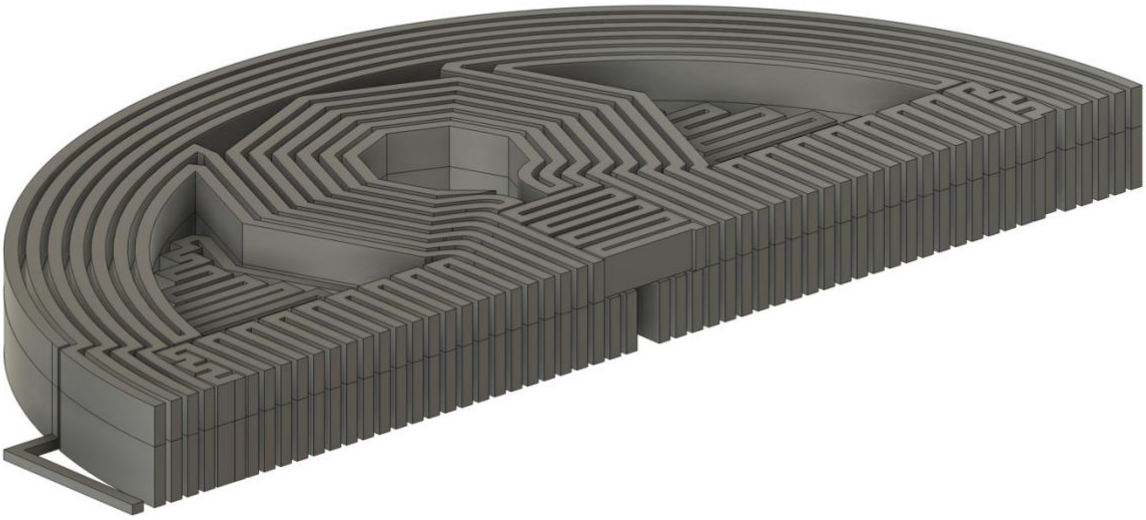

Figure 30 Cross-section of the reduce one-chamber guidance devices. The design of the full one-chamber device is shown in section 3.1.4. The (central) channel of the guidance devices were filled with carbon black dyed SE1700 PDSM after their curing and then cured again to get dyed channels. A scalpel was then used to make slices of the device cross-section which were imaged with a microscope to measure the channel depth and width. The devices were printed with different thicknesses of the lid layer which were 300, 900 and 1800 µm to investigate the influence of lid thickness on the channel depth. These thicknesses correspond to 100, 300 and 600 % of the thickness of the one-chamber devices used for organoid culture.

Table 10 Channel width as a function of lid thickness. 100% correspond to 300 µm, 300% to 900 µm and 600% to 1800 µm.

	Sample Number			
Lid Thickness	1	2	3	4
100%	1014	667	607	748
	921	656	607	618
	1014	613	645	640
300%	748	824	743	688
	753	710	688	753
	764	705	662	694
600%	840	678	499	732
	846	667	509	797
	824	667	537	694

As it was discussed on the last page the values in Table 11 come from cross-sectional slices which were specifically for a lack of channel narrowing at the bottom. Since this widening was assumed to be the result of misalignment on the z-axis and thus this represents an attempt to have a heuristic of the reproducibility that might be possible with proper z-alignment. The channel width of these slices was measured at 5 positions from one side to the other and their values are given in Table 11 and the median of these values is given in Table 12. The slices themselves are shown in Figure 31.

Table 11 Channel width of the slices which were selected for absence of channel narrowing at the bottom. The selection was done in order to get a heuristic for the reproducibility that could be achievable with better z-alignment and bed levelling. Each slice was measured at 5 locations from one side to another.

	Sample Number					
	1	2	3	4	5	6
Channel Width in μm	791	783	746	787	830	752
	859	908	879	883	907	889
	932	942	896	912	932	881
	936	913	900	883	945	836
	923	908	867	892	949	888

Table 12 Median channel width of slices which showed a uniform channel width. The median widths were taken from the values in Table 11. The mean of the median values was 901 μm with a standard deviation of 23 μm.

Sample	1	2	3	4	5	6
Channel Width in μm	923	908	879	883	932	881

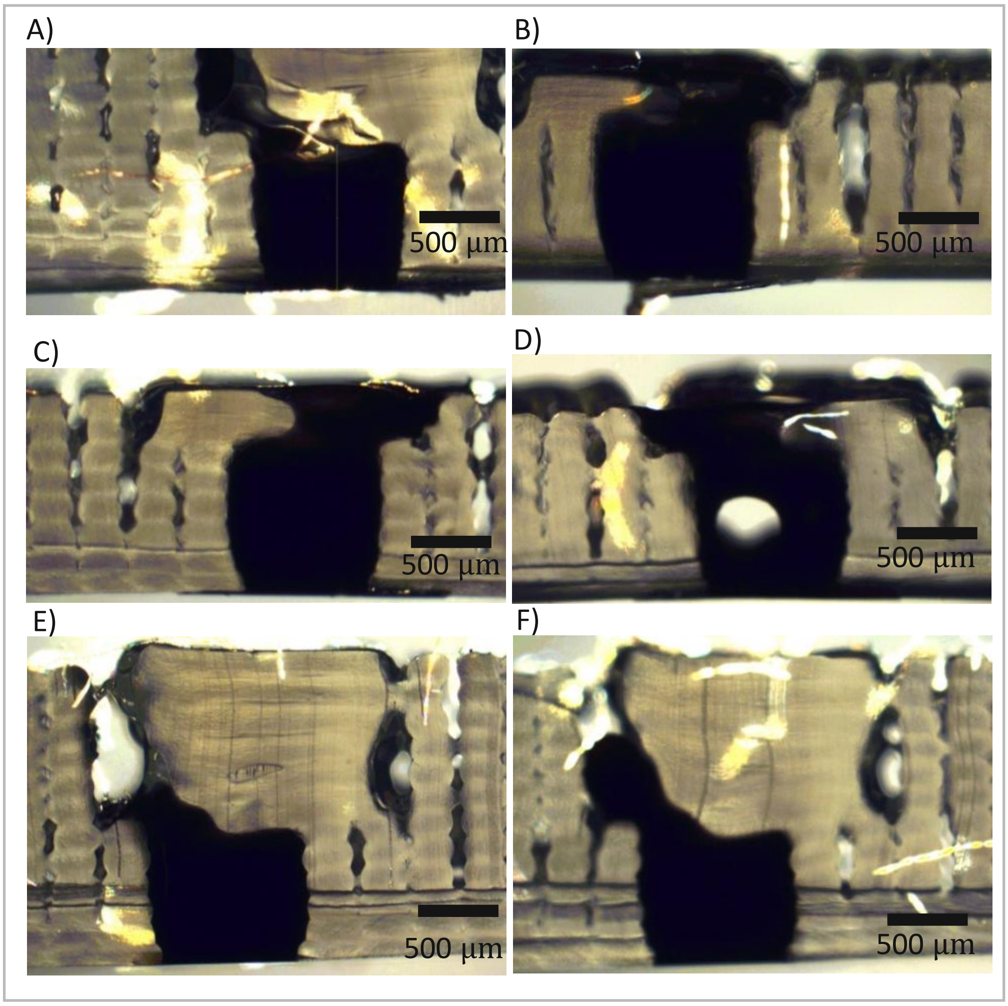

Figure 31 Microscope images from the device slices which were selected for weak channel narrowing at the bottom. The slices show signs of delamination but not on the bottom of the device. This might be the result of higher static pressure, squeezing due to a lower effective printing height or closer distance to the rigid substrate. The delamination was largely prevented by junctions that seem to have formed during PDMS curing (good visible in E). Related to the formation of these junctions is the presence of major lumens in some locations. The delamination was recognizable by eye on the top of the prints but did not seem to interfere with the functionality of the devices. The top of the channels was presumably opened during the injection of carbon black PDMS since they were resistant to leakage when tested with dyed water. The cross-section of the STL file used for slicing is shown in Figure 30. A more thoroughly discussion on the prints is given in 4.2

3.1.7. Upside-Down Printing

Since it was observed during preliminary experiments that the extrusion in the first printing layers can be subject to major variations that do not affect upper printing layers to the same extend upside-down printing was investigated to circumvent these problems. The idea was to print the desired structure on a primary substrate with the channel facing upwards and then place the print on a secondary substrate while still uncured (Figure 32). After curing the primary substrate would be removed such that the wells and channel would be accessible for cell culture. The primary substrates were 24x50 mm cover slips from VWR and the secondary substrates were Hounisen 76 x 26 mm object glasses. Since the PDMS was not detachable from the primary substrates they were cut off using a scalpel. A preferred approach would have been the use of either passivated primary substrates (e.g. silanized with fluorosilanes) or water-soluble primary substrates but these were not used due to their unavailability. The passivation of the primary wafer is discussed in section 2.2.2. A CAD file (Figure 33) was created for this printing approach that had a channel width of 450 μm a well diameter of 2000 μm. The design consisted of two design layers were the closed layer (printed at the bottom) had a height of 1800 μm and the channel layer a height of 450 μm. The experiment was performed in triplicates and the channel width was measured analogue to the previously described experiments. The measured values are given in Table 13 and the microscope images are shown in Figure 34. For microscope imaging isopropanol was mixed with water and baker's color to overcome the hydrophobicity of the PDMS channels which led to the pigments.

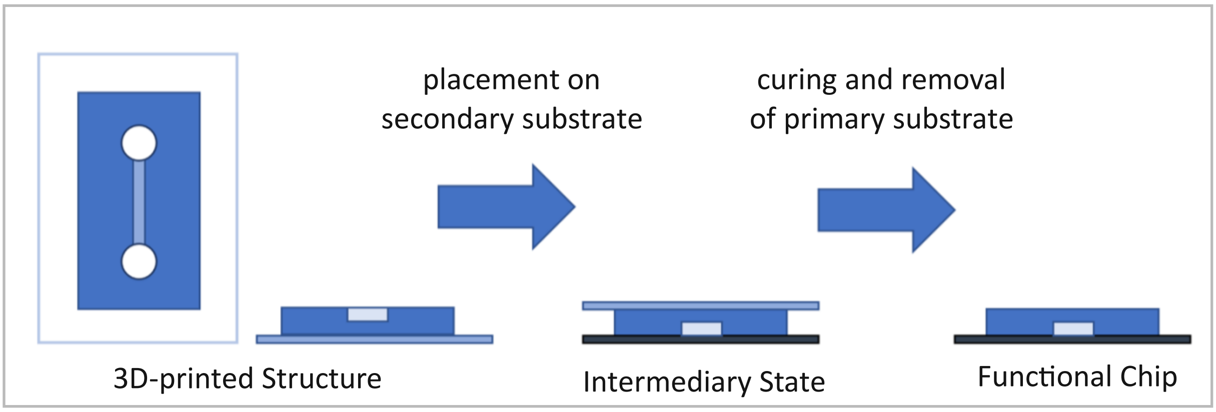

Figure 32 Concept of the upside-down printing approach. The desired structure is printed upside-down on a primary structure and is then placed on a secondary substrate before curing. After curing the primary substrate is removed and the channels and wells are accessible for cell culture.

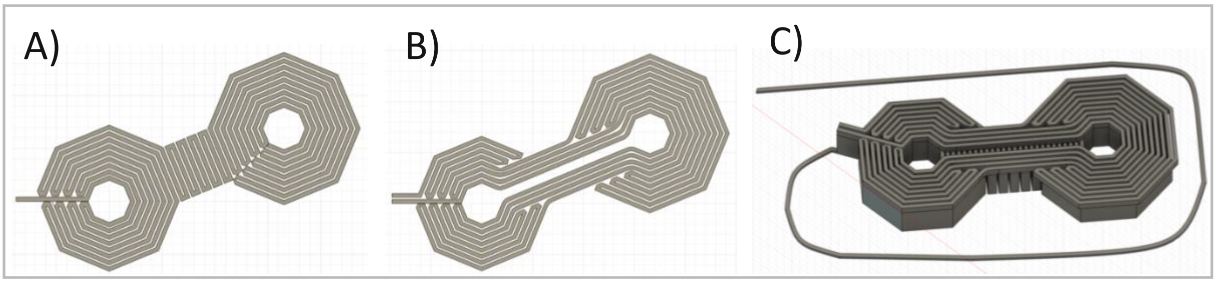

Figure 33 CAD file for upside-down printing. The design had a channel width of 450 μm and a well diameter of 2000 μm. The two design layers were a closed layer with a height of 1800 μm (A) and a lid layer (B) with a height of 450 μm. The assembled design had a short starting path (C).

Table 13 Channel width obtained by upside-down printing. The experiment was done with triplicates and the channel width of each print was measured at 3 points.

	Sample Number		
	1	2	3
Channel Width in µm	363	363	320
	379	358	353
	352	347	358

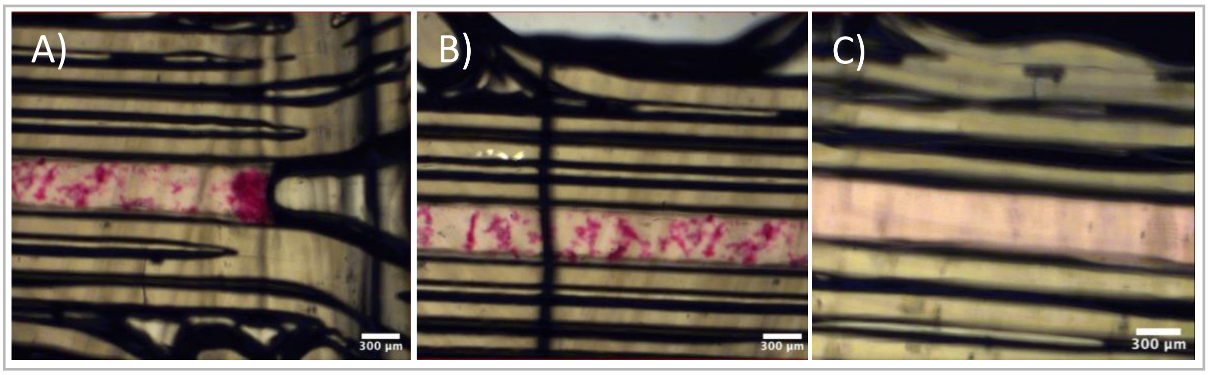

Figure 34 Microscope images from the upside-down printing experiments after removal of the primary substrates. Due to the hydrophobic resistance isopropanol was mixed with water and baker's color to dye the channel which led to the pigments visible in A & B. The image in C was taken after the isopropanol/water mixture was removed from the channels using a pipette and replaced with water which mixed with the residual fluid and pigments.

3.2 Cell cultures

As this thesis can be seen as a preliminary work for the OpenMIND project the goal was to fabricate 3D printed guidance devices that would allow for the spatially separated cultivation of two organoids connected via axon fascicles that resemble the nigrostriatal path (see section 1.1). A prerequisite for this is the biocompatibility of the 3D printed device which is a function of the used material and its handling. In this case this does not only mean that cells need to be able to survive in close proximity to the printed structures but also that they must not influence the stem cells negatively during their development into mature brain organoids. Although PDMS is regarded as one of the most biocompatible materials particularities of the used product like the functional groups for cross-linking might cause problems with the cells and thus render the printed devices useless. In this regard it should be regarded that cell death in culture is often the consequence of bacterial, east or fungal infection, mishandling of the cells or the contamination of the products used for cultivation. Another criterium is that the fabricated devices should allow for proper handling of the organoids and guide their developments towards axonal channel penetration and axon fascicle formation (see section 3.2.2.3). As this is largely a function of the geometry of the device failure in this regard might be correctable by a change in design, printing set-up or change of coating. Since the specialized expertise culture and adequate laboratories for brain organoids were not yet established at DTU the organoid cultures were conducted in the author's 3D printed devices by the project partners from Lund University. Since brain organoids require long times to major which is both expensive and requires large time commitment spheroid cultures were tested in 3D printed devices. This would allow to get a first evaluation of the suitability of the devices in respect to material properties and structural features. In addition, different conditions for hVM1 spheroid formation and culture were tested since suitable protocols might allow for fast-growing simplified models of the nigrostriatal pathway that might be used in the prototyping analytical devices.

3.2.1. Testing of the Two-Chamber Devices with Spheroids

The two-chamber device was the first majored prototype and was used with hVM1 spheroids in order to make a first evaluation of the printed devices in respect to the biocompatibility of the material and the suitability of the structural dimensions to induce channel penetration and subsequent bundling into fascicle (see 3.2.2.3) for mimicry of nigrostriatal path (see 1.1). The printed prototype is shown in Figure 35 and the considerations behind the design are given in section 3.1.4. During the printing of these devices mechanical alignment was used were the movability of sheet of paper between nozzle and printing bed was used to estimate the distance. This was done because the more elaborate methods for z-alignment (see section 3.1.3) were not yet established when this batch of prototypes was printed. After mechanical alignment to the supposed zero position the nozzle was elevated for 600 µm before placement of the substrate and start of the print. Since there were visibly major variations in the channel width the devices were manually selected by eyesight and the microscope images taken during spheroid cultures were used to measure the channel widths which were measured to be between 65 and 95 µm using image analysis with ImageJ-MicroManager-1.4. This was done because microscope imaging before culture might have introduced the risk of toxic contamination and because the channel dimension might chance when the channel is flooded with aqueous medium. For the spheroids generation 50.000 hVM1 cells were suspended in 200 µL proliferation medium consisting of DMEM/F12 (1:1) with Glutamax as a solvent, AlbuMAX-I (1.25 g/L), HEPES (5mM), glucose (6g/L), penicillin/streptomycin (0.1 v/v), N_2

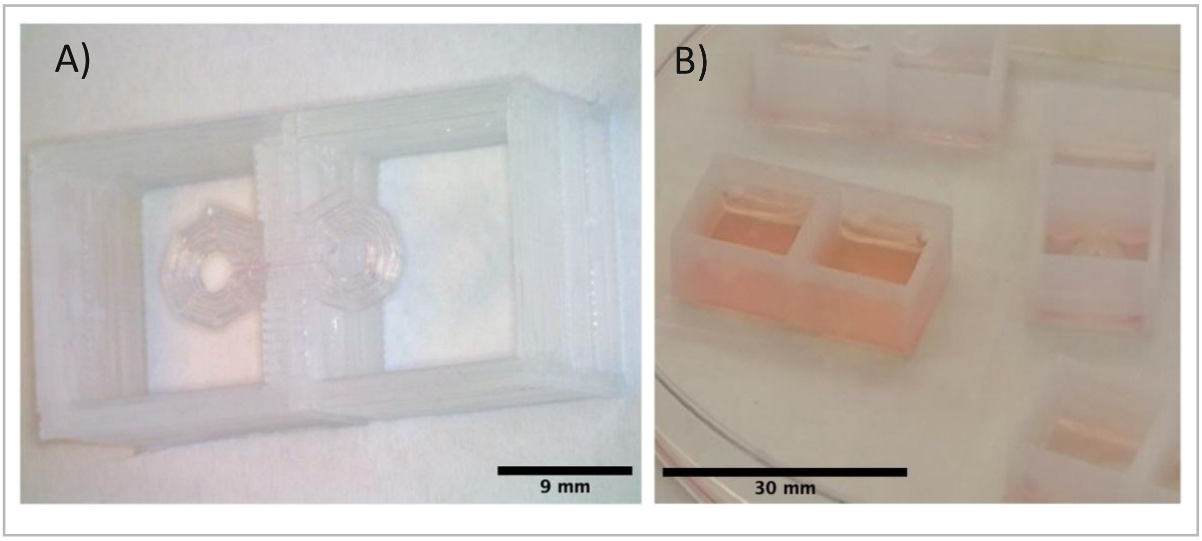

Figure 35 Images of the two-chamber PDMS guidance devices. Image A was taken with a dinocam from the bottom and the channel is visible at close inspection. Image B was taken with a phone camera and shows the hVM1 spheroid culture where leakage from several devices is recognizable through the low levels of culture medium. The bottom of the printed device was accessible due to the printing on passivated wafers (see ***Error! Reference source not found.****).*

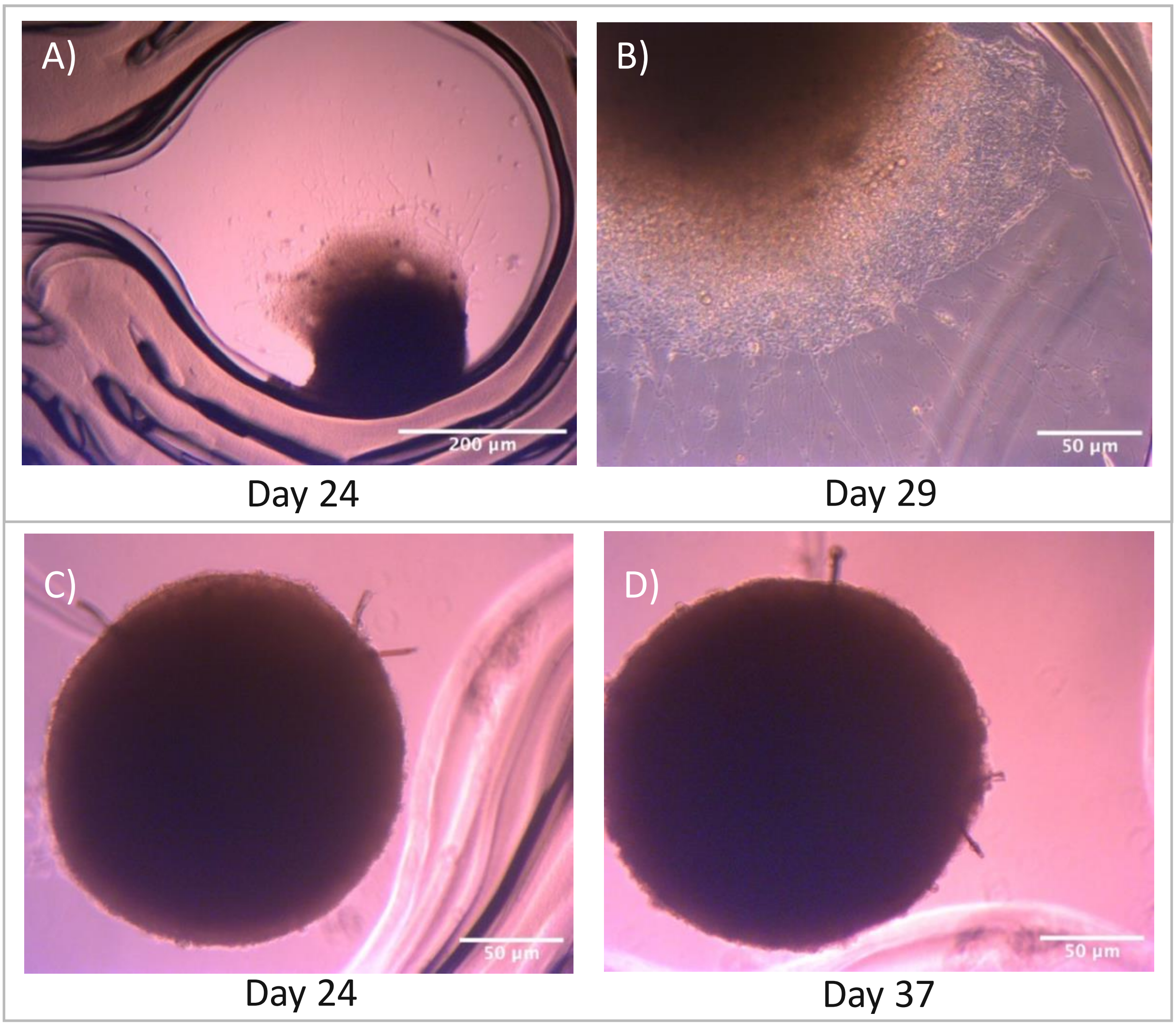

Figure 36 Two spheroid cultures (A,B & C,D) in the two-chamber guidance device. The days 24, 29 & 37 correspond to day 14, 19 & 27 in the guidance device respectively. The spheroid shown in A & B had a relative strong outwards projection of axons but presumably due to the distance it did not penetrate the channel. The spheroid shown in C & D appears to have had neither outwards projection of axons nor cellular outgrowth putting the viability of its constituting cells into question.

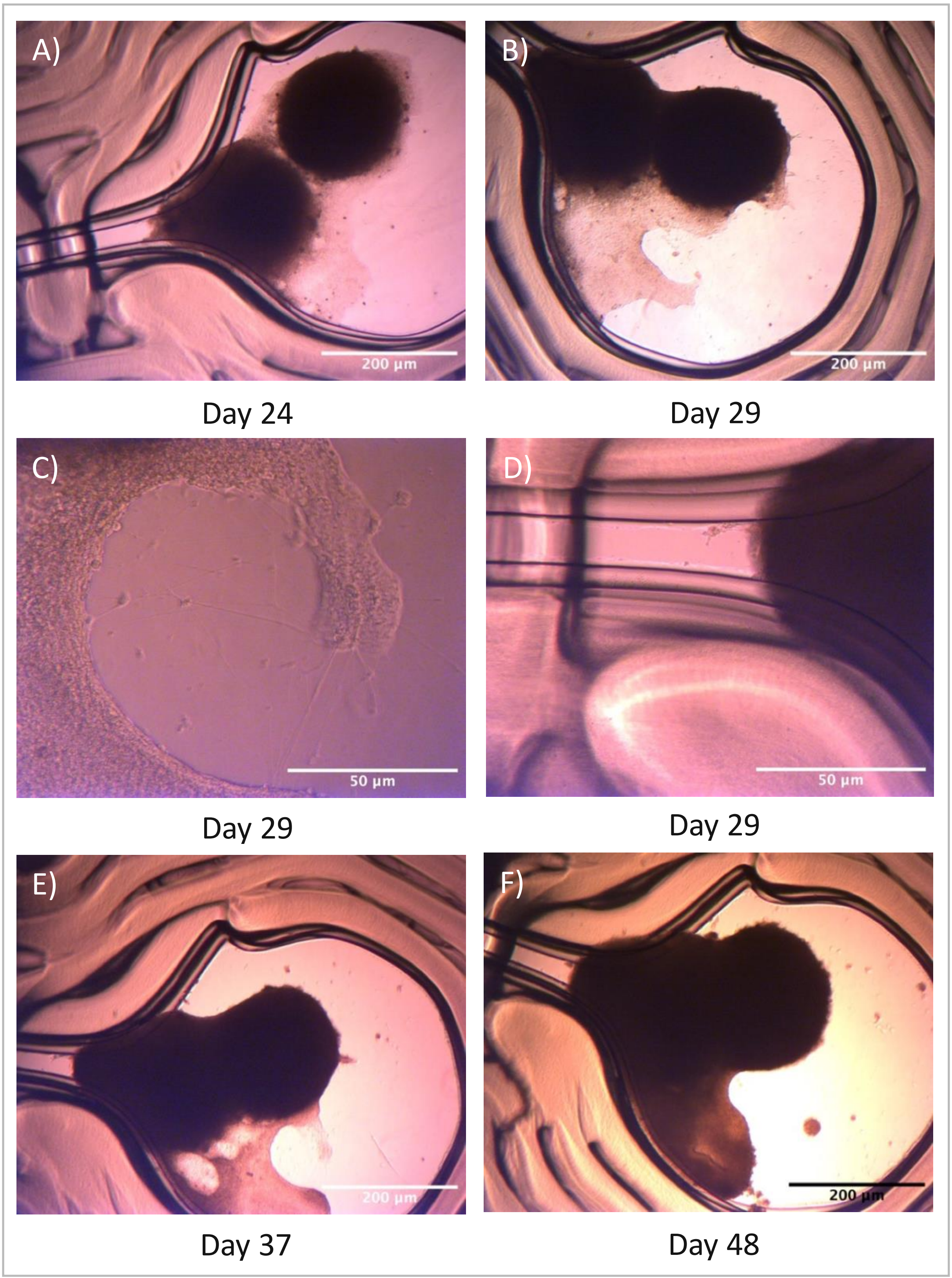

Day 24

Day 29

Day 29

Day 29

Day 37

Day 48

Figure 37 Spheroid culture in the two-chamber guidance device. During transfer two spheroid settled in a single chamber. The days 24, 29, 37 & 48 correspond to day 14, 19, 27 & 38 in the guidance device respectively. It can be seen that cells partially colonized the bottom of the well as a thin film on day 24 (A) that became progressively thicker until day 48 (F) as indicated by the decreased light transmission. Further it can be seen that the two spheroids had seemingly fused on day 29 (B). Image C shows limited axonal outgrowth close to the middle of the well while image D indicates that there was to axonal penetration of the channel. Comparing the lower halves of image E & F it appears as if the cell culture slightly decreased in area due to shrinkage.

3.2.2 Spheroid culture in Coated Well Plates

3.2.2.1 Experimental Outlook

Since the cell culture in the two-chamber devices gave unsatisfactory results and no protocols for hVM1 spheroid formation are available, it was decided to investigate different conditions for spheroid generation and substrate coating for hVM1 culture. Two methods were used to generate hVM1 spheroids which will be referred to as proliferation medium seeding and differentiation medium seeding. The difference between the two methods was whether the cells were resuspended in proliferation medium or differentiation medium after splitting, before they were seeding into faCellitate ultra-low attachment 96-well plates. The proliferation medium seeding is more similar to standard approaches for spheroid formation, but it can be expected that some proliferation medium will retain in the interior of the newly formed spheroids which might interfere with the chemical signaling after medium exchange or might lead to increased cell death at the interior of the spheroids due to higher metabolic activities. To give more details in the proliferation medium seeding method cells were suspended in 200 ml proliferation medium and seeded into faCellitate ultra-low attachment 96-well plates (day 0) using a 200 µL Eppendorf mechanical pipette. The hVM1 cells were kept in 2D culture for more than 2 weeks before the start of the experiments. The proliferation medium was based on DMEM/F12 (1:1) with Glutamax as a solvent and contained AlbuMAX-I (1.25 g/L), HEPES (5mM), glucose (6g/L), penicillin/streptomycin (0.1 v/v), N_2 supplements (0.1 v/v), non-essential amino acids, hrEGF (20 mg/L) and hrFGF-2 (20 mg/L). Details on the manufacturers, handling and the non-essential amino acid solution are given in the section “Materials”. The next morning 175 µL medium were removed and replaced with differentiation medium (day 1) using an Eppendorf Xplorer Plus electronic eight-channel pipette. Differentiation medium contained GDNF (2 mg/L) and dibutyryl cAMP (2.5 g/L) instead of hrEGF and hrFGF-2 but was otherwise identical to proliferation medium. More information about the medium is given in the appendix. In the proliferation medium seeding method, the cells were suspended in 200 µL differentiation medium and then seeded into faCellitate ultra-low attachment 96-well plates (day1). Every second day 90 µL medium were removed from each well and 100 µL differentiation medium were added using an Eppendorf Xplorer Plus electronic eight-channel pipette. The 10 µL surplus was added in order to account for evaporation. The cells were kept in the ultra-low attachment plates between 3 and 15 days in differentiation medium and were then transferred into coated 96-well plates using a single-channel mechanical Eppendorf pipette. The medium was retained during transfer and the rhythm of medium exchange was kept. For both methods three spheroid sizes were generated starting with 25.000, 50.000 and 75.000 cells respectively. Different cell numbers were chosen because bigger spheroids can be assumed to grow thicker axonal fascicles due to their increased size, but an increased spheroid size may lead to a necrotic core. In addition, cell density and spheroid size may trigger different cell signaling pathways due to different mechanical cues, oxygen gradients or other factors. The 96-well plates were coated with poly-L-lysine (0.1% w/v) for transfer days 4 to 10 and Geltrex for transfer days 4 to 16. The difference in used transfer days was due to an insufficient cell number before splitting. PLL is mostly used for proliferation of stem cells due to its lack of trophic factors and ECM proteins, but its successful application in hVM1 dopaminergic differentiation has been reported[68]. In addition, patterns of different PLL densities have been shown to guide neuritogenesis and redirect axonal growth along their lines through interaction with the filopodium[69, 70]. Geltrex is a basal membrane extract that resembles physiological conditions *in vivo*[71] and contains proteins that are known to be associated with growth cones[72] and support of dopaminergic differentiation[73, 74]. The different transfer timepoints from the low-adhesion plates to the coated well-plates were tested because the differences in the microenvironment the cells are exposed to can be assumed to provide different cues for cellular development and lineage commitment and thus influence spheroid maturation. The different conditions used for Spheroid formation are summarized in Table 14. The spheroids with transfer days 4 & 7 were cultured until day 19 when they were fixated and then immunocytochemistry was performed. Live/dead staining was performed for the spheroids with transfer days 10 to 16 on day 26 and after imaging they were fixated and then immunocytochemistry was performed. During culture the development of the spheroids was monitored using brightfield microscopy and at the end of the culture live/dead staining and immunocytochemistry were performed to assess the samples.

Table 14: Summary of the conditions for spheroid formation

	Conditions		
Medium for Seeding	Proliferation Medium	Differentiation Medium	
Substrate Coating	Geltrex	Poly-L-Lysine	
Cells per Spheroid	25.000	50.000	75.000

3.2.2.2. Imaging, Fixation and Staining

Since no protocols for hVM1 spheroid fixation were available established protocols for 2D cultures were adapted for the longer times necessary for mass transport into the interior of spheroids. Unfortunately, this approach led to damage to the protruding axons for the spheroids transferred on day 4 & 7 the duration of each step was reduced again to the original times of the 2D protocols for the spheroids with later transfer days. For fixation the first group was kept for 30 min in 4% (v/v) paraformaldehyde in PBS and washed twice with PBS for 5 min. The second group was kept for 2 minutes in 2% (v/v) PFA in PBS and for 4 min in 4% PBS for fixation and washed twice with PBS for 5 min. For permeabilization/blocking and immunocytochemistry the times for the later transferred spheroids will be given in brackets. For permeabilization & blocking the spheroids were kept for 6 h (or 1 h for the second group) in STPBS solution. For the formation of the STPBS solution Triton X-100 was dissolved in PBS under stirring for a final concentration of 0.3 % (v/v) before goat serum and horse serum were added to a concentration of 1 % (v/v) each. Afterwards the spheroids were incubated with rabbit polyclonal anti-tyrosine hydroxylase and mouse monoclonal anti-β-tubulin III primary antibodies diluted together 1:1000 in STPBS for 48 hours (O/N) at 4°C. Afterwards the antibody-solution was removed and the samples were washed with STPBS for 30 min (10 min), then with 0.3 % Triton X-100 in PBS for 30 min (10 min) and then with PBS for 30 min (10 min). After this the samples were incubated with Alexa 546 goat anti-mouse (1:500) and Alexa 647 goat anti-rabbbit (1:500) together with Hoechst 33342 solution (1:5000) in PBS for 24 h at 4°C (30 min). The secondary antibody solution was then removed, and the sample washed twice with PBS for 30 min (10 min). For live/dead staining the samples were washed 3x with PBS in preparation and then incubated for 20 min in 0.5 ‰ (v/v) Invitrogen™ calcein AM & 2 ‰ (v/v) Invitrogen™ ethidium homodimer-1 in PBS for 20 min in the incubator at 37°C. Imaging for both live/dead staining and immunostaining was performed using Zeiss AxioObserver Z1 inverted epifluorescence microscope equipped with 5x (EC Plan-Neofluar 0.16 M27), 10x (EC Plan-Neofluar 10x/0.30 Ph1, Zeiss™, Germany) and 20x magnification (LD Plan-Neonfluar 20x/0.4 Korr M27, Zeiss™, Germany) objectives. Images were then processed using Zen (Zeiss™) and Fiji NIH image analysis software.

3.2.2.3 Discussion of Summarized Results

In order to increase the ease of reading the results of these experiments they will first be summarized and then later be shown in detail for each condition. This way it will not only be possible to get a quick overview over the results, but this will also help the reader with understanding the context necessary in which the results for each condition have to be evaluated. Since the envisioned purpose of the hVM1 spheroids was to be a fast-majoring substitute for brain organoids in connectoid systems (see section 1.3) one of the major criteria in the evaluation of the experiments will be the extent to which the spheroids display axonal protrusion. Figure 38 illustrates the process of axonal protrusion followed by axonal penetration of a microchannel and formation of axon fascicles. While the axon cannot be recognized readily during spheroid formation in low-adhesion plates the axons will protrude[81] and form networks on a coated substrate under the right conditions. Given the right dimensions of the culture devices axonal pathfinding may lead to redirection of the protruding axons into the microchannels and subsequent bundling into axon fascicles[82].

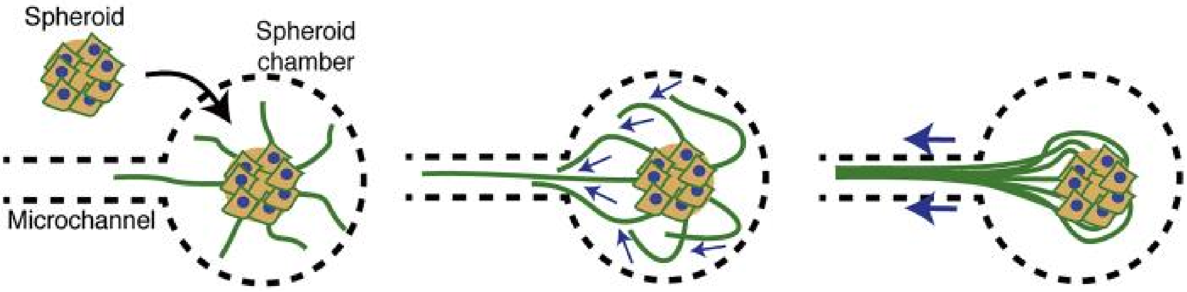

Figure 38 Illustration of axon protrusion (left), channel penetration (middle) and axon fascicle formation (right) of spheroids seeded in a microfluidic guidance device[82].

Since the extend of axon protrusion and the size and density of the resulting axonal network can be regarded as a sufficient proxy for the extent to which these conditions would lead to channel penetration and axon formation in a microfluidic guidance device, they were used to evaluate the success of a growth condition. Besides the fact that testing each condition with 3D printed guidance devices would have been unfeasible due to the high demand in medium and laboratory space the differences in the effective well size and channel dimensions may have obscured the effects of the different conditions for spheroid formation. The biggest influence on the protrusion of axons had whether proliferation medium or differentiation medium was used for seeding. With all other conditions the spheroids showed more axonal protrusion and larger axon networks when differentiation medium was used for seeding. This was especially true for small spheroids where clear signs of cell viability were mostly absent when proliferation medium was used for seeding, which is distinct to other conditions were clear signs of cell viability were usually recognizable. This group of spheroids could not be imaged with live/dead staining because all sample were unintentionally removed during washing which can be attributed to low cell viability since the moment of spheroid transfer and therefore little formation of adhesion sites. Removal of spheroids and axons during washing and fixation was a problem with several samples which is further discussed in the conclusions section 4. Besides axonal protrusion as a clear sign of cell viability other indicators were cellular outgrowths, spheroid flattening, adhesion to the substrate and cellular rearrangements that changed the spheroid shape. An illustration of the extend of axonal protrusion and sign of cell viability that resulted from the different conditions on PLL is shown in Figure 39.

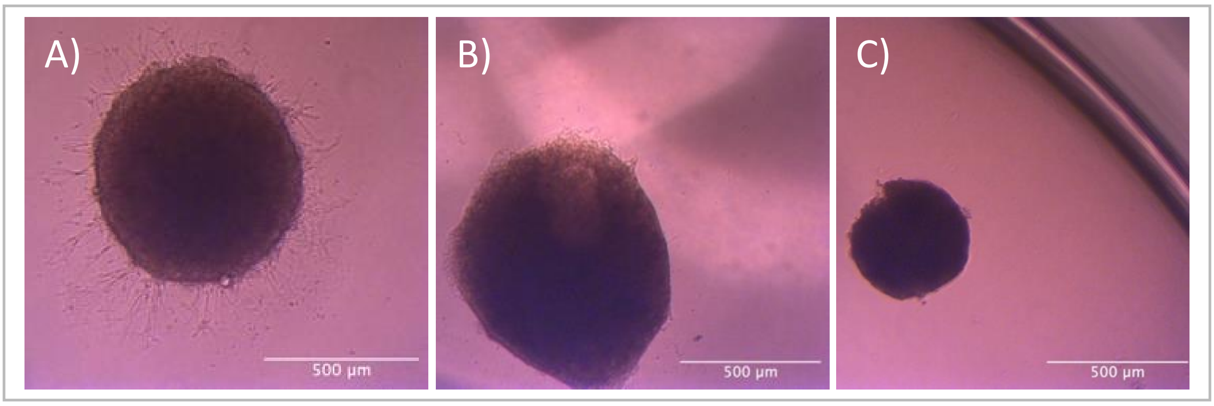

Figure 39 Representative outcomes for different conditions for spheroid formation after culture on PLL coated well-plates. The biggest influence on axon protrusion and subsequent formation of axonal networks was whether the differentiation medium (A) or proliferation medium (B & C) was used for cell suspension during seeding. The use of proliferation medium appeared to be especially detrimental in combination with a low cell number (25.000) like shown in C.

All three of the shown spheroids shown in Figure 39 were cultivated in PLL coated well-plates onto which they were transferred on the fourth day of culture (left & middle) or on the tenth day (right). While differentiation medium was used for the formation of the spheroid on the left proliferation medium was used for the other two. The Spheroid A in Figure 40/A shows strong axonal protrusion leading to a dense network of neurons around the spheroid. The stark contrast to the other two spheroids is representative of the influence of the medium during seeding. While the spheroid B shows some signs of cellular outgrowth or flattening on the top and on the left these observations are absent on spheroid C. The difference in morphology can be better understand if compared to spheroid A where a difference in cell density is recognizable on the edges via the increased light transmission. The additional deterioration seen in spheroid C to B is assumed to come from the low cell number that had an additional detrimental effect in combination with proliferation medium during seeding. The cell viability for samples with the conditions of C could not be determined by live/dead staining since these spheroids were washed away during washing. The biggest factor that influenced the results besides the medium used for seeding was whether the well-plates were coated with PLL or Geltrex. While the spheroids on PLL only showed partial flattening (Figure 39) the spheroids flattened thoroughly on Geltrex like shown in Figure 40. Presumably related to this the spheroids on PLL formed dense networks in the proximity of the spheroids, while the flattened spheroids on Geltrex formed only loose networks but with a far higher reach.

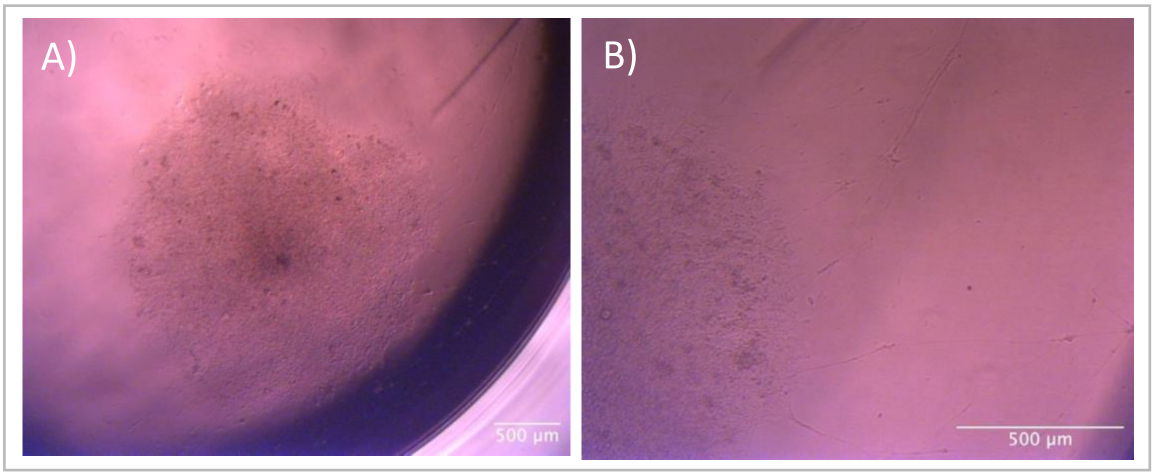

Figure 40 A spheroid formed with differentiation medium during seeding after culture on a Geltrex coated well-plate. The spheroid is shown in increased magnification on the right to show the protruding axons.

A possible explanation for the fact that the spheroids on PLL retained their sheroidal shape and that the axonal networks did not project further outwards and instead aligned themselves concentrically to the spheroids might be that PLL does not provide physiological ECM proteins for integrin interaction which might have caused axonal outgrowth to be redirected towards neighboring axons and cell soma. Although PLL has been shown to be effective in guiding axonal growth[69, 70] these findings stem from 2D cultures on patterned surfaces and are therefore not expected to necessarily yield the same outcomes. The fact that the cultivation on Geltrex did not yield dense networks might be related to the flattening of the spheroids since this alters the mechanical cues the cells are exposed to. Although the length of the protruding axons seemed promising the low number their density rendered these cultures unviable as a substitute for organoid cultures. The influences of the day of transfer from the low-adhesion plates to the coated well-plates and the spheroid size are more complex to evaluate and less pronounced than the influence of seeding medium and coating. On PLL the spheroids of 50.000 and 75.000 seemed to be superior to the spheroids of 25.000 cells but the influence of the day of transfer to the coated plates is not very clear. On Geltrex larger spheroids and a later transfer day led tendentially to better outcomes, but the 25.000 cells spheroids with early transfer days showed a much higher variability in their outcomes such that some of them outperformed the bigger spheroids with later transfer. A clear trend might be visible with a larger sample number, but due to the large in-group variability in comparison to a relatively low between-group variability no valid conclusion can be made about the effects of transfer day and spheroid size on Geltrex. If the spheroid experiments in guidance devices were to be continued it can be expected that increase axon protrusion would lead to increased channel penetration and may further lead to the formation of axonal fascicles. A potential approach to yield the benefits of PLL and Geltrex might be to coat the substrate first with PLL and then try to get Geltrex proteins to sediment on the PLL coating. This way the initial conditions might lead to dense axon networks that then project further outwards after sedimentation of Geltrex proteins. The results of the experiments are summarized in Table 15 for PLL and in Table 16 for Geltrex. The spheroids were kept in the ultra-low attachment plates for 72h, 144h, 216h, 288h & 360h before they were transferred into coated 96-well plates equaling transfer timepoints τ of day 4 (τ4), day 7 (τ7), day 10 (τ10), day 13 (τ13) & day 16 (τ16). The formation of projections was assessed utilizing brightfield microscopy until day 19 for τ4 & τ7 and until day 26 for τ10, τ13 & τ16. The cultivation time for τ4, τ7, τ10, τ13 & τ16 on coated well plates were therefore 15, 12, 16, 15 & 12 days respectively. Immunostaining was performed for all transfer days but was only for τ4 and τ7 successful. Live/dead staining was performed for τ10-τ16 followed by fixation and brightfield spectroscopy to assess to damage to the projections during this process. Using the images from brightfield microscopy and live/dead staining the spheroids were classified as having no outwards projections (np, red – similar to Figure 39/C) , weak outwards projection of axons (wp, red – similar to Figure 39/B), medium outwards projection of axons (mp, yellow – between Figure 39/A and Figure 39/C) or strong outwards projection of axons (sp, green – similar to Figure 39/A) and left white and empty for wells where the spheroids were lost during or before transfer into the coated plates. The numbers a,b,c & d or e,f,g & h are used to differentiate samples with equivalent conditions.

Table 15 and Table 16 Assessment of the cultivation of hVM1 spheroids on PLL and Geltrex in respect to their outwards projection of axons. A detailed explanation of the table was given on the last page.

Spheroids on Poly-L-Lysine (PLL)

25.000 Cells Per Spheroid

Transfer Timepoint	Proliferation Medium Seeding				Differentiation Medium Seeding			
	a	b	c	d	a	b	c	d
τ4	np	np	np	np	mp	mp	mp	mp
τ7		np	np	np	mp	mp		mp
τ10	np	np	np	np	wp	mp		mp

50.000 Cells Per Spheroid

Transfer Timepoint	Proliferation Medium Seeding				Differentiation Medium Seeding			
	a	b	c	d	a	b	c	d
τ4		wp	wp	wp	sp	sp	sp	sp
τ7		wp	wp	wp	sp	sp	sp	sp
τ10		wp	wp	wp	sp	sp	mp	sp

75.000 Cells Per Spheroid

Transfer Timepoint	Proliferation Medium Seeding				Differentiation Medium Seeding			
	a	b	c	d	a	b	c	d
τ4	mp	wp	wp	wp	sp	sp	sp	sp
τ7					np	mp	sp	sp
τ10					wp	sp	sp	sp

Spheroids on Geltrex

25.000 Cells Per Spheroid

Transfer Timepoint	Proliferation Medium Seeding				Differentiation Medium Seeding			
	e	f	g	h	e	f	g	h
τ4	np	np	np	np	wp	wp	sp	sp
τ7	np	np	np	np	mp	sp	sp	sp
τ10	np	np	np	np	mp	mp	mp	mp
τ13		np		np	mp	mp	mp	sp
τ16			np	np	mp	mp	mp	sp

50.000 Cells Per Spheroid

Transfer Timepoint	Proliferation Medium Seeding				Differentiation Medium Seeding			
	e	f	g	h	e	f	g	h
τ4	np	np	np	np	sp	mp	mp	wp
τ7	wp	np			mp	mp	sp	sp
τ10	np	np	mp	mp	mp	sp	mp	mp
τ13	mp	mp	wp	wp	sp	sp	sp	sp
τ16	mp	mp	mp			sp	sp	sp

75.000 Cells Per Spheroid

Transfer Timepoint	Proliferation Medium Seeding				Differentiation Medium Seeding			
	e	f	g	h	e	f	g	h
τ4	np	np	np	np	mp	sp	sp	sp
τ7					sp	sp	mp	sp

3.2.2.4 Immunocytochemistry

Immunocytochemistry was performed in order to target cell nuclei and specific markers of cell differentiation. As a preparation the cultures were fixated but in this step spheroids were lost in the process as discussed in 3.2.2.3 and 4. β-III tubulin was used as a specific marker for neurite cytoskeleton, tyrosine hydroxylase, which has a rate limiting function in the synthesis of dopamine[83], was used as a marker specific to dopaminergic neurons, and Hoechst 33342 was used for cell nuclei visualization. Since confocal microscopy was unavailable widefield microscopy was used to image the samples. Since widefield microscopy does not allow for 3D reconstructions and since the multilayered nature of the samples complicated the photographic capture of smaller structures it cannot be assumed that all stained structures could be visualized. At lower magnifications the immuno-targets TH and β-III tubulin had decreased visibility in comparison to the stained nuclei which skewed the images. Through gamma correction it was possible to improve visibility of neuronal processes. On the multichannel images in Figure 41 and Figure 42 are free nuclei on the edge of the cell cultures visible which seem to come from cells that express neither TH nor β-III tubulin.

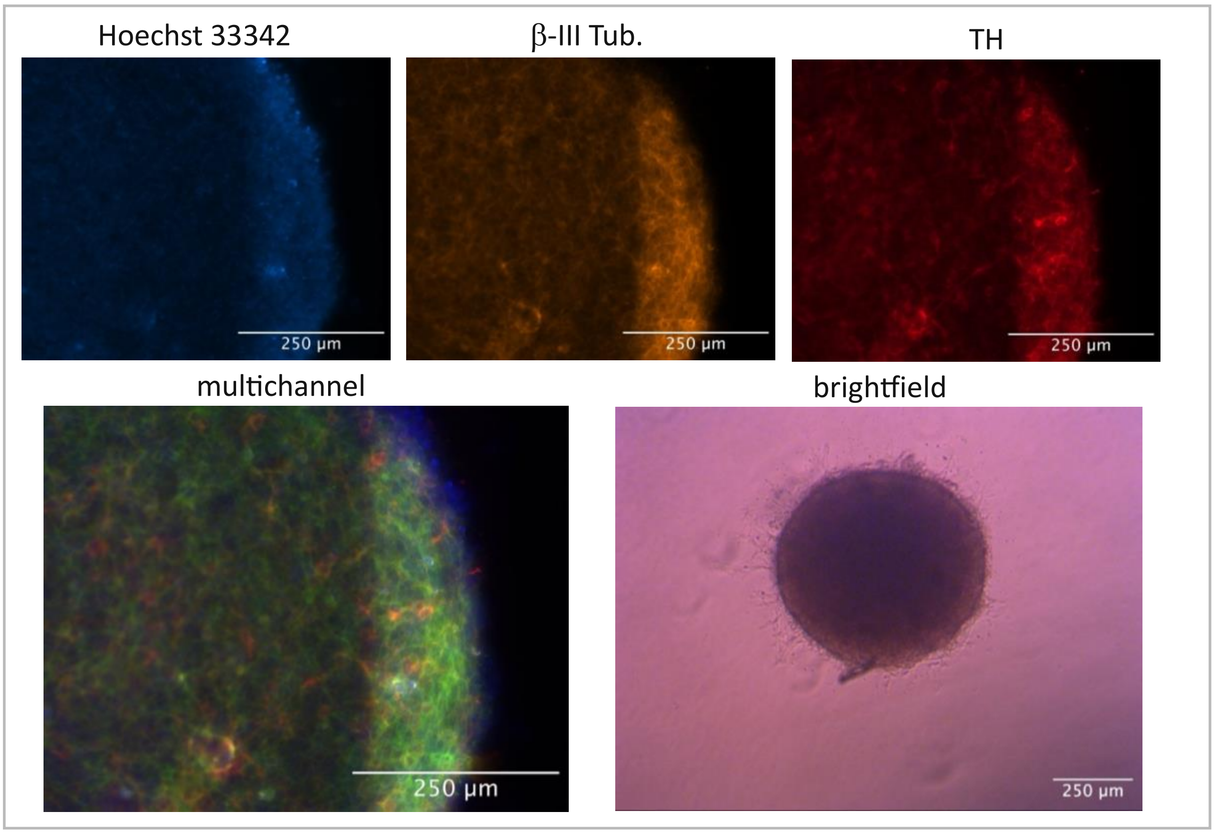

Figure 41 Immunocytochemistry and brightfield image of spheroid sample τ7/d[75.000/differentiation-medium-seeding/poly-L-lysine]. On the top are single-channel images shown for Hoechst 33342 (left), β-III tubulin (middle) and tyrosine hydroxylase (right), which mark cell nuclei, neurite cytoskeleton and dopaminergic neurons respectively. The images have been taken with widefield microscopy and are not completely monochrome due to insufficient filtering. β-III tubulin and TH are present over most of the circumference indicating that the cells largely differentiated into neurites and became dopaminergic, although the extend cannot be determined since 3D reconstruction was not possible. For the multichannel image non-blue color had been filtered for Hoechst and β-III tub. was converted into monochrome green. In the multichannel image green overshades the other colors due to a brighter color. There are some nuclei visible that are seemingly not corresponding to β-III tub. and TH signals indicating the presence of undifferentiated neuronal stem cells. Comparing the brightfield images with the fluorescence images it can be seen that the majority of axons were lost during fixation and immunostaining.

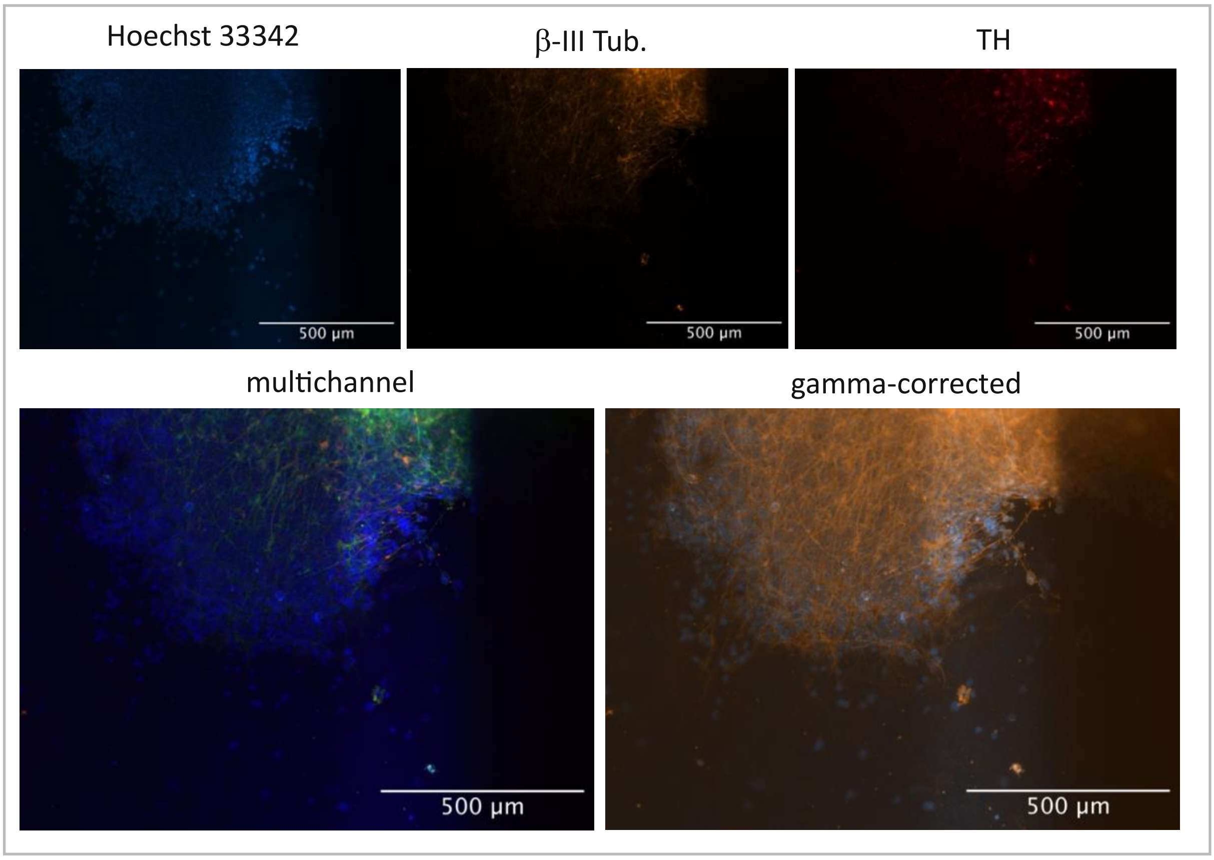

Figure 42 Immunocytochemistry of spheroid sample τ7/h[50.000/differentiation-medium-seeding/Geltrex]: on the top are single-channel images shown for Hoechst 33342 (left), β-III tubulin (middle) and tyrosine hydroxylase (right), which mark cell nuclei, neurite cytoskeleton and dopaminergic neurons respectively. The images have been taken with widefield microscopy and are not completely monochrome due to insufficient filtering. For the multichannel image (bottom left) non-blue color had been filtered for Hoechst and β-III tub. was converted into monochrome green. In the multichannel image blue overshades the other colors and green overshades red due to brighter color. The bottom right shows an overlay of Hoechst 33342 with gamma-corrected β-III tubulin. The comparison between the bottom pictures illustrates that β-III tubulin and TH were insufficiently visualized in the original image. Due to the problems with the image quality these pictures due not seem adequate to judge how many cells on the outskirt did not express the targeted markers for neurite differentiation or dopaminergic potential.

This may indicate the presence of stem cells that did not commit themselves and thus kept a larger potential for proliferation. Although the image quality was suboptimal the presence of small TH and β-III tubulin signals in their proximity in Figure 41 may be seen as valid indication of undifferentiated cells on the spheroid's edges. The gamma-corrected image in Figure 42 points in a similar direction albeit this can be assumed to be less reliable. From comparison of the fluorescence images to the brightfield images it can be concluded that the axons were largely abrased during fixation and immunostaining. Only the spheroids with transfer day 4 & 7 were TH-positive which was presumably an artefact that occurred due to problems during the second run of immunostaining.

3.2.2.5. Spheroid Size

To give additional context for the interpretation the spheroids cultivated on PLL were measured in respect to their size. Since the spheroids on Geltrex flattened no such measurement was conducted. The spheroid size was determined using the software ImageJ and the images of the spheroids formed with differentiation medium seeding on day 19. The diameter was measured in triplicates and their median values are given in Table 17.

Table 17 Diameter of spheroids formed with differentiation medium seeding on PLL on day 19 for the 3 spheroid sizes of 25.000, 50.000 and 75.000 cells per spheroid. A, b, c and d refer to the spheroids as indicated in Table 15 and the respective values are the median of triplicates. The mean values were calculated from these medians and SD stands for standard deviation.

			Spheroid Label			
Cells per Spheroid	Mean	SD	a	b	c	d
25.000	431	32	473	416	399	435
50.000	489	12	493	499	492	471
75.000	520	25	533	505	549	494

The mean values were calculated from the medians and are together with their standard deviation $431 \pm 32\ \mu\mathrm{m}$, $489 \pm 12\ \mu\mathrm{m}$ and $520 \pm 25\ \mu\mathrm{m}$. Although the small sample size means that these values are not very reliable, they indicate that there is a systematic difference in the spheroid diameter albeit a small one in comparison to their cell number.

Detailed Results for the Respective Conditions

This section serves to give more details of the experimental outcome that came from the respective conditions for spheroid culture. A discussion of the summarized results was given in section 3.2.2.3 since it was assumed that this would help the reader to interpret the results better without having to read this section again to fully grasp the differences between the conditions. The results will be shown first for Poly-L-Lysine (PLL) and then for Geltrex. For each of these two groups the conditions will be shown for proliferation medium before differentiation medium seeding and on a lower hierarchy for smaller spheroids before larger spheroids. An explanation of the tested conditions is given in 0 and 3.2.2.3.

3.2.2.6 Spheroids on Poly-L-Lysine with Proliferation Medium Seeding

25.000 cells per spheroid

With proliferation medium seeding the 25.000-cell spheroids formed no protruding neuronal processes and no clear signs of cellular growth during the cultivation period on the coated well plates were evident, regardless of transfer timepoint as can be seen in Figure 43.


τ4/a τ7/b τ10/a

Figure 43 Images from spheroid conditions [25.000cells/ proliferation-medium-seeding/poly-L-lysine]. The spheroids were kept for 3 days (left, [τ4/a]), 6 days (middle, [τ7/b]) and 9 days (right, [τ10/a]) in ultra-low attachment plates after medium exchange to differentiation medium and were then transferred into PLL coated 96-well plates. The images were taken at day 19. No formation of neuronal processes could be recognized and cell adhesion was insufficient leading to a removal of the spheroids during fixation and immunostaining.

The brightfield images suggested that several spheroids moved or rotated during culture on coated plates which indicated that formation of adhesion sites by the spheroids was at most negligible. Live/dead imaging yielded no signal with these spheroids suggesting that they were removed during washing. Two samples remained after immunostaining but showed only fractures of the spheroids. Whether this adhesion was caused by formation of adhesion sites or is the result of non-biological reactions during the fixation process is speculative.

50.000 cells per spheroid

With proliferation medium seeding the spheroids of 50.000 cells had a comparable morphology to each other independent of transfer day and slight flattening could be observed as indicated by the time series in Figure 44.

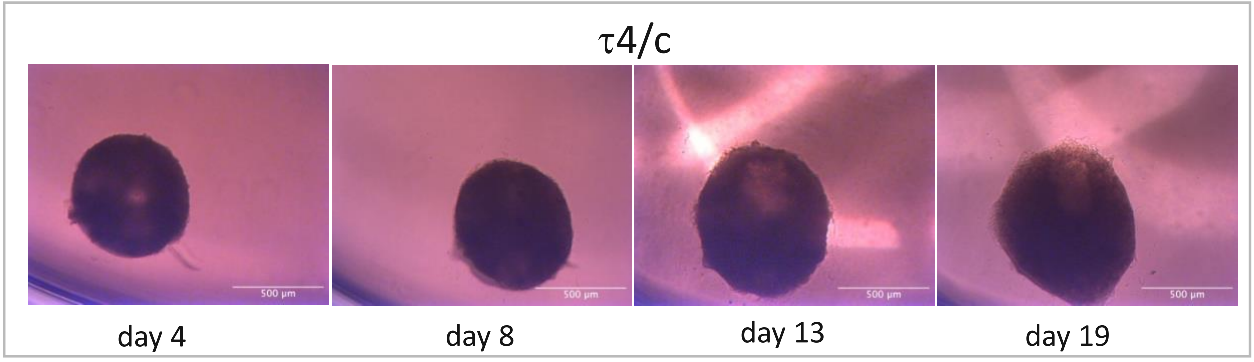
τ4/c
day 4 day 8 day 13 day 19

Figure 44 Images from the spheroid conditions [50.000cells/proliferation-medium-seeding/poly-L-lysine]. Timeseries of spheroid τ4/c ranging from day 4 to day 19. A slight flattening of the spheroid can be observed due to an increase in the area and changes in the morphology, especially on the edges of the spheroid.

A very weak formation of neuronal processes could be observed as can be seen in the immunostaining image in Figure 45 if looked closely.

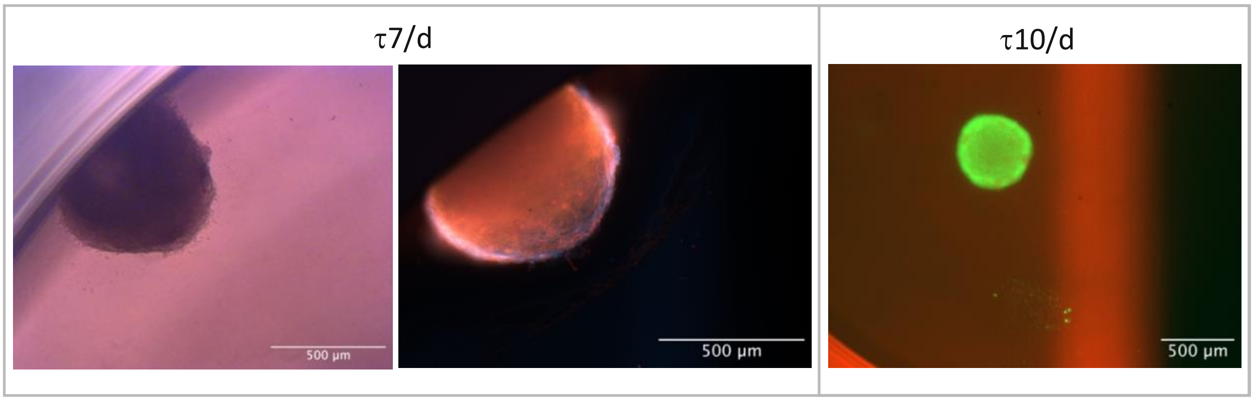

Figure 45 Images from the spheroid conditions [50.000cells/proliferation-medium-seeding/poly-L-lysine]. Brightfield (left) and immunostaining (middle) images of τ7/b. The middle image was taken with widefield microscopy and nuclei were stained with Hoechst 33342 solution (blue), β-III tubulin with Alexa 546 (orange) and tyrosine hydroxylase with Alexa 647 (red). This spheroid was the only sample from these conditions that was not removed during immunostaining, presumably due to its position on the well wall. The results of immunocytochemistry will be discussed in its own section. This image from live/dead staining of τ10/d (right) shows a loose spheroid and the traces of its outgrowths onto the well plate in widefield. The membranes of viable cells were stained with calcein-AM (green) and the nuclei of dead cells with ethidium homodimer-1 (red). The spheroidal outgrowth connecting the spheroid to the well plate seemed to have been damaged by the PBS washing.

Live/dead staining was conducted for τ10 where two of the four spheroids were lost during washing. The other two seemed to have been moved during the washing process as indicated by a deviation in position and living residual cells in their vicinity (Figure 45/right). The spheroid τ7/d could be imaged with immunostaining. This spheroid stuck to the wall of the well which contributed to its adhesion as it emerged as a pattern that could be observed with the other conditions as well.

75.000 cells per spheroid

This condition was only tested with τ4 since not enough 75.000-cell spheroids formed with proliferation medium seeding were available due to a low cell number after splitting. The time series in Figure 46 shows a partial flattening of the spheroidal structure and a limited number of neurite projections can be recognized in Figure 47.

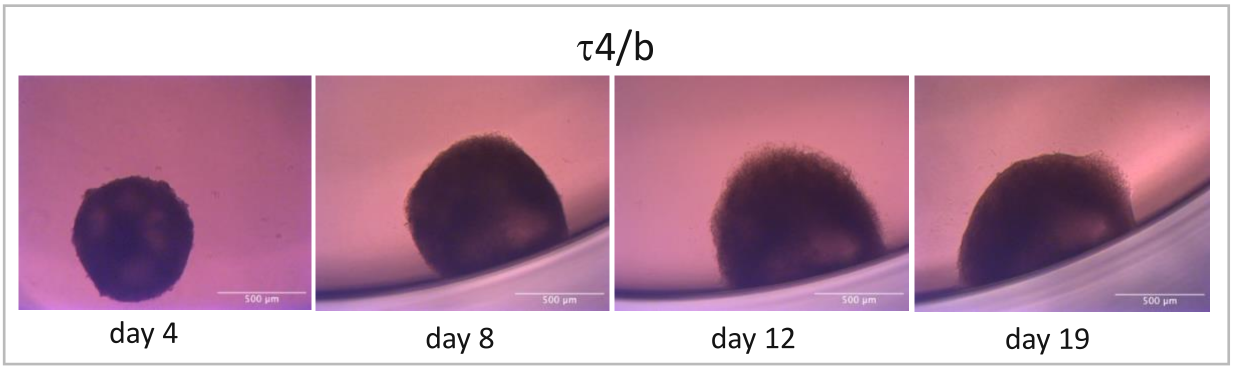

Figure 46 Images from the spheroid conditions [75.000cells/proliferation-medium-seeding/poly-L-lysine]. A) Timeseries of spheroid τ4/b[75.000cells/proliferation-medium-seeding/poly-L-lysine] from day 4 to day 19. The spheroid flattened albeit in an anisotropic manner due to its position at the well wall. The edges appear the most diffuse on day 12 and differently shaded spots with changing sizes can be seen on the images presumably reflecting variations in cell density. In addition, the central thickness of the spheroid decreased through adoption of an oval shape indicating cellular rearrangements in the spheroid.

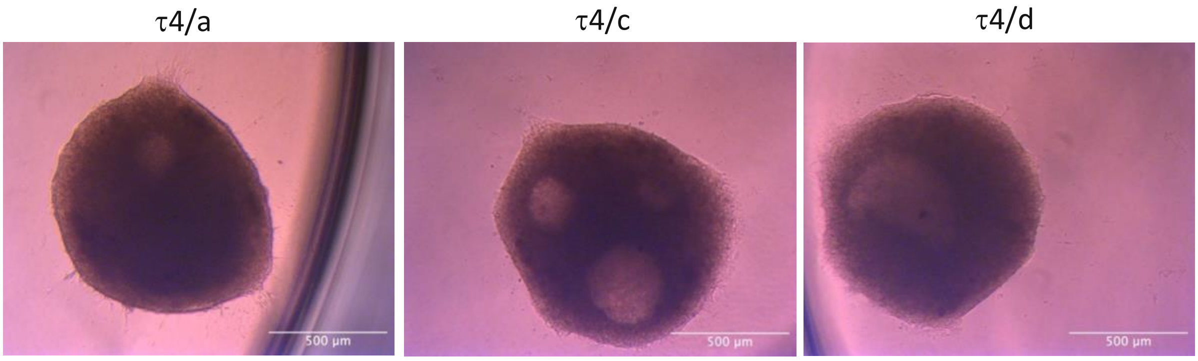

Figure 47 Images from the spheroid conditions [75.000cells/proliferation-medium-seeding/poly-L-lysine] Images of the spheroids τ4/a(left), τ4/c(middle) and τ4/d(right) taken at day 19. Formation of single, short cellular projections can be observed in τ4/and τ4/d. Differently shaded spots can be observed in the spheroids presumably indicating an asymmetric flattening of the spheroids with clusters of lower cellular density.

Sample τ4/c shows three major clusters with increased light transmission which presumably indicates an unevenness in cell density related to the flattening of the spheroid Figure 47. From the four spheroids only b which adhered to the well wall remained after immunostaining which resembled the outcome for the middle-sized spheroids under the same conditions.

3.2.2.7 Spheroids on Poly-L-Lysine with Differentiation Medium Seeding

25.000 cells per spheroid

With differentiation medium seeding all 25.000-cell spheroids except τ10/a showed formation of projections, most pronounced with τ10/d as can be seen in Figure 48.

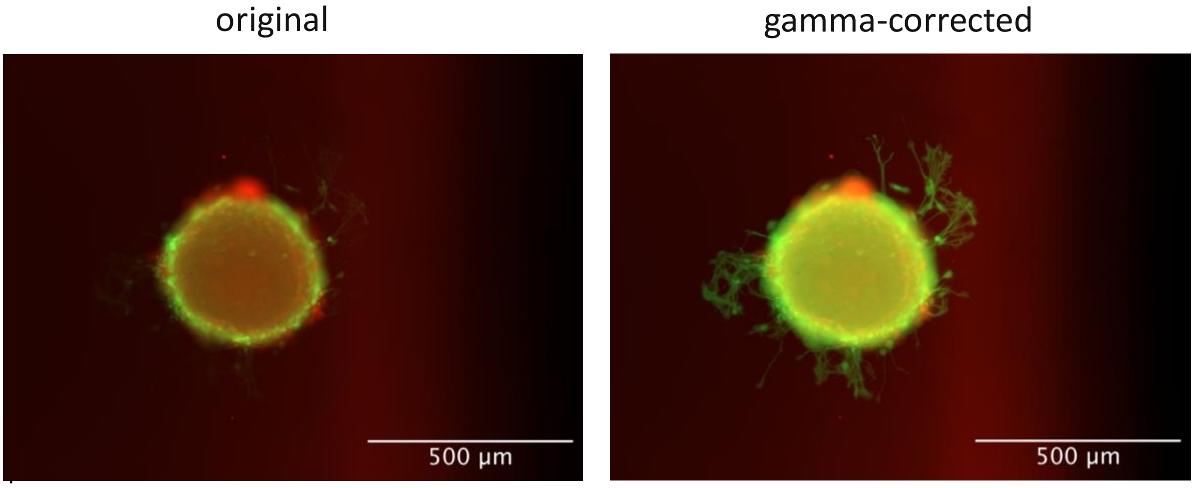

Figure 48 Live/dead staining of spheroid τ10/d[25.000cells/differentiation-medium-seeding/poly-L-lysine] in the original (left) and gamma-corrected (right). The membranes of viable cells were stained with calcein-AM (green) and the nuclei of dead cells with ethidium homodimer-1 (red). The image was taken in widefield. Due to the multilayered nature of the sample the neuronal processes are only partially recognizable since most of the light was emitted from the bulk of the spheroid. Gamma-correction was used to make the neuronal processes visible such that these images could be used to assess their density and trajectory.

Albeit the formation of outwards projections was weak or intermediate this stands in clear contrast to proliferation medium seeding where they formed no projections and clear signs of cell viability were absent for the same spheroid size. With τ4 the samples were washed away during immunostaining unless they adhered to the well wall like under the previously

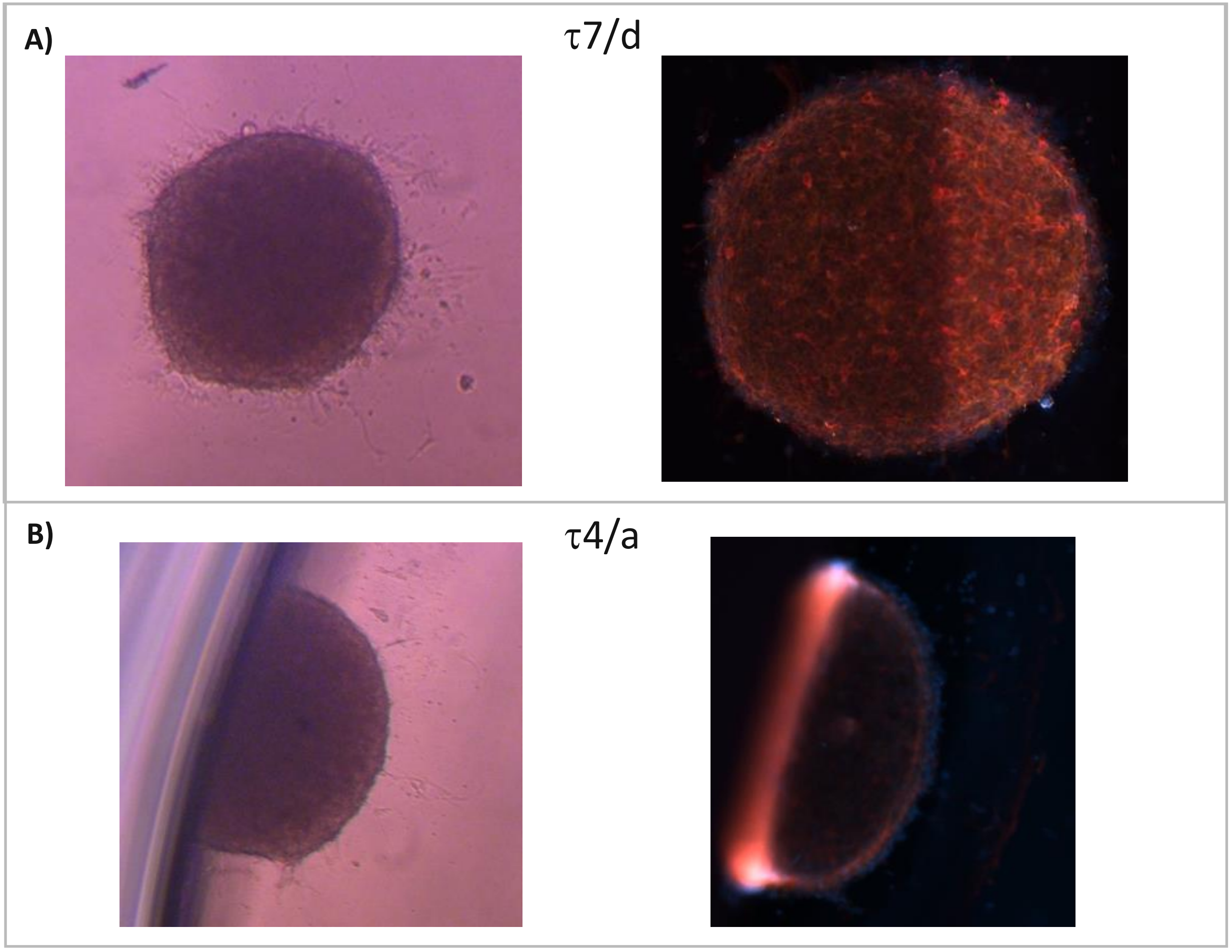

Figure 49 Images from the spheroid conditions [25.000cells/differentiation-medium-seeding/poly-L-lysine]. A) Spheroid τ7/d before (left) and after immunocytochemistry (right) and (B) Spheroid τ4/a before (left) and after immunocytochemistry (right). The immunocytochemistry images were taken with widefield microscopy and nuclei were stained with Hoechst 33342 solution (blue), β-III tubulin with Alexa 546 (orange) and tyrosine hydroxylase with Alexa 647 (red). While the brightfield microscopy shows plenty of neuronal processes they can be hardly seen on fluorescence images why they appear to have been damaged by the fixation process and the various washing steps with PBS. The results of immunocytochemistry will be discussed in their own section.

discussed conditions (Figure 49/B). All three τ7 samples remained in the well during immunostaining indicating a better adhesion presumably due to higher cell viability. During live/dead staining with τ10 sample d was the only one of the three to remain in the well (Figure 49). Why they were removed despite their formation of axon networks and while similar spheroids did not is unknown. Although the protruding axons are not all fully recognizable in the original image gamma-correction could be used to increase their visibility. From the comparison between the images from immunostaining (Figure 49/right) and brightfield microscopy (Figure 49/left) it could be concluded that the fixation process damaged the projections and primed them for removal by the washing steps. This is further discussed in the section conclusions 4. Since the plate on which the samples with τ10 were cultivated was not identical to the plate used for the other transfer timepoints the deterioration in adhesion might have been due to problems with the coating on this specific plate.

50.000 cells per spheroid

With differentiation medium seeding 2 the 50.000-cell spheroids generally formed many protruding axons although with limited outwards reach due to their coiling as it is most visible in Figure 50/B.

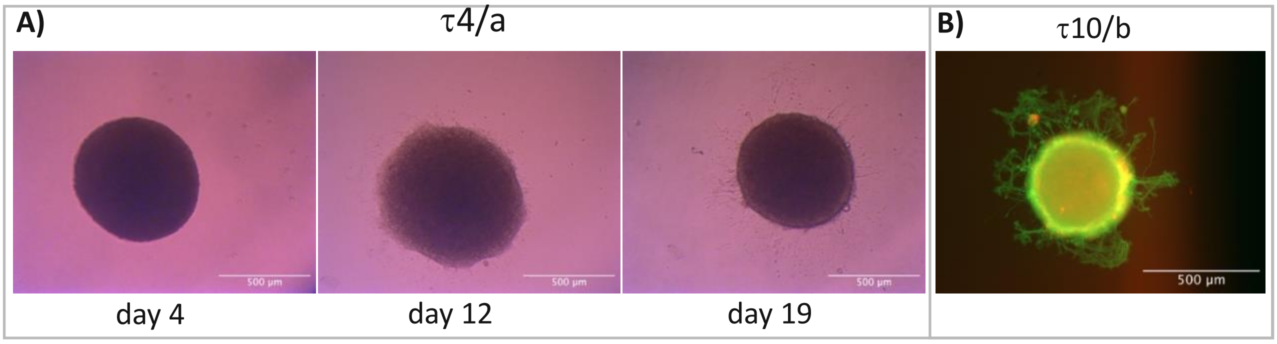

Figure 50 Images from the spheroid conditions [50.000cells/differentiation-medium-seeding/poly-L-lysine]. A) Time series of spheroid τ4/a from day 4 to day 19. The edges of the spheroid get diffuser from day 4 to day 12 while the area of the spheroid increases. Until day 19 the edges of the spheroid sharpened again, and its circumference receded again while axons started projecting outwards from the spheroid. B) Live/dead image of spheroid τ7/b in widefield where gamma-correction was used to make the protruding axons more visible. The membranes of viable cells were stained with calcein-AM (green) and the nuclei of dead cells with ethidium homodimer-1 (red). With greater density of projections, they are more bundled together and project less outwards than when they are isolated.

As it can be seen in the time series in Figure 50/A the spheroids were initially flattening and their edges became more diffuse and many projections were formed (day 12), but timewise correlated with the formation of protruding axons the edges became sharper again (day 19). Although the spheroids with τ4 were washed away during immunostaining three out of four spheroids kept adhering and could be imaged with τ7 and τ10. Since the spheroids with τ4 & τ7 were cultivated on the identical well plate this difference seems to indicate inferior formation of adhesion sites for τ4. One alternative explanation would be manual mishandling of the respective samples leading to physical force on the spheroids.

75.000 cells per spheroid

The 75.000-cell spheroids had very dense networks of protruding axons and a comparable morphology to the 50.000-cell spheroids. As can be seen in Figure 51/A the spheroid’s edges initially became more diffuse while its area increased during flattening, but the edges became sharper again with the outwards projection of axons. The axon bundles were comparatively dense for all samples, but greater for τ4 spheroids than for later transferred ones. One sample that formed relatively few projections was spheroid τ7/c as it can be seen in Figure 51/B. The spheroids τ7/a and τ10/a formed no projections and did not show significant flattening, which shaded doubts about their cells’ viability. As with the middle-sized spheroids the ones with τ4 were washed away during staining while 3 out of 4 spheroids maintained their adherence with τ7 & τ10. This might lead to the assumption that the spheroids should be transferred after day 4 for better adhesion, but due to physical proximity on the culture plate physical mishandling of the samples should not be ruled out as an explanation. In Figure 51/C gamma correction was used to make the dense axon bundles of spheroid τ10/c more visible. This sample represented the very dense formation of projections coupled with an intense coiling which seemed to have limited the outwards growth that was achieved with these conditions.

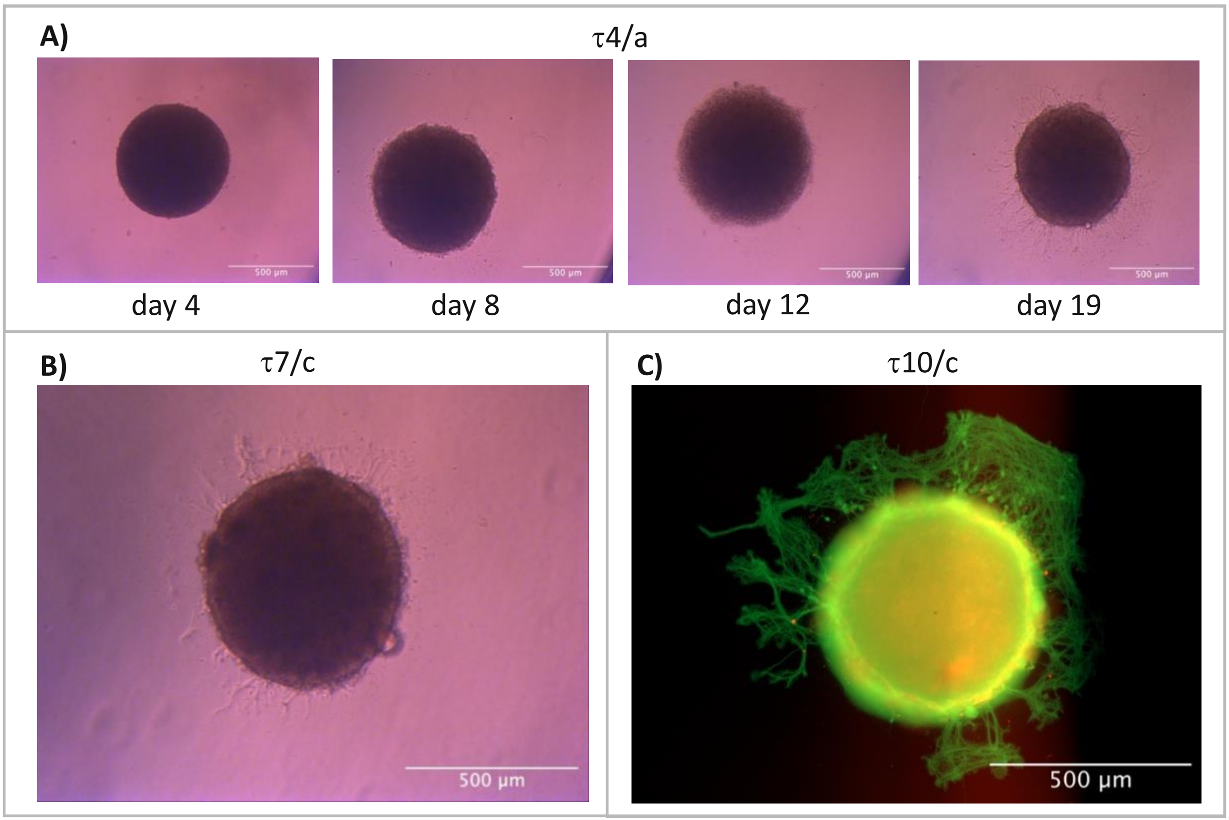

Figure 51 Images for spheroids conditions [75.000cells/differentiation-medium-seeding/poly-L-lysine]. A) Time series of spheroid τ4/a from day 4 to day 19. The edges of the spheroid get more diffuse until day 12, but until day 19 sharper again and a dense network of neuronal processes is now visible. B) spheroid τ7/c on day 19 which looks comparable to τ4/a although with less outwards projecting axons. C) Live/dead image of spheroid τ10/c in widefield which shows its dense network of coiled neuronal processes. The membranes of viable cells were stained with calcein-AM (green) and the nuclei of dead cells with ethidium homodimer-1 (red). The coiling seems to have caused a significant reduction in their outwards projection.

In conclusion it can be clearly said that proliferation medium seeding yielded better results for all conditions on PLL. The spheroids did not flatten which can be attributed to the lack of physiological ECM molecules necessary for focal adhesion. Some spheroids build very dense neural networks, but the axons did not spread very far. Geltrex might be assumed to lead to a different outcome because it better resembles the natural physiology cells are exposed to *in-vivo*.

3.2.2.8 Spheroids on Matrigel with Proliferation Medium Seeding

25.000 cells per spheroid

The 25.000-cell spheroids generated using proliferation medium seeding largely kept their spheroidal shape with some of them completely flattening during the cultivation on Geltrex. The flattening of the spheroids was accompanied by a rapid proliferation of cells in the surrounding for τ4 (Figure 52/A) to τ10, with τ10 showing mayor variability between the four samples.

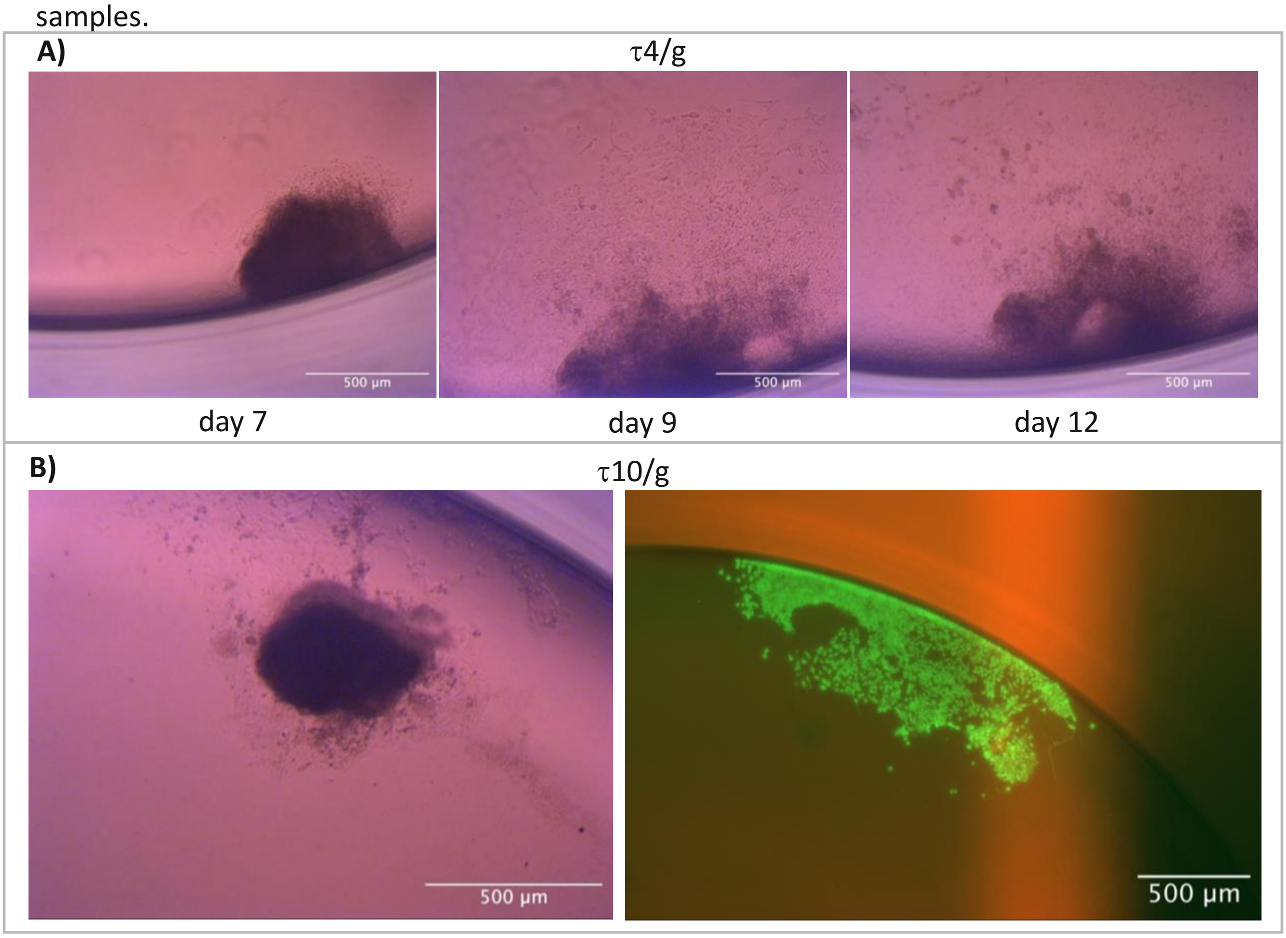

Figure 52 Images for spheroid conditions [25.000cells/proliferation-medium-seeding/Geltrex]. A) Time series of spheroid τ7/g from day 7 until day 12. The spheroid flattened fast and structural reorganization is evident especially due to the "moving hole" in day 9 and day 12. Neurite projections could not be recognized. B) Brightfield (left) and live/dead imaging in widefield (right) for τ4/g. For live/dead imaging membranes of viable cells were stained with calcein-AM (green) and the nuclei of dead cells with ethidium homodimer-1 (red). While the spheroid largely retained its form some cells have been detached from the spheroid and started proliferating in its vicinity. The cells largely have a mixed morphology between undifferentiated and differentiated hVM1 cells. Some of the cells with a more differentiated morphology have developed observable neuronal processes.

A structural rearrangement of the samples could be observed as indicated by the "moving holes" in the cell culture. The spheroids with τ13 & τ16 flattened over much smaller areas indicating more advanced differentiation before transfer. Although it is hardly recognizable on the brightfield images the live/dead images clearly show some of the proliferated cells with a neurite-like morphology and small projections emanating from them (Figure 52/B). Despite this most of the cells seemed to have an intermediate morphology between stem cells and neurites, indicating that retention of proliferation medium in the spheroidal core had a significant effect. Images from immunostaining only showed spheroidal fragments that were hardly interpretable, and no cell monolayers were observed.

50.000 cells per spheroid

With proliferation medium seeding the 50.000-cell spheroids lost their spheroidal form through rupture into smaller parts and rearrangements in tandem with cell proliferation and migration as can be seen in Figure 53.

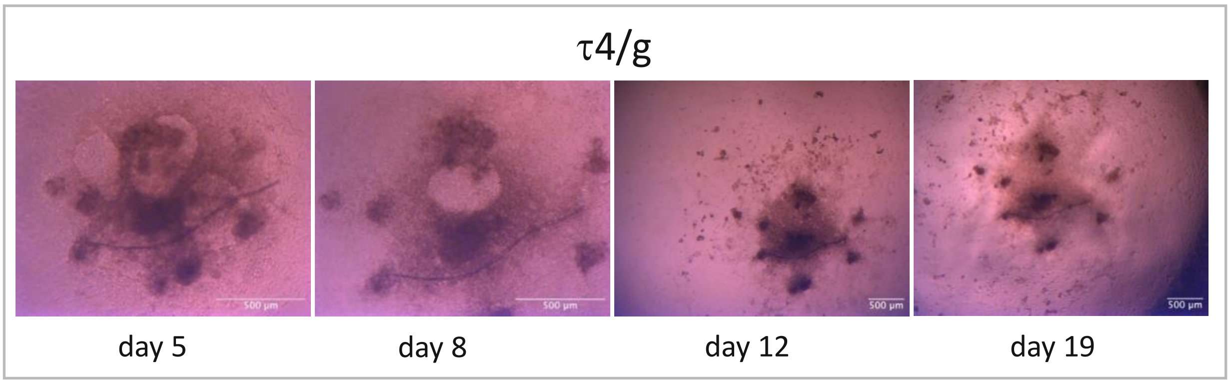

Figure 53 Images for spheroids conditions [50.000cells/proliferation-medium-seeding/Geltrex]. A) time series of spheroid τ4/g from day 5 until day 19; The images showed an intense rearrangement of the culture between the different time points as indicated by the clusters of increased and decreased light transmission. As with the other τ4 samples the culture spread over a great area compared to the initial spheroid size.

In this process thick spheroidal fragments remained between the proliferating cells as can be seen by their darker shade. While the spheroids with τ4 & τ7 spread unevenly over a larger area Figure 53 the spheroids with τ13 & τ16 spread over a smaller area with greater uniformity Figure 54.

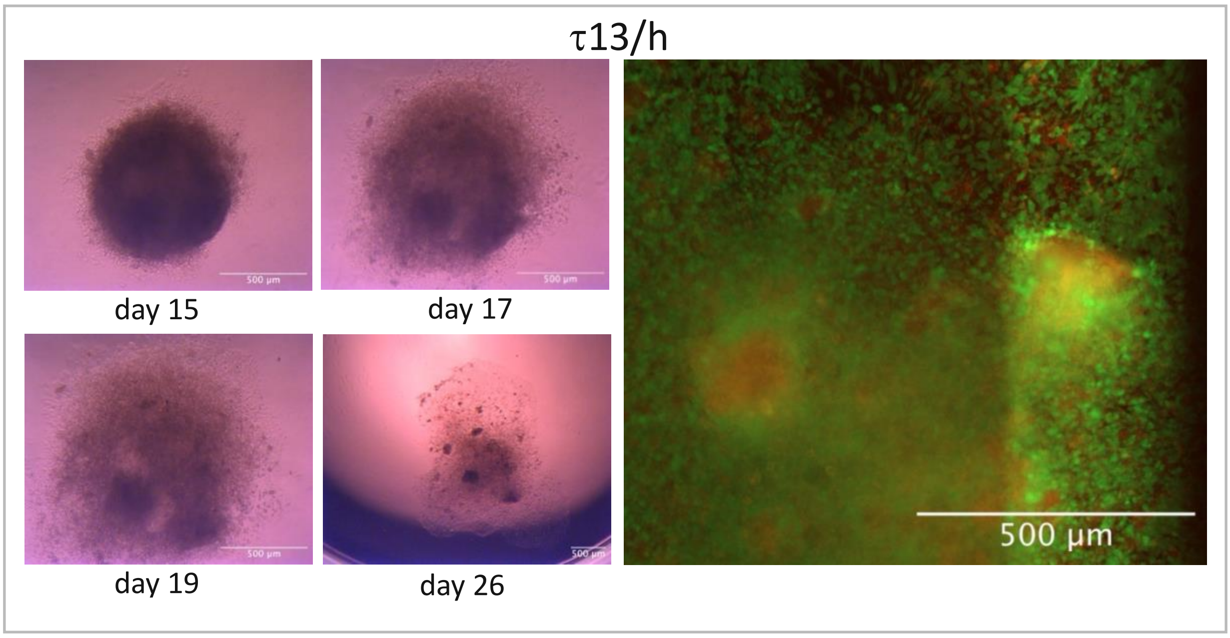

Figure 54 Images for spheroids conditions [50.000cells/proliferation-medium-seeding/Geltrex]. Times series (left) and live/dead image in widefield (right) for spheroid τ13/h where membranes of viable cells were stained with calcein-AM (green) and the nuclei of dead cells with ethidium homodimer-1 (red); The time series shows a different course of flattening compared to A). The cell culture ended up occupying less area and the clusters of high cell density were bigger and less numerous. The live/dead staining showed dead cell clusters with varying size interspersed with living cells. These clusters of dead cells seemed to have downward pointing edges constituted of living cells which could explain the special rearrangements that were observed during flattening.

In this process thick spheroidal fragments remained between the proliferating cells as can be seen by their darker shade. While the spheroids with τ4 & τ7 spread unevenly over a larger area (Figure 53/A) the spheroids with τ13 & τ16 spread over a smaller area with greater uniformity (Figure 54). The samples with τ10 showed an intermediary behavior. While the earlier two transfer timepoints yielded no visible outwards projection of axons the later three did to some extent. In clear contrast to the observed axons on poly-L-lysine the axons projected far more outwards on Geltrex, but they were far sparser as can be seen in Figure 55.

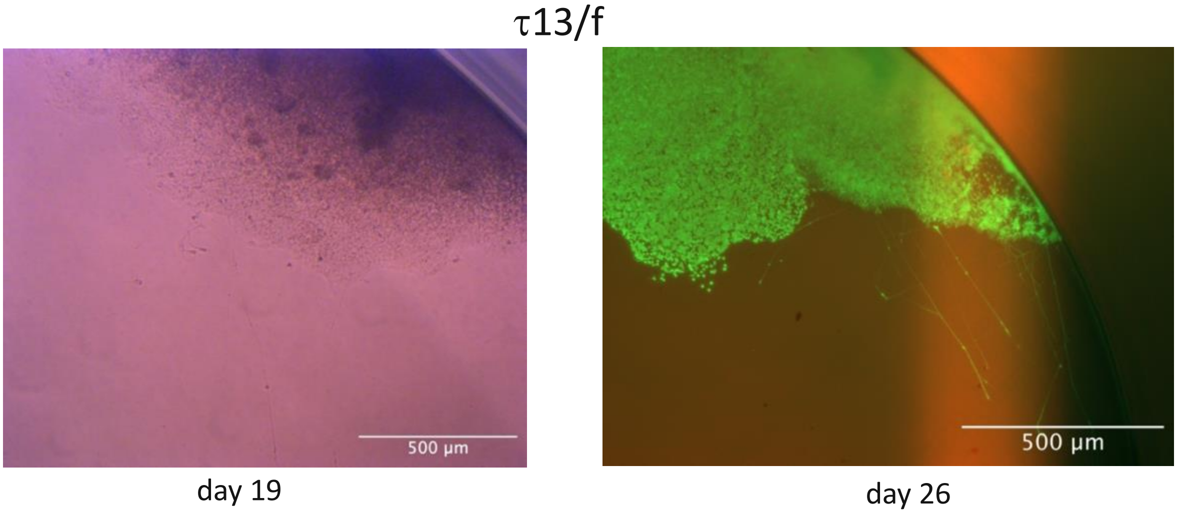

Figure 55 Images for spheroids conditions [50.000cells/proliferation-medium-seeding/Geltrex] Brightfield microscopy (left) and live/dead staining in widefield (right) for spheroid τ13/f. For live/dead imaging the same staining was applied as in (B). A limited number of outwards projecting axons could be observed which did only show minor coiling and had increased length compared to the protruding axons formed on PLL.

Live/dead staining showed larger and smaller clusters of dead cells with living cells surrounding and covering them (Figure 54 on the right). These clusters seem to stem from a break-up of the necrotic core driven by living cells on their outer edge as supported by the live/dead image of spheroid τ13/g. In Figure 55 gamma-correction was used to grant the neuronal processes better visibility which made the dead cells less visible. The samples did not get removed during immunostaining which indicated better adhesion on Geltrex compared to PLL.

75.000 cells per spheroid

Due to an insufficient number of 75.000-cell spheroids only τ4 was realized. This low number of spheroid came from a low number of cells at the timepoint of splitting. Their morphology closely resembled the 50.000-cell spheroids with the discussed structural and spatial rearrangements into clusters of distinct cell densities and their spread over a large area (Figure 56).

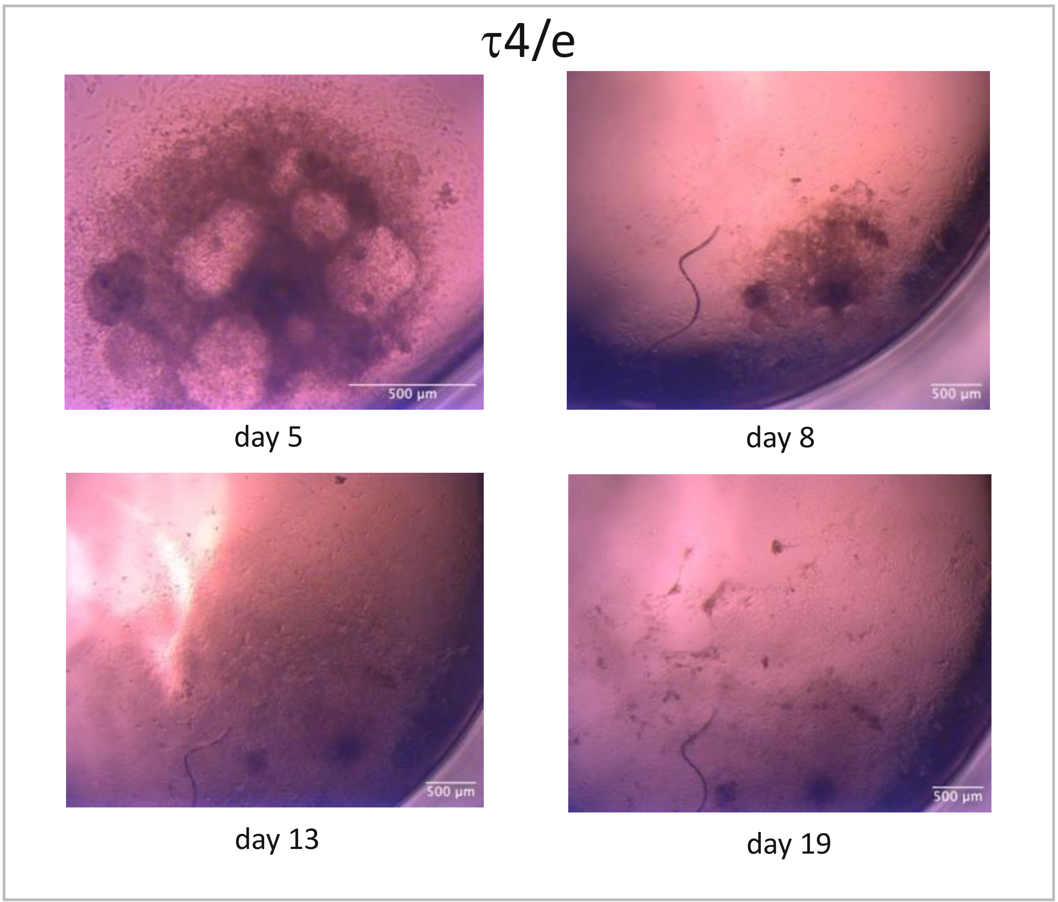
τ4/e

day 5

day 8

day 13

day 19

Figure 56 Time series of spheroid τ4/e[75.000cells/proliferation-medium-seeding/Geltrex]. The time series shows a comparable course of flattening as spheroid τ4/g[50.000cells/proliferation-medium-seeding/Geltrex] in Figure 55, albeit this spheroid spread over a larger presumably due to the earlier transfer timepoint and bigger size.

No formation of neuronal processes could be recognized. The samples did not get washed away during immunostaining albeit partial damages cannot be ruled out.

In summary it can be said that comparable to proliferation medium seeding on PLL proliferation medium seeding on Geltrex does not lead to dense axonal networks. The next condition that will be discussed is the culture of spheroids formed with differentiation medium seeding on Geltrex.

3.2.2.9 Spheroids on Geltrex with Differentiation Medium Seeding

25.000 cells per spheroid

With differentiation medium seeding the 25.000-cell spheroids flattened relatively smoothly and lost their spheroidal shape more readily than the samples from the previous sections. The spheroids with τ4 & τ7 flattened uniformly while the spheroids with later transfer days retained some distinct clusters as can be seen in Figure 57A & B.

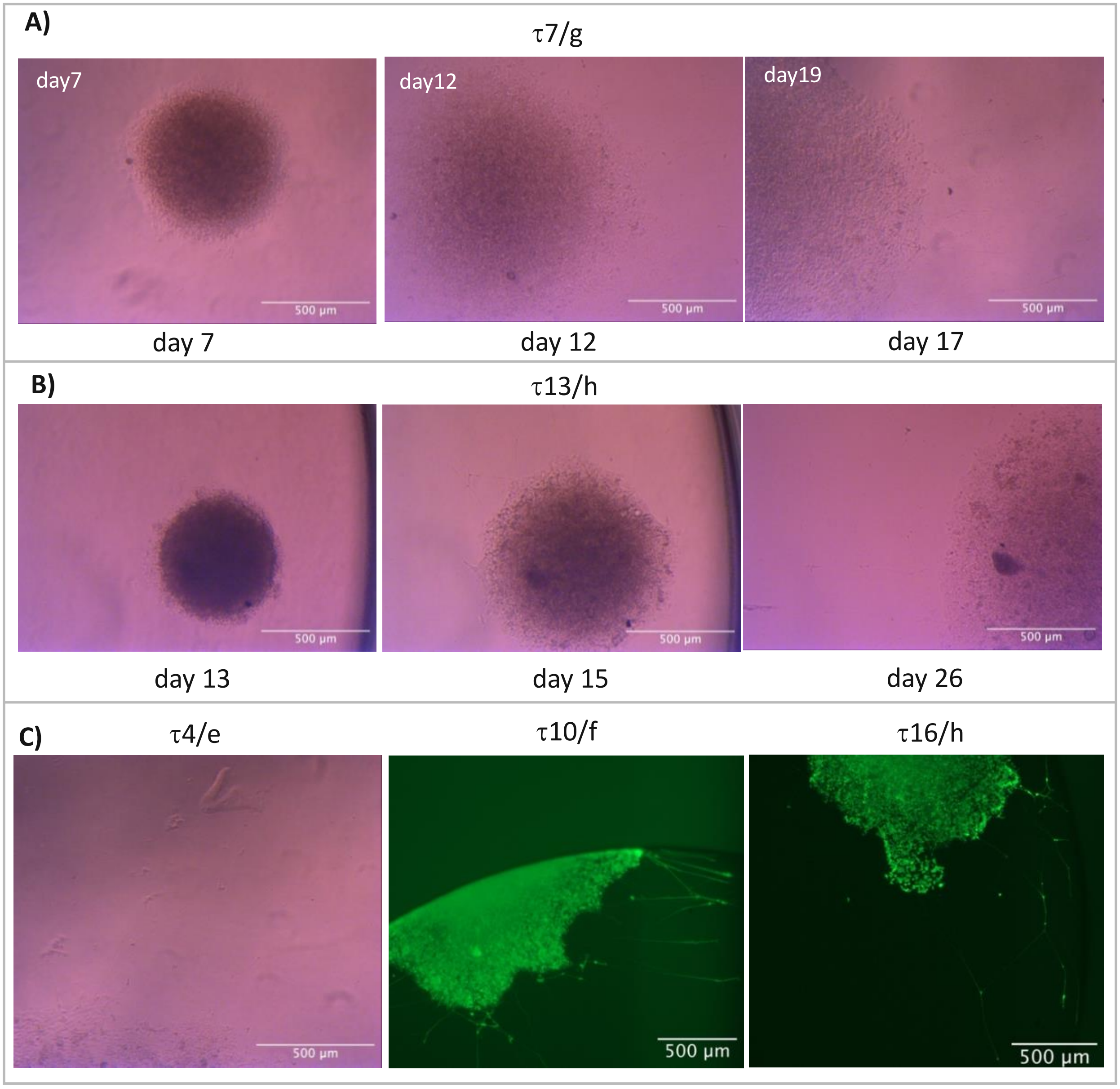

Figure 57 Images for spheroid conditions [25.000cells/differentiation-medium-seeding/Geltrex]. A) Time series of spheroid τ7/g from day 7 until day 17. The spheroid flattened rather uniformly, and protruding axons can be observed at day 12 & 17. The number of projections is low compared to the samples on PLL with differentiation medium seeding but they projected radially more outwards due to the lesser coiling. B) Time series of spheroid τ13/h from day 13 until day 26. The sample flattened less uniformly leading to clusters of higher density that could be seen most distinctly at day 26. Outwards growth of axons was comparable to τ7/g. C) On the left is τ4/e as an example of long and relatively dense formation of axons at earlier transfer timepoints. The samples τ10/f (middle) and τ16/h (right) show live images in widefield and represent later transfers that, although they could not compete with the outlier τ4/e, were better than the other spheroids with early transfer time. For live images the membranes of viable cells were stained with calcein-AM and the live images were gamma-corrected to better visualize the protruding axons.

As it can be seen in Table 16 and Table 16 and Figure 57/C these conditions led to relatively strong formation of protruding axons in some samples, while most samples had a mediocre performance. Here the samples with τ4 & τ7 showed higher variability while the samples with later transfer timepoints showed more uniformity regarding axon growth. While these projections were nearly completely washed away during immunostaining, they are clearly visible on the live/dead images in Figure 57/C. From comparison between the live/dead images to brightfield images taken before sample preparation it can be seen that the washing led to a partial loss of cells.

50.000 cells per spheroid

The 50.000-cell spheroids formed denser and wider networks of protruding axons compared to the smaller spheroids as can best be seen on the live images in Figure 58/B.

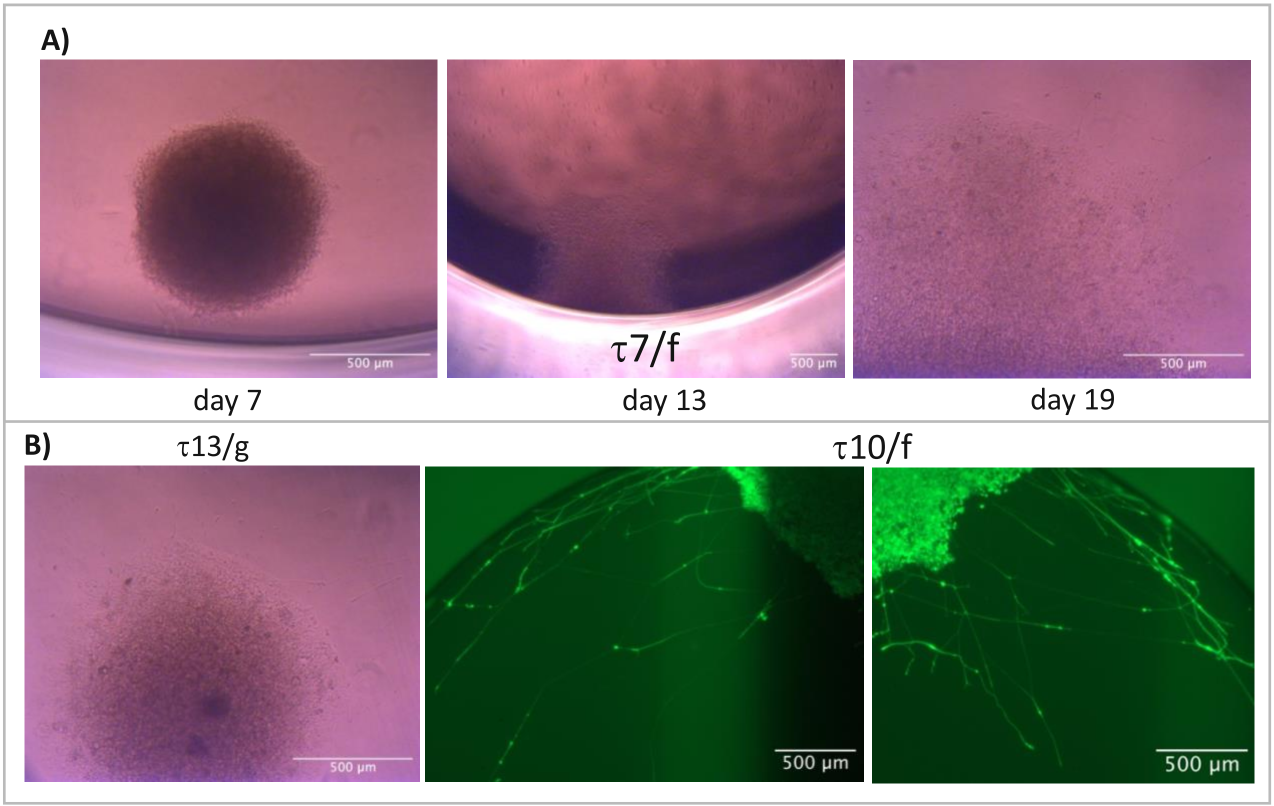

Figure 58 Images for spheroid conditions [50.000cells/differentiation-medium-seeding/Geltrex]. A) Time series of spheroid τ7/f; due to the proximity to the well wall the spheroid did not flatten in all directions evenly, but high uniformity is given along concentric lines. Protruding axons can be seen on day 19 and to a much lesser extend on day 13 in part due to the smaller magnification. B) Brightfield image of spheroid τ13/g (left) and the gamma corrected live images of spheroid τ10/f (middle & right) in widefield where the membranes of viable cells were stained with calcein-AM; although some projections are clearly visible on the brightfield image the live image renders it much easier to recognize the neuronal processes. The protruding axons formed under these conditions projected far wider compared to cultivation on PLL, but they numbered far less in comparison.

As Figure 58/A shows these samples had a similar morphology and flattened in a similar course as the 25.000-cell spheroids on Geltrex. This implies that these spheroids flattened into more uniform clusters than spheroids of the same size generated with proliferation medium seeding. The protruding axons appeared slightly more uniform regarding their spatial distribution than in comparison with the smaller spheroids. While the results seemed indecisive for early transfer days it appears that 50.000 cell spheroids yielded better results than the smaller spheroids when transferred later. In Figure 58/B gamma correction was used to visualize the wide network of neuronal processes of spheroid τ10/f.

In conclusion it can be said that the spheroids on Geltrex flatten and that their axon networks can be very wide, but they are always thin compared to the networks from the spheroids on PLL.

75.000 cells per spheroid

The 75.000-cell spheroids with τ4 & τ7 largely resembled the 50.000-cell spheroids with τ13 & τ16 in regard to their morphology and the density of protruding axons as can be seen in Figure 59.

τ7/f

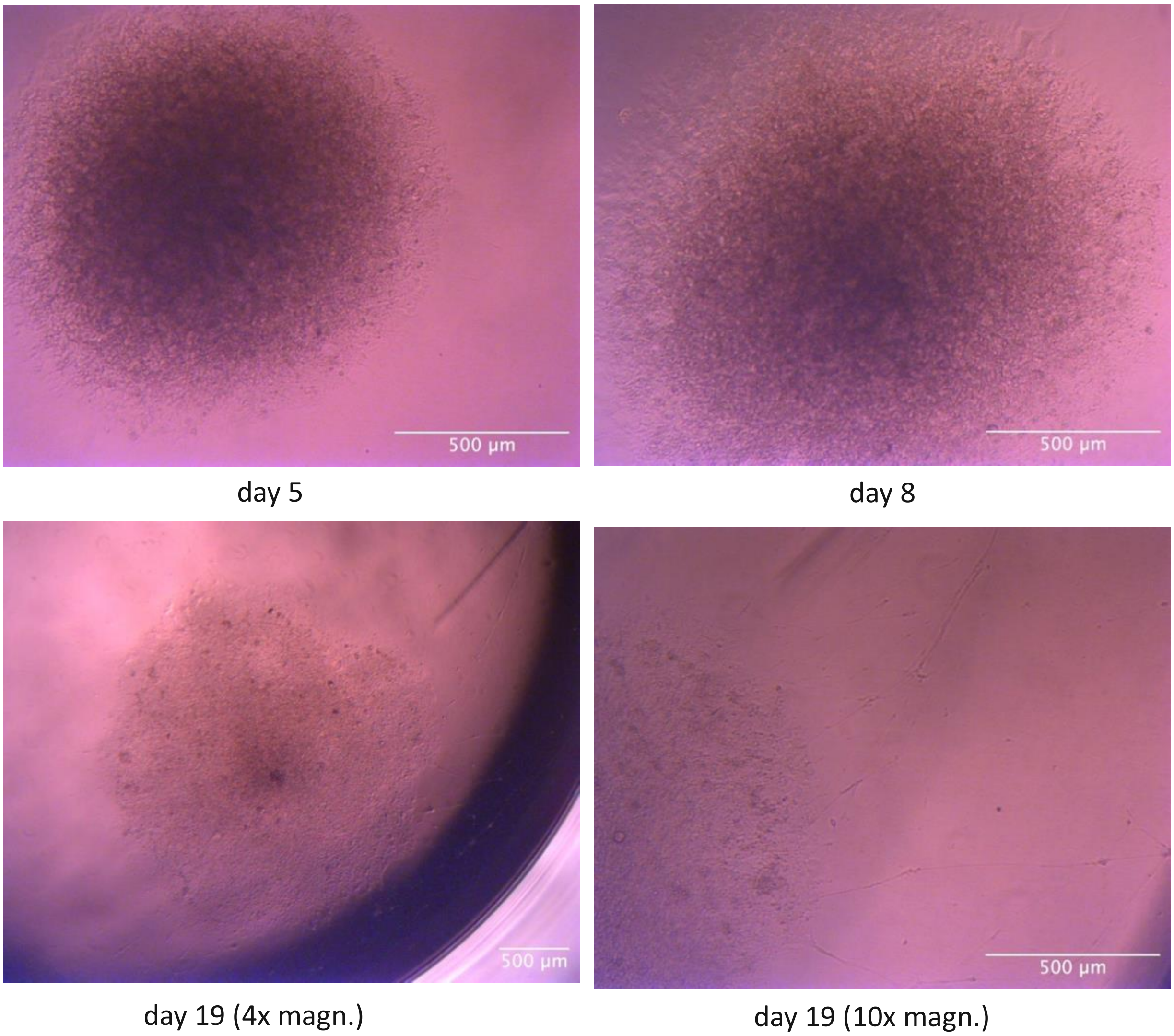

day 5

day 8

day 19 (4x magn.)

day 19 (10x magn.)

Figure 59 Time series of spheroid τ4/f[75.000cells/differentiation-medium-seeding/Geltrex] from day 5 to day 19. A greater radial gradient in cell density is visible here than with the smaller spheroid sizes presumably due to a higher number of cells per area. Concentrically variability in cell density seemed minor in comparison. On day 19 protruding axons are eminent as can be best seen on the bottom right due to the higher magnification. Although a coiling of these projections can be observed, these coils still projected outwards unlike the coils formed on PLL.

In contrast to the similarity the center of the culture seemed to have retained a higher cell density presumably due to a larger number of cells per area being an obstacle for flattening. Since the spheroids with $\tau10$ all happened to adhere close to the well wall they were forced to flatten anisotropicly which rendered them with a different appearance than $\tau4$ & $\tau7$. In regard to the density of projections and their length the 75.000-cell spheroids showed on average the best outcome of the spheroids on Geltrex, but the greater variability within some 25.000-cell spheroids gave rise to some samples with competing performance. The live/dead images only marginal showed projections which was in contrast to the brightfield imagery which therefore indicated their abrasion during washing. Why the projections got destroyed during sample preparation with 75.000, - but not with 50.000-cell spheroids is unknown.

In summary it can be concluded that differentiation medium seeding leads to better results for both cultivation on Geltrex and PLL. This may be caused by increased necrosis in the core of the spheroids due to medium retention which might increase the metabolic rate and thus oxygen demand. Geltrex coating induces a spheroid flattening while PLL coating does not. In addition, the neural networks formed on Geltrex were very wide but thin while the ones on PLL were very dense but did not span over a large area. This might both be attributed to the presence of physiological matrix proteins which PLL lacks. Although the results are far superior in comparison to the protocol used for cultivation in the two-chamber device it does not seem like the spheroids could compete with the dense and wide axonal networks formed by brain organoids.

3.2.3. Brain Organoid Culture in One-Chamber Guidance Devices

The cultivation of brain organoids in the 3D printed devices was a major goal of the project but since the necessary laboratories and expertise for their cultivation were lacking at DTU the one-chamber guidance devices were transferred to Lund university where they were tested for the cultivation of midbrain-like organoids and forebrain-like organoids by the project partners according to their protocols[65]. The same batch of organoids was also used for cultivation with the guidance device from Osaki et al.[55] as a control. The one-chamber devise was designed after the spheroid cultures in the two-chamber device and one of the specific design considerations was to increase the bottom area to prevent leakage of cell medium like it occurred with the two-chamber design. The reasoning for the two chambers in the older design were meant to avoid convective mixing after filling of the connecting channel with hydrogel but this idea was set aside to reduce the complexity of the experiments. The one-chamber device is shown from the bottom in Figure 60 from the top (A) and from the bottom (B). In order to minimalize the risk for contamination of the one-chamber devices channel width and well size were not measure directly from the selected specimen used for culture. Instead, a sample from the same batch (Figure 61) was measured which gave a channel width of $\sim 900\ \mu\text{m}$ and a well diameter of $\sim 2500\ \mu\text{m}$. These measurements may be prone to the problems discussed in the section z-alignment 3.1.3.

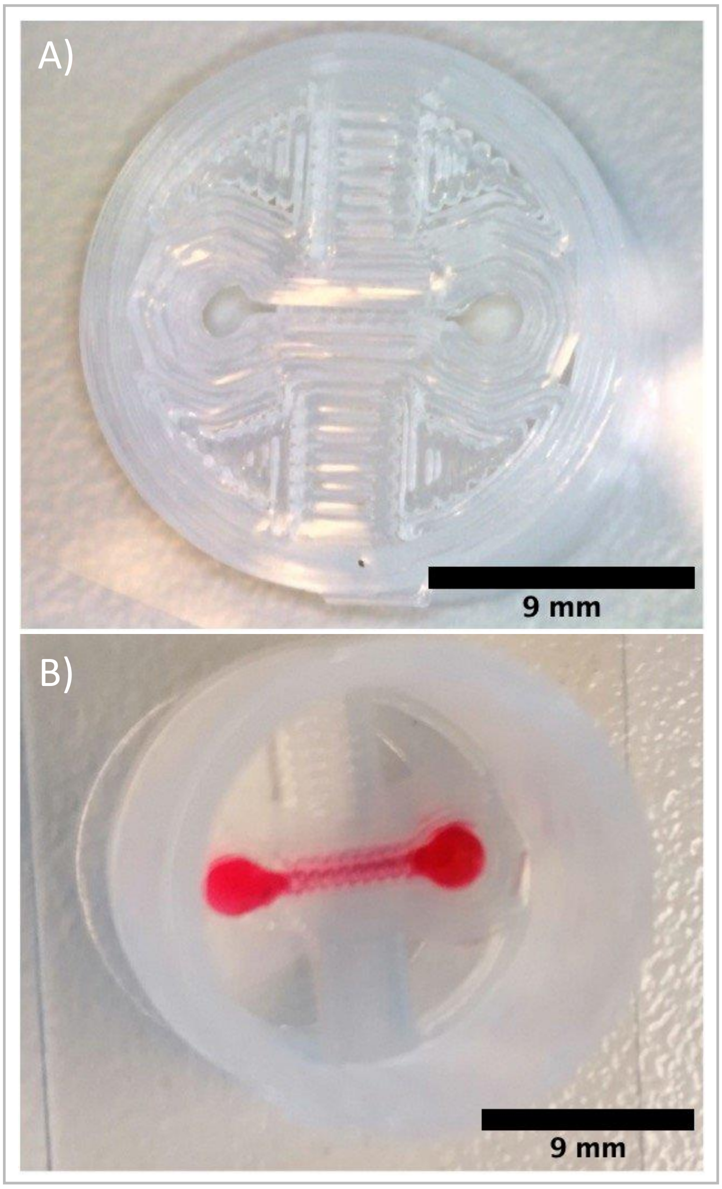

Figure 60 One-chamber guidance device from the bottom (A) and from the top (B). The bottom side of the devices was accessible due to the use of a passivated wafer as a substrate for printing (explained in ***Error! Reference source not found.****).*

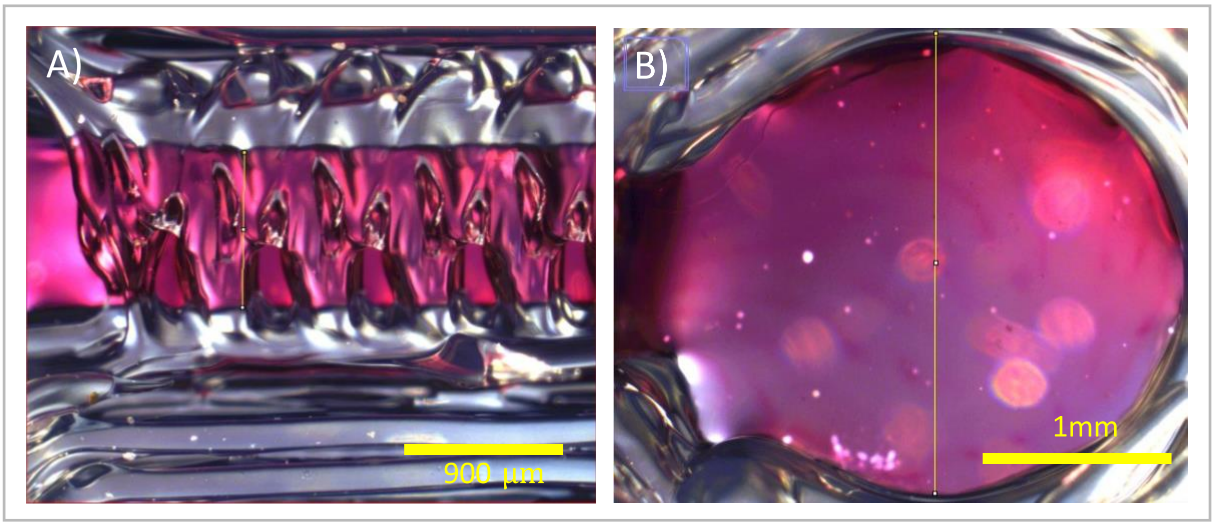

Figure 61 Measurement of channel width and well diameter of the one-chamber device. The smaller yellow lines in A & B correspond to 905 & 2499 µm respectively and were from the original measurements.

Since the alignment methods were not advanced properly at the time of production of the one-chamber devices a larger variability in respect to channel width & well diameter can be assumed. The cultivation was done until day 90. The images provided by Lund university (Figure 62) showed axonal penetration of the channels but the axons did not bundle into fascicles presumably due to the broad channel width.

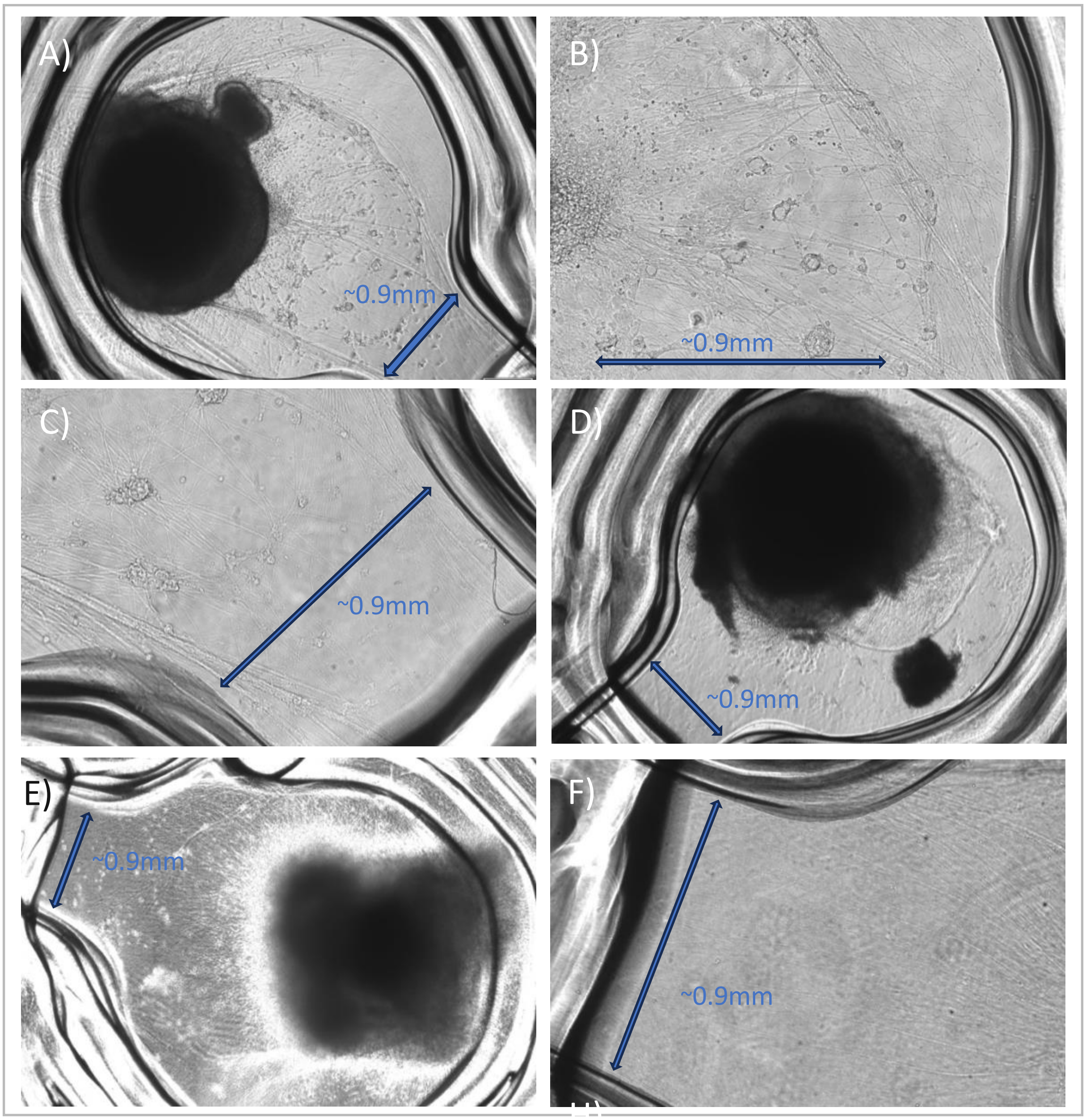

Figure 62 Images from organoid culture in the one-chamber guidance devices taken on day 26 of culture or day 10 after transfer into the devices. The images were provided by Lund university. The scale bars are estimated from the device geometry since accurate scale bars were not provided. The images A, B & C as well as E & F depict the same organoid respectively. The axonal protrusions did not bundle into fascicle but did project loosely into the channels. According to the analysis from Lund university the organoids were healthy until day 30 but their condition deteriorated progressively from that point. Since other organoid cultures that utilized the same Matrigel and medium showed similar results it was concluded that these problems did not arise from the guidance devices.

The organoids in the guidance devices were healthy until day 30 as determined by qPCR and immunofluorescence but afterwards a deterioration in cell morphology and cell viability was observed. Functional analysis with multi-electrode arrays was performed on day 90 but no activity could be detected. Organoids from the same batch were cultivated in the guidance devices from Osaki et al.[55] but showed even worse results in respect to cell viability and morphology. A later batch of organoids from several different cell lines that was cultured with the same medium and embedded in the same Matrigel yielded similar results. Since the guidance devices from Osaki et al. were previously used successfully by the conductor of the experiments in Lund it was concluded that the failure of the organoid culture was probably caused by some defect of used material like the Matrigel. Due the failure in both control and 3D printed device no meaningful conclusion can be made about the biocompatibility of the printed devices. A reasonable approach might be to just repeat the experiments with new culture material and maybe another batch of stem cells. Some conclusions can however be made about the design of the device. No leakage of medium from the device was reported which indicates that the bottom area in future design should be high. Since the axons did not bundle into fascicles (section 3.2.2.3) it seems that a smaller channel width would be beneficial although the unhealthiness of the organoids makes this conclusion less obvious. Another improvement of the devices would probably be to decrease the well size since the images in Figure 62 seem to indicate an incomplete redirection of the axons towards the channel.

With this final result in the context of this thesis it was successfully shown that the 3D printed structures are a viable candidate for organoid culture in respect to their mechanical and structural aspects. The biocompatibility of the devices could not be shown clearly, bit this might largely be attributed to faults in the materials used for cell culture. The results of the hVM1 spheroids on coated well-plates might be a solid basis for future work with dopaminergic spheroids. The printing process seemed to work reliable in respect to larger structures, but the process was unreliable in respect to the channel width which is a crucial aspect of microfluidic channels. The results may indicate though that the printing process can be optimized or that alternative workflows can be conceptualized that would increase the reproducibility of these features a lot.

4. Conclusion & Outlook

4.1. Cell Cultures

The main goal of this work was to 3D print guidance devices for brain organoids to make a biological model that resembles crucial features of the nigrostriatal pathway. To this aim the organoids are connected in the guidance devices via a microfluidic channel where penetration from dopaminergic axons with subsequent bundling into axon fascicles has to be achieved (see section 3.2.2.3). The author has succeeded in the printed of microfluidic devices with the desired structural features although the printing process has to be viewed critically due to problems with reproducibility in respect to channel width (3.1.5). To investigate the suitability of the devices for 3D cell culture early prints (two-chamber design) were used by the author for the cultivation of hVM1 spheroids. Since leakage of cell medium occurred in these early guidance devices the area was increased for stronger adhesion. The prints with the new design (one-chamber design) were then handed to the project partners at Lund University where they were used for organoid cultures. In addition, different conditions for hVM1 spheroid formation were tested with the author to account for the fact that there are no established protocols. Since the organoid cultures at Lund University afflicted heavily by cell death during the later days of culture with both the printed guidance devices and the reference guidance device no proper conclusion could be made regarding the suitability of the printed devices for organoid culture and axonal guidance. One plausible explanation for this outcome would be that there was a contamination in one of the chemicals since the reference devices had yielded good outcomes in analogue experiments in the past. In order to make a valid judgement of the suitability of the 3D printed devices the organoid culture would need to be repeated either with the same protocol or with different ones until at least the cultures in the reference device are satisfactory in respect to cell viability. A problem that appeared with the newer devices was that the axonal projections of the organoids that penetrated the channel did not bundle into fascicles. This was probably contributed to the fact that a change in channel width was suggested by the project partners since they assumed this might lead to thicker fascicles. The fact that the partners at Lund reported no leakage means that the design change to a larger surface area can be considered a success. A change that was requested by the project partners was the increase of the walls around the wells to help with the seeding of organoids in future experiments. The cultivation of hVM1 spheroids in the two-chamber guidance devices led to viable spheroids with axon protrusion but no decisive conclusion about the suitability of the devices for cell culture can be drawn due to insufficient analysis and the unavailability of reference studies. The results of the cultivation of hVM1 spheroids on coated well-plates might be used to develop working protocols for hVM1 axonal fascicles formation in guidance devices. If it would be possible to find protocol that induce axon protrusion and subsequent formation of axon fascicles on neural spheroids it might be used in the prototyping of bioanalytical devices to reduce time and cost associated with organoid culture. Despite the fact that the investigated conditions for hVM1 spheroid formation and culture led to a drastic improvement in the formation of axon networks the conditions seem not to favor axonal protrusion enough to succeed in this aim. This might however be related to the fact that neither structures for axonal guidance nor any cellular structures that resembles the *in-vivo* target of midbrain dopaminergic neurons were used. The axonal outgrowth was either not projecting outwards enough (PLL) or were too sparse (Geltrex). Immunocytochemistry indicated successful dopaminergic differentiation with both coating. On PLL the spheroids largely retained their spheroidal shape and dense axon networks were formed, but these axon networks did not project straight outwards and instead aligned themselves concentrically to the spheroids where they coiled themselves into bundles. The formed bundles were too short for the envisioned purpose but a possible rout to success might be here to add Geltrex in the medium after the initial days of spheroid culture on PLL. A possible explanation to this would be that PLL does not provide physiological ECM proteins for integrin interaction which might have caused axonal outgrowth to be redirected towards neighboring axons and cell soma. Although PLL has been shown to be effective in guiding axonal growth[69, 70] these findings stem from 2D cultures on patterned surfaces and are therefore not expected to necessarily yield the same outcomes. The spheroids that were transferred onto Geltrex flattened readily and formed much longer axons than the spheroids on PLL. The number of protruding axons was far reduced compared to PLL which rendered them unviable as a substitute for connectoids. A possible approach for further experiments might be to transfer spheroids on PLL coated well plates and then add Geltrex or ECM proteins to improve axonal growth and prevent redirection towards concentric trajectories since this would be incompatible with the necessary channel penetration on the guidance devices. It could be tested whether the presence of forebrain derived spheroid would be sufficient to redirect hVM1 spheroid axons towards themselves even without provision of physiological ECM proteins. Differentiation medium seeding yielded superior results to proliferation medium seeding under all conditions. This suggests that cells should be suspended directly in differentiation medium when seeded for spheroid formation. In addition to the inferior outcomes regarding axonal outgrowth lower cell viability was observed with proliferation medium seeding, especially with smaller spheroids. One factor for this low cell viability might be greater metabolic stress due to retention of proliferation medium that leads to increased necrosis starting from the interior of the spheroids. From the three different spheroid sizes tested the medium and large spheroids formed from 50.000 & 75.000 cells respectively performed relative comparable. The performance of the smaller spheroids of 25.000 cells was mostly inferior but yielded some exceptionally good results on Geltrex due to the greater variability with smaller spheroids. The effect of transfer time from ultra-low attachment plates to coated well plates is not very clear due to a large in-group variability in comparison to a relatively low between-group variability and a low number of samples per condition. If the influence of the cell number during spheroid formation should be investigated further, it would be necessary to conduct experiments with much larger sample numbers per condition to account for these variabilities. Live/dead imaging indicated good cell viability for the outgrowths and the outer layers of non-flattened spheroids and a necrotic core in the interior. For flattened spheroids live/dead imaging indicated clusters of dead cells facing upwards with living cells facing downwards which presumably showed spheroidal fragments that had spatially rearranged themselves during flattening. These clusters were of varying sizes and were interspersed by monolayered cells with high viability. As evident from the comparison between brightfield microscopy and the images from live/dead, - & immunostaining the neuronal processes were not only abrased during fixation but also during PBS washing. The likelihood of full abrasion depended on the conditions of the respective sample and may be the result of conditions detrimental to cell viability, but also just due to mechanical mishandling. Abrasion during washing happened for most spheroids that did not show clear signs of cell viability like spheroid flattening or cellular outgrowth but it also happened with many spheroids that appeared to have a healthy morphology on the brightfield images. Due to different mechanisms of adhesion PLL and Geltrex must be regarded separately when discussing the loss of axons. The adhesion of neurons and axons on Geltrex-coated plates can be assumed to be largely dependent on integrin interactions with Geltrex proteins[72, 84-86].

Since PBS contained the calcium chelator EDTA, which is known to interfere with integrin function[87], this might be considered to be the main cause for axonal loss on Geltrex. The adhesion of neurons on PLL is presumably based on a temperature-dependent mechanism involving its cationic amino groups[88]. Since the samples have been imaged before fixation cooling during this process might explain the damage done to the samples on PLL. Concluding the results of cell culture experiments has not given a valid evaluation of the suitability of the guidance devices for organoid culture, due to large cell death in both sample and control. The results from the spheroid cultures indicate too that the cell death was not caused by the printed device. The final prototypes might be unsuitable for axon guidance due to a too large channel, but simple design changes would correct this. Future studies might use the same experiments to investigate the suitability of the guidance devices and may then give a final answer about the biocompatibility of the printed devices.

4.2. Printing Process

The aim was to design a fast and reliable workflow for volumetric 3D printing of detachable biomedical devices. One feature of this printing process should be the reliable and reproducible fabrication of microfluidic channels like the ones used for the guidance devices. A workflow was established that could be used for the reliable fabrication of detachable structures (see section 2.2.2) although there were problems with leakage with some devices as discussed in the previous section. It was not possible with this workflow to print microfluidic channels with a decent reproducibility in regard to their width, due to major variations of extrusion width in the bottom layers. This is assumed to be largely the result of problems with bed levelling. The low variability of channel width of the slices with uniform channel width or the results with the z-correction factor of 350 μm indicates that a high reproducibility might be possible, but further improvements in z-alignment and levelling are needed. Testing of z-correction factors between 200 and 350 μm could yield better performances in respect to variability and stability. Variation of more printing parameters could lead to additional improvements. One potential vector for increased reproducibility might be the use of new PDMS ink formulations might prevent leakage with high first layer height. This might then be used to stabilize printing with high z-correction factors and thus decrease variability. An example would the mixing of SE1700 PDMS printing ink with Sylgard 184 casting PDMS[89]. The mixing of viscous PDMS ink with casting PDMS might lead to an ink that largely formstable but has a certain fluidity at rest that might prevent the formation of lumen during curing or internal leakage as the result of high first layer height. The upside-down printing method yielded good results, but this method would need further refinement to determine its potential. The apparent partially delamination might be countered by an increased extrusion multiplier or by reduced distances in the printing path, but this may lead to problems with over extrusion especially in the first printing layers. This problem might also be better solvable with new ink formulations. In particular, the effects of passivated primary substrates or water-soluble primary substrates and the effects of pre-curing before attachment to the secondary substrate would need to be investigated. In summary it can be said that the used methods for volumetric PDMS printing are usable for the fabrication of complex 3D structures, which are otherwise printed using either commercially available but expensive bioprinting systems or pneumatic home-made printing systems. However, the problems associated with the variability remain a major set-back to the described method. Due to the higher costs of state-of-the-art printing systems, they are not accessible for most research groups and the FelixBIO may thus be a viable commercial alternative for PDMS printing. Further, the fabrication of open-source volumetrically controlled syringe-extrusion 3D printer for PDMS printing based on RepRap technology may be an even cheaper option compared to the FelixBIO and may be more user-friendly than open-source pneumatic printers. Before this method might find wider application the problems with the reproducibility would have to be tackled. One problem appeared to be the manual fixation of the samples with a double adhesive tape as concluded by experience. An efficient way to increase the reproducibility might be gained through the fabrication of a substrate holder as depicted in Figure 63.

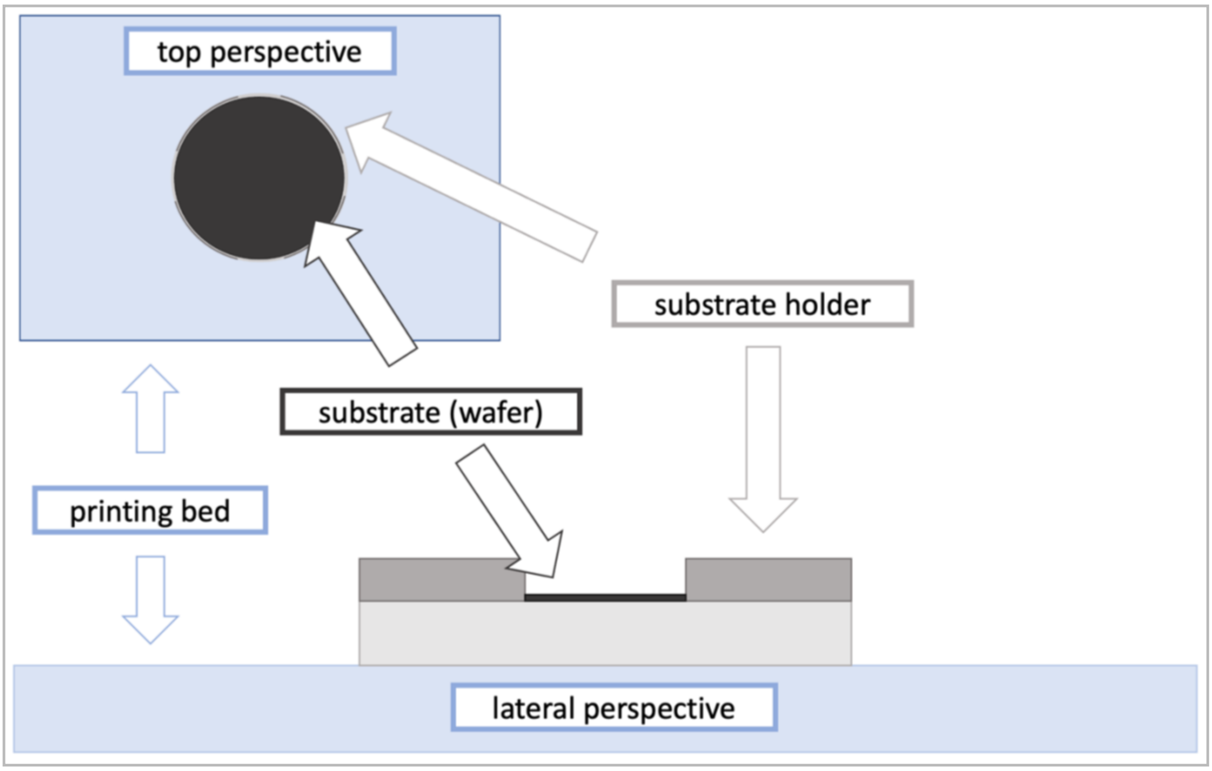

Figure 63 Proposal of a substrate holder to improve alignment for increased reproducibility. The depicted substrate holder could be used to circumvent the problematic fixation of the substrate on the printing bed with double adhesive tape and the windows in the holder would enable optical z-probing along the x and y axes on the edges of the substrate for bed leveling.

This could yield increased reproducibility due to circumvention of the problematic fixation of the substrate on the printing bed with tape which is assumed to be one of the main factors for variability. Furthermore, this would allow for readily optical z-alignment at many points for better bed leveling (see section 3.1.3). This would be a great improvement due to the insufficiencies with the automatic bed leveling. Optical methods for optical z-alignment appeared sufficient for z-alignment on the wafer, but they could not be used for bed leveljng due to the need for accessible edges. An alternative concept for fabrication might be to print the critical sub-structures *en-masse* and select the best specimen for assembly. This way the need for operation skill for the fabrication might be reduced. In the case of axonal guidance devices thin channel structures might be mass-produced and then assembled within outer walls using casting PDMS as depicted in Figure 64/A.

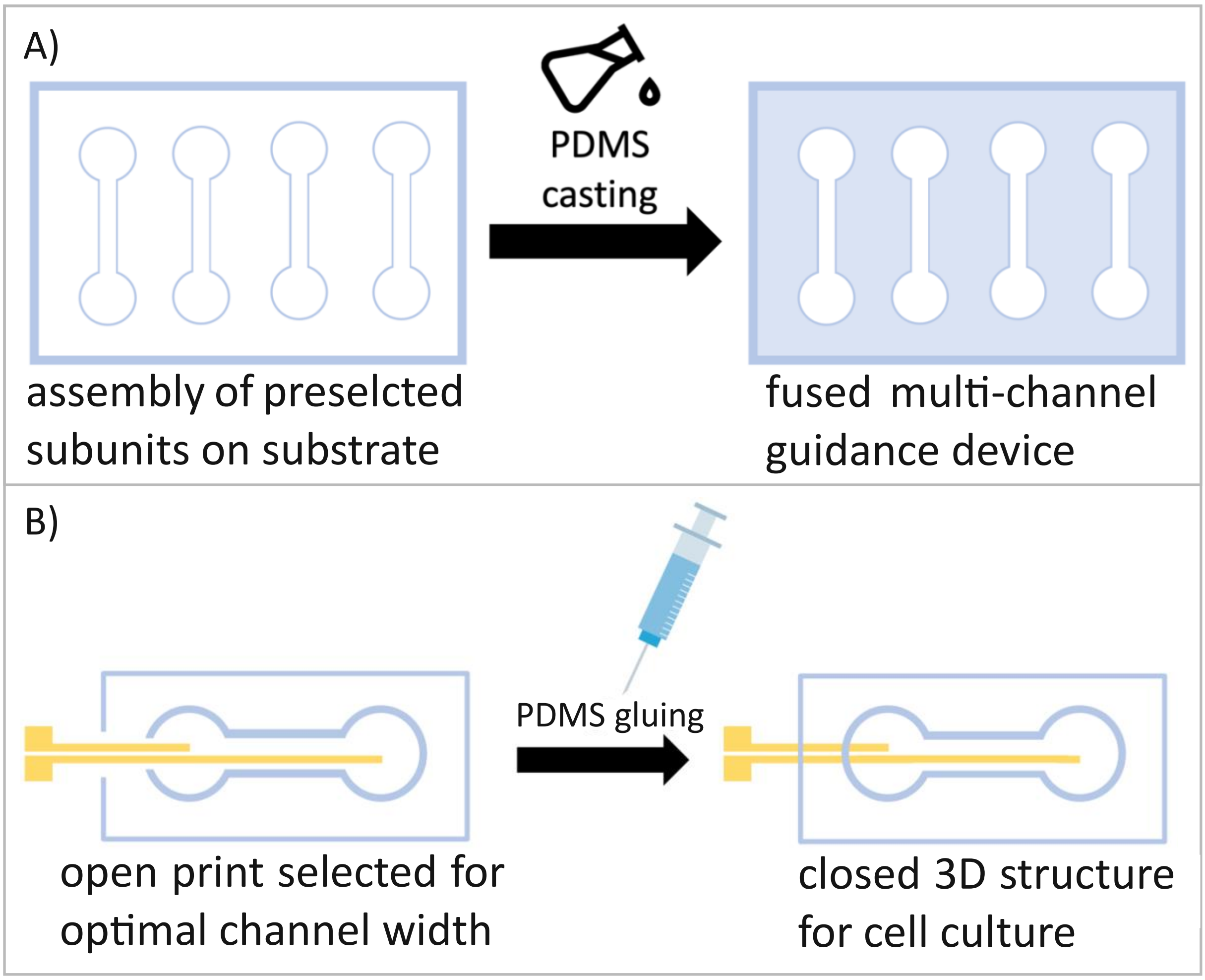

Figure 64 Proposed workflow for the fabrication of microfluidic structures using DIW 3D printing (A&B) and for the integration of microelectronic structures therein (B). In order to fabricate guidance devices or similar microfluidic structures with the need of larger medium reservoir the critical sub-structures, in this case the microfluidic channel should be fabricated as isolated units and then assembled within outer walls before being fused with casting PDMS. This workflow would allow a higher reproducibility since subunits could be printed en-masse and selected for optimal proportions or fabricated using a stereolithographic approach. For the fabrication of microelectronic devices, such as gold electrode depicted in B, an analogue approach could be used where PDMS structures with the critical sub-structures are fabricated with an open end that could be closed by PDMS gluing to integrate the electronic structures therein. For the flask and the syringe vector graphics were used from [90] and [91] respectively.

This approach might also drastically reduce the time needed for the fabrication of microfluidic systems due to the downscaling of the printed units for screening. Alternatively, the sub-structures could be produced with high fidelity using stereolithography before integration within 3D printed walls. A possible vector for the integration of electrodes or other functional units might be the fabrication of open structures that can be closed by manual PDMS gluing as shown in Figure 64/B. This integration of electrode might also be readily achieved by the upside-down printing method.

4.3 Outlook

In general, this work has shown that volumetric 3D-printing of PDMS guidance devices is feasible, but the problems with the reproducibility must be overcome in order to make the method feasible for most researchers. These problems can be largely attributed to problems with bed leveling. Different approaches therefor have been suggested in the previous section. This work has further used methods for the evaluation of prints such as the imaging of slices to investigate the interior of the samples and has suggested several solutions to problems in 3D printing, especially in regard to volumetric DIW in particular or z-alignment in general. The cultivation of organoids in the printed PDMS structures was not successful, but this is assumed to have been the results of quality issues of the used materials for cell culture. Protocols for the formation and culture of hVM1 has been formulated and evaluation in regard to their potential. In addition, problems with the fixation of axons were revealed which might lead to better protocols for immunostaining in the future.

5. Appendix

5.1 Table of Figures

5.2 Table of Tables

5.3 Citations

1. Dauer, W. and S. Przedborski, *Parkinson's disease: mechanisms and models.* Neuron, 2003. **39**(6): p. 889-909.
2. McGregor, M.M. and A.B. Nelson, *Circuit Mechanisms of Parkinson's Disease.* Neuron, 2019. **101**(6): p. 1042-1056.
3. Bastide, M.F., et al., *Pathophysiology of L-dopa-induced motor and non-motor complications in Parkinson's disease.* Progress in Neurobiology, 2015. **132**: p. 96-168.

4. Zarzycki, M.Z. and I. Domitrz, *Stimulation-induced side effects after deep brain stimulation – a systematic review.* Acta Neuropsychiatrica, 2020. **32**(2): p. 57-64.
5. Kalia, L.V. and A.E. Lang, *Parkinson's disease.* The Lancet, 2015. **386**(9996): p. 896-912.
6. Walker, Z., et al., *Lewy body dementias.* The Lancet, 2015. **386**(10004): p. 1683-1697.
7. Cummings, J.L., T. Morstorf, and K. Zhong, *Alzheimer's disease drug-development pipeline: few candidates, frequent failures.* Alzheimers Res Ther, 2014. **6**(4): p. 37.
8. Białkowska, K., et al., *Spheroids as a Type of Three-Dimensional Cell Cultures-Examples of Methods of Preparation and the Most Important Application.* Int J Mol Sci, 2020. **21**(17).
9. Fennema, E., et al., *Spheroid culture as a tool for creating 3D complex tissues.* Trends in Biotechnology, 2013. **31**(2): p. 108-115.
10. Dingle, Y.T., et al., *Three-Dimensional Neural Spheroid Culture: An In Vitro Model for Cortical Studies.* Tissue Eng Part C Methods, 2015. **21**(12): p. 1274-83.
11. Reynolds, B.A. and S. Weiss, *Generation of Neurons and Astrocytes from Isolated Cells of the Adult Mammalian Central Nervous System.* Science, 1992. **255**(5052): p. 1707-1710.
12. Reynolds, B.A. and R.L. Rietze, *Neural stem cells and neurospheres—re-evaluating the relationship.* Nature Methods, 2005. **2**(5): p. 333-336.
13. Singec, I., et al., *Defining the actual sensitivity and specificity of the neurosphere assay in stem cell biology.* Nature Methods, 2006. **3**(10): p. 801-806.
14. Zhuang, P., et al., *3D neural tissue models: From spheroids to bioprinting.* Biomaterials, 2018. **154**: p. 113-133.
15. Lancaster, M.A. and J.A. Knoblich, *Organogenesis in a dish: modeling development and disease using organoid technologies.* Science, 2014. **345**(6194): p. 1247125.
16. Sasai, Y., *Cytosystems dynamics in self-organization of tissue architecture.* Nature, 2013. **493**(7432): p. 318-26.
17. Pașca, S.P., *The rise of three-dimensional human brain cultures.* Nature, 2018. **553**(7689): p. 437-445.
18. Sasai, Y., *Next-Generation Regenerative Medicine: Organogenesis from Stem Cells in 3D Culture.* Cell Stem Cell, 2013. **12**(5): p. 520-530.
19. Zhang, W., et al., *Microglia-containing human brain organoids for the study of brain development and pathology.* Mol Psychiatry, 2023. **28**(1): p. 96-107.
20. Arlotta, P., *Organoids required! A new path to understanding human brain development and disease.* Nat Methods, 2018. **15**(1): p. 27-29.
21. Curtis, A., *Cell adhesion.* Progress in biophysics and molecular biology, 1973. **27**: p. 315-384.
22. Guttman, M., S. Kish, and Y. Furukawa, *Current concepts in the diagnosis and management of Parkinson's disease.* CMAJ : Canadian Medical Association journal = journal de l'Association medicale canadienne, 2003. **168**: p. 293-301.
23. Turing, A.M., *The chemical basis of morphogenesis.* Philosophical Transactions of the Royal Society of London. Series B, Biological Sciences, 1952. **237**(641): p. 37-72.
24. Chiaradia, I. and M.A. Lancaster, *Brain organoids for the study of human neurobiology at the interface of in vitro and in vivo.* Nat Neurosci, 2020. **23**(12): p. 1496-1508.
25. Wurst, W. and L. Bally-Cuif, *Neural plate patterning: Upstream and downstream of the isthmic organizer.* Nature Reviews Neuroscience, 2001. **2**(2): p. 99-108.

26. Heylighen, F., *Stigmergy as a universal coordination mechanism I: Definition and components.* Cognitive Systems Research, 2016. **38**: p. 4-13.
27. Isaeva, V., *Self-Organization in Biological Systems.* Izvestiia Akademii nauk. Seriia biologicheskaia / Rossiĭskaia akademiia nauk, 2012. **39**: p. 144-53.
28. Mehra, A. and J.L. Wrana, *TGF-beta and the Smad signal transduction pathway.* Biochem Cell Biol, 2002. **80**(5): p. 605-22.
29. Chambers, S.M., et al., *Highly efficient neural conversion of human ES and iPS cells by dual inhibition of SMAD signaling.* Nature Biotechnology, 2009. **27**(3): p. 275-280.
30. Schier, A.F., *Nodal Signaling in Vertebrate Development.* Annual Review of Cell and Developmental Biology, 2003. **19**(1): p. 589-621.
31. Rodríguez-Esteban, C.n., et al., *Wnt signaling and PKA control Nodal expression and left-right determination in the chick embryo.* Development, 2001. **128**(16): p. 3189-3195.
32. Kadoshima, T., et al., *Self-organization of axial polarity, inside-out layer pattern, and species-specific progenitor dynamics in human ES cell–derived neocortex.* Proceedings of the National Academy of Sciences, 2013. **110**(50): p. 20284-20289.
33. Qian, X., et al., *Generation of human brain region–specific organoids using a miniaturized spinning bioreactor.* Nature Protocols, 2018. **13**(3): p. 565-580.
34. Mulligan, K.A. and B.N. Cheyette, *Wnt signaling in vertebrate neural development and function.* J Neuroimmune Pharmacol, 2012. **7**(4): p. 774-87.
35. Nakamura, H., et al., *Isthmus organizer for midbrain and hindbrain development.* Brain Res Brain Res Rev, 2005. **49**(2): p. 120-6.
36. Blaess, S., et al., *Temporal-spatial changes in Sonic Hedgehog expression and signaling reveal different potentials of ventral mesencephalic progenitors to populate distinct ventral midbrain nuclei.* Neural Development, 2011. **6**(1): p. 29.
37. Shou, Y., et al., *The Application of Brain Organoids: From Neuronal Development to Neurological Diseases.* Frontiers in Cell and Developmental Biology, 2020. **8**.
38. Jalink, P. and M. Caiazzo, *Brain Organoids: Filling the Need for a Human Model of Neurological Disorder.* Biology, 2021. **10**(8): p. 740.
39. Itskovitz-Eldor, J., et al., *Differentiation of Human Embryonic Stem Cells into Embryoid Bodies Comprising the Three Embryonic Germ Layers.* Molecular Medicine, 2000. **6**(2): p. 88-95.
40. Lancaster, M.A., et al., *Cerebral organoids model human brain development and microcephaly.* Nature, 2013. **501**(7467): p. 373-9.
41. Ying, Q.-L., et al., *Conversion of embryonic stem cells into neuroectodermal precursors in adherent monoculture.* Nature Biotechnology, 2003. **21**(2): p. 183-186.
42. Kelava, I. and Madeline A. Lancaster, *Stem Cell Models of Human Brain Development.* Cell Stem Cell, 2016. **18**(6): p. 736-748.
43. Qian, X., et al., *Brain-Region-Specific Organoids Using Mini-bioreactors for Modeling ZIKV Exposure.* Cell, 2016. **165**(5): p. 1238-1254.
44. Miura, Y., et al., *Generation of human striatal organoids and cortico-striatal assembloids from human pluripotent stem cells.* Nature Biotechnology, 2020. **38**(12): p. 1421-1430.
45. Smits, L.M. and J.C. Schwamborn, *Midbrain Organoids: A New Tool to Investigate Parkinson's Disease.* Frontiers in Cell and Developmental Biology, 2020. **8**.
46. Chinta, S.J. and J.K. Andersen, *Dopaminergic neurons.* The International Journal of Biochemistry & Cell Biology, 2005. **37**(5): p. 942-946.

47. OpenMIND. *OpenMIND homepage; https://openmind.dtu.dk/*. 2022.
48. Vasudevan, S., et al., *Leaky Optoelectrical Fiber for Optogenetic Stimulation and Electrochemical Detection of Dopamine Exocytosis from Human Dopaminergic Neurons.* Advanced Science, 2019. **6**(24): p. 1902011.
49. Lewis, J.A., *Direct Ink Writing of 3D Functional Materials.* Advanced Functional Materials, 2006. **16**(17): p. 2193-2204.
50. University, M.K.T.O., *Design and Manufacture with Polymers: Solid properties and design*. 2000.
51. *Washington State University Homepage, Fundamentals of Direct-Ink-Writing, https://labs.wsu.edu/mpml/projects/*.
52. Bordás, R., *Vorlesungsskript Rheologie.*
53. Miranda, I., et al., *Properties and Applications of PDMS for Biomedical Engineering: A Review.* Journal of Functional Biomaterials, 2022. **13**(1): p. 2.
54. Kajtez, J., et al., *3D-Printed Soft Lithography for Complex Compartmentalized Microfluidic Neural Devices.* Advanced Science, 2020. **7**(16): p. 2001150.
55. Osaki, T., et al., *Three-Dimensional Motor Nerve Organoid Generation.* J Vis Exp, 2020(163).
56. *RepRap Project; https://reprap.org/wiki/RepRap*.
57. Tang, Z., et al., *Coaxial Printing of Silicone Elastomer Composite Fibers for Stretchable and Wearable Piezoresistive Sensors.* Polymers, 2019. **11**(4): p. 666.
58. Yan, H.-l., et al., *Coaxial printing method for directly writing stretchable cable as strain sensor.* Applied Physics Letters, 2016. **109**(8).
59. Sher, D., *3D Bioprinting For Just $1000, https://all3dp.com/3d-bioprinting-for-just-1000/*.
60. *FelixRobotics Website, https://www.felixprinters.com/felix-bioprinter/*.
61. Hadiono, C., *Aniwaa, https://www.aniwaa.com/product/3d-printers/regenhu-3ddiscovery/*.
62. *Padana Cleanroom Website, https://www.padanacleanroom.it/en/discover-the-new-era-of-cleanrooms-english/*.
63. *DOW Homepage, DOWSIL SE1700 product discription, https://www.dow.com/en-us/pdp.dowsil-se-1700.01707116z.html#overview*.
64. *Cymit Quimica, 1H,1H,2H,2H-perfluorodecyltrichlorosilane, https://cymitquimica.com/cas/78560-44-8*.
65. Sozzi, E., et al., *Generation of Human Ventral Midbrain Organoids Derived from Pluripotent Stem Cells.* Current Protocols, 2022. **2**(9): p. e555.
66. Villa, A., et al., *Generation and properties of a new human ventral mesencephalic neural stem cell line.* Exp Cell Res, 2009. **315**(11): p. 1860-74.
67. Martínez-Cerdeño, V. and S.C. Noctor, *Neural Progenitor Cell Terminology.* Frontiers in Neuroanatomy, 2018. **12**.
68. Tønnesen, J., et al., *Functional properties of the human ventral mesencephalic neural stem cell line hVM1.* Experimental Neurology, 2010. **223**(2): p. 653-656.
69. Joo, S., K. Kang, and Y. Nam, *In vitro neurite guidance effects induced by polylysine pinstripe micropatterns with polylysine background.* Journal of Biomedical Materials Research Part A, 2015. **103**(8): p. 2731-2739.
70. Fricke, R., et al., *Axon guidance of rat cortical neurons by microcontact printed gradients.* Biomaterials, 2011. **32**(8): p. 2070-6.

71. Gonzalez-Perez, F., E. Udina, and X. Navarro, *Chapter Ten - Extracellular Matrix Components in Peripheral Nerve Regeneration*, in *International Review of Neurobiology*, S. Geuna, et al., Editors. 2013, Academic Press. p. 257-275.
72. Robles, E. and T.M. Gomez, *Focal adhesion kinase signaling at sites of integrin-mediated adhesion controls axon pathfinding.* Nat Neurosci, 2006. **9**(10): p. 1274-83.
73. Zhang, D., et al., *Niche-derived laminin-511 promotes midbrain dopaminergic neuron survival and differentiation through YAP.* Sci Signal, 2017. **10**(493).
74. *3D midbrain model using neural organoids.* ThermoFisher BIOPROBES 81, SUMMER 2020.
75. Datasheet of the DAC 150.1 FVZ Speedmixer, H., https://cdn2.site-media.eu/images/document/3477924/DAC150.1_EN.pdf, .
76. *FelixBIO Specifications,* *https://www.felixbio.com/felix-bioprinter-landing*.
77. Gürbüz, H., *3D printing of functional scaffolds for neural interfaces*. 2021.
78. *Autodesk Homepage, Fusion360,* *https://www.autodesk.com/products/fusion-360/overview?term=1-YEAR&tab=subscription*.
79. *Wikipedia - Shear thinning,* *https://en.wikipedia.org/wiki/Shear_thinning*.
80. *Biesterfeld Electronics Portfolio,* *https://www.biesterfeld.com/fileadmin/documents/product/BSC_Portfolio_Electronics_2021_A4_UK_Web.pdf*.
81. Dent, E.W., S.L. Gupton, and F.B. Gertler, *The growth cone cytoskeleton in axon outgrowth and guidance.* Cold Spring Harbor perspectives in biology, 2011. **3**(3): p. a001800.
82. Kawada, J., et al., *Generation of a Motor Nerve Organoid with Human Stem Cell-Derived Neurons.* Stem Cell Reports, 2017. **9**(5): p. 1441-1449.
83. P B Molinoff, a. and J. Axelrod, *Biochemistry of Catecholamines.* Annual Review of Biochemistry, 1971. **40**(1): p. 465-500.
84. McKerracher, L., M. Chamoux, and C.O. Arregui, *Role of laminin and integrin interactions in growth cone guidance.* Molecular Neurobiology, 1996. **12**(2): p. 95-116.
85. Flynn, K.C., *The cytoskeleton and neurite initiation.* BioArchitecture, 2013. **3**(4): p. 86-109.
86. Bandtlow, C.E. and D.R. Zimmermann, *Proteoglycans in the developing brain: new conceptual insights for old proteins.* Physiol Rev, 2000. **80**(4): p. 1267-90.
87. Lai, T.-Y., et al., *Different methods of detaching adherent cells and their effects on the cell surface expression of Fas receptor and Fas ligand.* Scientific Reports, 2022. **12**(1): p. 5713.
88. Yavin, E. and Z. Yavin, *Attachment and culture of dissociated cells from rat embryo cerebral hemispheres on polylysine-coated surface.* J Cell Biol, 1974. **62**(2): p. 540-6.
89. Ozbolat, V., et al., *3D Printing of PDMS Improves Its Mechanical and Cell Adhesion Properties.* ACS Biomaterials Science & Engineering, 2018. **4**(2): p. 682-693.
90. *pngwing,* *https://www.pngwing.com/en/search?q=flask+Vector*.
91. *vecteezy,* *https://www.vecteezy.com/vector-art/1877994-injection-syringe-flat-style-icon*

.